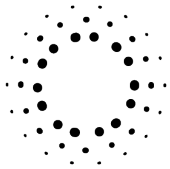

IFT - UNESP
INSTITUTO DE FÍSICA TEÓRICA

TESE DE DOUTORAMENTO IFT–T.004/23

Exploring Composite Higgs Models at Present and Future Colliders:

A study on the Top-Higgs Sector and the Importance of Three-Body Decays in Vector-like Quark Searches

Carlos Yosep Bautista Choqque

Orientador

Ricardo D'Elia Matheus

Maio de 2023

Bautista Choqque, Carlos Yosep.
B352e Exploring composite Higgs models at present and future colliders: a study on the top-Higgs sector and the importance of three-body decays in vector-like quark searches / Carlos Yosep Bautista Choqque. – São Paulo, 2023
154 f.: il. color.

Tese (doutorado) – Universidade Estadual Paulista (Unesp), Instituto de Física Teórica (IFT), São Paulo
Orientador: Ricardo D'Elia Matheus

1. Partículas (Física nuclear). 2. Higgs, bosons de. 3. Colisores hadrônicos. I. Título

Sistema de geração automática de fichas catalográficas da Unesp. Biblioteca do Instituto de Física Teórica (IFT), São Paulo. Dados fornecidos pelo autor(a).

EXPLORING COMPOSITE HIGGS MODELS AT PRESENT AND FUTURE COLLIDERS: A STUDY ON THE TOP-HIGGS SECTOR AND THE IMPORTANCE OF THREE-BODY DECAYS IN VECTOR-LIKE QUARK SEARCHES

Tese de Doutorado apresentada ao Instituto de Física Teórica do Câmpus de São Paulo, da Universidade Estadual Paulista "Júlio de Mesquita Filho", como parte dos requisitos para obtenção do título de Doutor em Física, Especialidade Física Teórica.

Comissão Examinadora:

Prof. Dr. RICARDO D'ELIA MATHEUS(Orientador)
Instituto de Física Teórica/UNESP

Prof. Dr. ROGÉRIO ROSENFELD
Instituto de Física Teórica/UNESP

Prof. Dr. THIAGO RAFAEL FERNANDEZ PEREZ TOMEI
Instituto de Física Teórica/UNESP

Prof. Dr. OSCAR JOSÉ PINTO ÉBOLI
IFUSP/Instituto de Física da USP

Prof. Dr. CHEE SHENG FONG
UFABC/Universidade Federal do ABC

Conceito: Aprovado

São Paulo, 26 de junho de 2023.

Dedico esta tese a minha familia

Agradecimentos

Gostaria de expressar meus sinceros agradecimentos a todos que contribuíram para a realização desta tese.

Em primeiro lugar, gostaria de agradecer ao meu orientador, Ricardo, pela sua orientação, paciência e dedicação ao longo de todo o processo. Suas orientações e perspectivas enriquecedoras foram fundamentais para o desenvolvimento deste trabalho.

Também gostaria de agradecer à Aurore e ao Leonardo pelas constantes discussões que acrescentaram significativamente ao valor deste trabalho. Da mesma forma, a Leônidas, Geum Bong, Nicola e Maxwell, que forneceram valiosas contribuições em diferentes etapas desta jornada.

Gostaria de dedicar um agradecimento especial a Eduardo, cuja memória e influência continuam vivas em minha vida e jornada acadêmica. Embora não esteja mais fisicamente presente, sua paixão pelo conhecimento, rigor acadêmico e espírito corajoso sempre servirão como exemplo a ser seguido.

Expresso minha gratidão aos meus pais por me darem a vida e apoiarem minhas decisões. À minha mãe Sebastiana, por todo seu sacrifício e amor, e ao meu pai Augusto, por ter plantado a semente da curiosidade em mim desde que eu era criança. Também sou grato à minha irmã Mercedes por me motivar a buscar a excelência e me esforçar para ser um exemplo para ela.

Quero estender meus agradecimentos aos colegas e amigos Segundo, Gabriel, Max, Enzo, Carol, Vivian, Victor, por fazerem parte da minha vida e tornarem essa jornada acadêmica mais leve e memorável. Agradeço também à Cibele por sua companhia, compreensão e apoio.

Por fim, gostaria de agradecer ao IFT-UNESP por fornecer as instalações adequadas para a realização da pesquisa e à CAPES pelo apoio financeiro.

Resumo

A tese concentra-se no estudo de duas realizações do Modelo Higgs Composto Mínimo, o MCHM_5 e o MCHM_{14}, em colisores hadrônicos de alta energia. Exploramos dois regimes de energia: o do LHC e sua atualização de Alta Luminosidade (HL-LHC), e futuros colisores hadrônicos com 100 TeV de energia de centro de masa. Desenvolvemos estruturas completas de geração e simulação para explorar o espaço de parâmetros desses modelos e conduzimos uma investigação sistemática usando um algoritmo de agrupamento. Os processos de produção $t\bar{t}h$ e $t\bar{t}hh$ foram examinados, revelando que desvios na seção de choque podem ocorrer e que a contribuição não ressonante no processo $t\bar{t}hh$ é considerável, fornecendo acesso ao acoplamento duplo de Yukawa introduzido por esses modelos. Pontos representativos foram selecionados para resumir a fenomenologia do espaço de parâmetros para cada regime de energia. Parceiros do top com consideráveis decaimentos em três corpos foram encontrados para algumas regiões do espaço de parâmetros. A inclusão desse canal em buscas experimentais foi explorada, aumentando os limites de exclusão anteriores. Finalmente, uma busca inclusiva foi proposta, e os resultados mostraram uma significância promissora no HL-LHC com uma luminosidade de 4 ab^{-1}.

Palavras Chaves: Além do modelo Padrão; Higgs composto; Decaimento em três corpos; Quarks Vector-like; Colisores de altas energias.

Áreas do conhecimento: Física; Física de partículas.

Abstract

The thesis focuses on studying two realizations of the Minimal Composite Higgs Model: the $MCHM_5$ and the $MCHM_{14}$, at high energy hadron colliders. We explored two energy regimes: that of the LHC and its High luminosity upgrade (HL-LHC), and future hadron colliders at a center of mass energy of 100 TeV. We developed full generation and simulation frameworks to explore the parameter space of these models and conducted a systematic investigation using a clustering algorithm. The $t\bar{t}h$ and $t\bar{t}hh$ production processes were examined, revealing that deviations in cross section can occur and the non-resonant contribution in the tthh process is sizable, providing access to the double Yukawa coupling introduced by these models. Representative points were selected to summarize the phenomenology of the parameter space for each energy regime. Top partners with sizable three-body decays were found for some regions of the parameter space. The inclusion of this channel in experimental searches was explored, increasing previous exclusion limits. Finally, an inclusive search was proposed, and the results showed promising significance at the HL-LHC with a luminosity of 4 ab^{-1}.

Keywords: Beyond the Standard Model; Composite Higgs; Three-body decay; Vector-like quarks; High-energy colliders.

Fields of knowledge: Physics; Particle physics.

Contents

List of Tables

List of Figures

Chapter 1

Introduction

The Standard Model (SM) of particle physics is a well-established theoretical framework that describes the interactions between the fundamental particles that make up the visible universe. This model has been extensively tested over the past several decades and has been found to agree with a wide range of experimental observations and measurements, including the discovery of the Higgs boson at the Large Hadron Collider (LHC) in 2012 [1, 2].

Despite its success, the SM leaves several key questions unanswered, such as the nature of dark matter and the lack of an explanation for the observed matter-antimatter asymmetry in the universe, among others[3]. One of these challenges is the naturalness problem, which is the question of why the Higgs boson mass is so much lighter than the Planck scale or some other UV scale. The SM predicts that the Higgs boson mass receives quantum corrections from virtual particles, and these corrections are proportional to the energy scale at which the particles are produced. Since the Planck scale is so much larger than the weak scale, these quantum corrections are expected to make the Higgs boson mass much larger than it actually is, unless there is an extremely delicate balance between the parameters in the SM, which is not explained by any underlying symmetry.

The naturalness problem has motivated the search for new physics at the TeV scale, which could explain the smallness of the Higgs boson mass. One proposed solution is supersymmetry [4, 5, 6, 7], which postulates a new symmetry between bosons and fermions and introduces a new set of particles with the same quantum numbers as the SM particles but with different spins. Supersymmetry predicts that the quantum corrections to the Higgs boson mass are cancelled by the contributions from the new particles, leading to a natural explanation for the smallness of the Higgs boson mass. Another proposed solution is provided by extra-dimensional models [8, 9], which postulate spatial dimensions beyond the three we observe. In the Randall–Sundrum scenario, Standard-Model (SM) fields—including the Higgs

boson—are confined to a four-dimensional 'TeV brane' located at one end of a warped extra dimension, whereas gravity is localized on the opposite 'Planck brane.' The exponential warping generates the observed weak–Planck hierarchy.

Composite Higgs Models (CHM) [10, 11, 12, 13] are another promising solution to the naturalness problem. They propose that the Higgs boson is not a fundamental particle, but is instead composed of more basic building blocks, similar to how composite particles, such as protons and neutrons, are made up of more fundamental quarks and gluons. These models introduce new interactions and dynamics that help to stabilize the Higgs boson mass and provide a more natural explanation for the observed mass hierarchy.

In CHM, the Higgs boson arises as a bound state of a new strongly-interacting sector, which is characterized by a scale of confinement, Λ. The Higgs boson is a composite scalar that transforms non-linearly under the global symmetries of the theory, which leads to a protection of its mass from large quantum corrections. These models predict the existence of additional scalar and vector bosons, as well as fermions, which are partner states of the Standard Model particles. These new states could be discovered at current or future high-energy colliders, providing a distinctive signature of composite Higgs models.

Particle accelerators have been devised and built in order to address the open questions and further test the predictions of the SM. The LHC, located at CERN, is currently the world's largest and most powerful particle accelerator, and it has provided a wealth of new data on the properties and interactions of the fundamental particles. By colliding beams of high-energy particles, the LHC and other particle accelerators allow physicists to probe the structure of matter and energy at scales far beyond the reach of direct observation. In the coming years, new accelerators and experimental facilities are expected to be built, which will provide an even more precise and comprehensive understanding of the nature of the universe, and they will play a crucial role in advancing our knowledge of the Standard Model and beyond.

The High-Luminosity Large Hadron Collider (HL-LHC) is a major upgrade to the existing LHC [14]. It will increase the number of proton-proton collisions that can be produced by a factor of 10, compared to the current LHC. This increase in luminosity will allow physicists to study rare and exotic processes that are difficult to

observe with the current accelerator. The HL-LHC will achieve its higher luminosity by several improvements, including the installation of new superconducting magnets, more powerful radiofrequency cavities, and new collimators to improve the beam quality. The HL-LHC is expected to begin operation in the mid-2020s and continue through the 2030s, providing a wealth of new data to study.

In addition to the HL-LHC upgrade, CERN is also exploring a new accelerator, the Future Circular Collider (FCC) [15, 16]. The proposed FCC would consist of a 100-kilometer circular tunnel located at CERN, and it would be capable of colliding protons at energies of up to 100 TeV. The first hadronic collisions are expected to occur by 2065–70. Apart from the developments at CERN, China is also investing in particle accelerators, with plans for a new facility called the Super Proton-Proton Collider (SppC) [17, 18, 19, 20, 21]. The SppC has a construction timeline of 2042-2050, it will have a circumference of 100 km and aims to reach a center of mass energy of 125-150 TeV. These proposed accelerators would allow to study the properties of particles at even higher energies than are possible with the LHC, and they would also be capable of studying the Higgs boson and other particles in much greater detail [22, 23, 24].

The Top-Higgs sector, in particular, will be of extreme importance for searches in future accelerators, as it is a unique window into the dynamics of electroweak symmetry breaking and the search for new physics beyond the SM. In the first part of this thesis (Chapters 2 to 5) we use the Minimal Composite Higgs Model (MCHM) [25], based on the symmetry breaking pattern $SO(5) \to SO(4)$, to study the production of a top pair in association with one (the $t\bar{t}h$ process) and two Higgs bosons (the $t\bar{t}hh$ process), in the context of future accelerators. The $t\bar{t}h$ process has been observed with increasing precision in recent years at the LHC [26, 27]. This process is important because it allows us to study the tth Yukawa coupling and deviations from the SM prediction of this parameter could signal the presence of new physics beyond the Standard Model. The $t\bar{t}hh$ has also been subject of initial measurements in the last years [28, 29]. It is particularly interesting because it offers a sensitive probe of the Higgs boson self-coupling. It is also important in the context of the present study, as CHMs predict charge 2/3 vector-like "top partners" that can decay in the th channel, leading to that final state. Earlier searches in this channel, as well as in tZ and bW decay channels, have already restricted these resonances. Additionally, it has been suggested [30] that measuring the tthh coupling can help distinguish between different effective operators, which cannot be differentiated by

solely measuring the tth coupling.

Given that top partner resonances are currently being actively searched for, with defined bounds above 1 TeV, we draw attention to the fact that a significant portion of the $t\bar{t}hh$ cross section often consists of non-resonant production. This non-resonant component could play an important role in discriminating between different MCHM models and is more closely tied to the pNGB nature of the Higgs boson, unlike the vector-like fermionic resonances. We emphasize the complementary relationship between non-resonant $t\bar{t}hh$ production and the $t\bar{t}h$ and hh channels, particularly in terms of measuring the trilinear Higgs couplings. We quantitatively evaluate the relative contributions of Yukawa, trilinear Higgs, and new effects to the non-resonant $t\bar{t}hh$ channel, while also examining the correlation between the $t\bar{t}h$ and $t\bar{t}hh$ cross sections.

Specifically, we present a parton-level phenomenological analysis of these processes using two MCHM fermion representations, both in current and future hadron colliders. Our objective is to highlight the phenomenological differences between a model with minimal fermion embedding (MCHM_5) and the simplest model that can support an increased top Yukawa coupling (MCHM_{14}). In addition, we provide a set of representative points that offer broad coverage of the parameter space of these models. Hence, this study serves as a valuable resource for guiding searches for new physics. Based on the current findings at the LHC, our study offers specific directions and predictions for upcoming experiments.

Usually, experimental searches consider simplified scenarios in which the widths of vector-like quarks (VLQ) are saturated by two-body decays. Furthermore, they assume that only one VLQ contributes to the final state, while others are too heavy or decay into different final states [31, 32, 33, 34, 35, 36, 37, 38, 39]. As part of our exploration of the MCHM parameter space, we find that a considerable part of it is composed of points with vector-like resonances with significant three-body decays. Therefore, in the second part of this work (Chapters 6 to 8), we focus on studying the experimental consequences of considering three-body decays on VLQ searches. First, we roughly estimate the modifications that the inclusion of three-body decays would introduce in the present mass exclusions for the lightest 2/3-charged top partner, T, and the exotic 5/3-charged top partner, $X_{5/3}$, by recasting the results on [40] and [29]. We also find that considering three-body decays implies

that different VLQs contribute to the same final state, making it difficult to isolate each contribution. However, we turn this in our advantage and propose an strategy in which we consider both contributions to enhance signal-background discrimination.

1.1 Dissertation's Outline

This thesis is structured as follows:

- In Chapter 2, we present the main general theoretical features of Composite Higgs Models and, in particular, of the MCHM_5 and the MCHM_{14}.
- In Chapter 3, we describe the phenomenological analysis approach we followed to comprehensively study the parameter space of both MCHM. It includes the definitions of High and Low Scale MCHMs, the description of the processes of interest $t\bar{t}h$ and $t\bar{t}hh$, the events generation and the parameter space scan. We finally explain how we extracted representative points from the scan.
- In Chapter 4, the Low Scale MCHM scan results are shown for the $t\bar{t}h$ and $t\bar{t}hh$ processes along with the selected representative points.
- Chapter 5 presents the results of the High Scale MCHM.
- In Chapter 6, we examine the characteristics of three body decays in the MCHM by using the scans performed previously.
- In Chapter 7, we evaluate the impact that the inclusion of three body decays in current VLQ searches would have on their mass exclusion limits.
- Chapter 8 present the proposed search strategy to guide signal extraction in experiments considering three body decays.
- We summarize the main conclusions of this dissertation in Chapter 9.

Chapters 3 to 5 correspond roughly to the work published in Chapter 9.7 of the Yellow Report [41] and the publication in [42]. Chapters 6 to 8 to the pre-print [43] (currently submitted for publication).

Chapter 2

The Higgs as a Pseudo-Nambu Goldstone Boson

Composite Higgs scenarios are characterised by the introduction of a "composite" sector with a global $\mathcal{G}$ symmetry which is spontaneously broken down to a subgroup $\mathcal{H} \subset \mathcal{G}$ generating a number of exactly massless Nambu-Goldstone Bosons (NGB) equal to the number of broken generators. These number of degrees of freedom must be enough to contain those of the Higgs field. An "elementary" sector breaks G explicitly through elementary-composite mixing terms producing a naturally light Pseudo-Nambu Goldstone Higgs boson.

The Callan–Coleman–Wess–Zumino (CCWZ) formalism is a general approach to build the Effective Lagrangian of theories with spontaneous symmetry breakdown in terms of multiplets of the unbroken $\mathcal{H}$ group. For a complete review on how Composite Models are constructed, we refer the reader to [44]. Here we show only the main features that will be used in our study. The symmetry breaking we will work with is $SO(5) \to SO(4)$, which is known as the "Minimal Composite Higgs scenario" as it possesses the minimum number of generators that could produce a Higgs field while preserving custodial symmetry. The Goldstone matrix that parametrizes the electroweak symmetry breaking, in unitary gauge, is:

$$U = \begin{pmatrix} \mathbb{1}_{3\times3} & \vec{0} & \vec{0} \\ \vec{0}^T & \cos\frac{h_0+h}{f} & \sin\frac{h_0+h}{f} \\ \vec{0}^T & -\sin\frac{h_0+h}{f} & \cos\frac{h_0+h}{f}, \end{pmatrix}, \tag{2.1}$$

where h is the Higgs boson, $h_0 = \langle h \rangle$ is its expectation value, and f is the scale at which the symmetry breaking takes place. By analogy with the theory of chiral symmetry breaking in QCD, f is also known as the "Higgs decay constant". The symbol $\mathbb{1}_{3\times3}$ represents the 3×3 identity matrix and $\vec{0}$ is a 3-dimensional null vector.

By gauging the $SU(2)_L \times U(1)_Y$ subgroup of $SO(4)$, we find the W mass to be

$$M_W^2 \;=\; \frac{1}{4}\, g^2 f^2 \sin^2 \frac{h_0}{f} \;,$$

from which we can identify the following relation between the electroweak vev (v), the scale f and h_0:

$$f \sin \frac{h_0}{f} \;\equiv\; v \;=\; 246 \text{ GeV} \;. \tag{2.2}$$

We define the parameter

$$\xi \;=\; \frac{v^2}{f^2} \;=\; \sin^2 \frac{h_0}{f} \tag{2.3}$$

which measures the departure of Composite models from the SM. The current experimental bound of the Higgs decay constant is $f \gtrsim 800$ GeV (or $\xi \lesssim 0.1$) [45, 46, 47, 48, 49, 50, 51].

As we are interested on studying the effects of this model on the $t\bar{t}h$ and $t\bar{t}hh$ processes, we will focus on the top-Higgs interactions which, in turn, depend on the composite resonances associated with the top quark. These resonances fall into representations of the $SO(5)$ group which can be further decomposed into multiplets of the unbroken $SO(4)$, with their non-degeneracy being governed by the scale f. In what follows we will focus on two scenarios:

- Resonances falling into the fundamental representation **5** of $SO(5)$ which decomposes as $\mathbf{5} = \mathbf{4} + \mathbf{1}$ under $SO(4)$
- Resonances falling into the symmetrical representation **14** of $SO(5)$ which decomposes as $\mathbf{14} = \mathbf{9} + \mathbf{4} + \mathbf{1}$ under $SO(4)$.

The first case contains the minimal number of additional fermionic degrees of freedom in Composite Higgs models, while still imposing the custodial protection of the $Z\bar{b}_L b_L$ coupling [52], which is important when considering EW precision measurements [53, 54, 55, 56, 57, 58, 59]. From now on we will denote this scenario as MCHM$_5$. The second scenario is non-minimal and has been considered in [46, 49, 60, 61, 62, 63, 64, 65, 66]. We will denote this scenario as MCHM$_{14}$. Certain Higgs couplings are enhanced w.r.t. the SM in the MCHM$_{14}$ [49, 62] while they are always suppressed in the MCHM$_5$. One of our objectives in this work is to study

the implications of these different behaviours on the $t\bar{t}h$ and $t\bar{t}hh$ searches at the HL-LHC at 14 TeV and the projected 100 TeV High Energy collider.

2.1 The Fermion Sector of the MCHM$_5$

Here, we will only describe the fermionic degrees of freedom related to the third generation of quarks, as they generate the couplings we are interested in. For a complete review, we refer the reader to [44].

The elementary sector contains the fields $q_L = (t_L, b_L)$ and t_R which have the same quantum numbers as the SM left-handed top-bottom $SU(2)_L$ doublet and the SM right-handed top $SU(2)_L$ singlet, respectively. The composite sector contains fermionic vector-like resonances that fall into the **5** representation of $SO(5)$, which, under $SO(4)$ decomposes into a fourplet Ψ_4 and a singlet Ψ_1. Their corresponding states will be denoted by:

$$\begin{aligned} \Psi_4 &\sim (X_{5/3}, X_{2/3}, T, B) \,, \\ \Psi_1 &\sim \tilde{T} \,, \end{aligned} \tag{2.4}$$

where the subindices in the X states denote their electric charge. The states T and $\tilde{T}$ have charge $2/3$ and B has charge $-1/3$. The states (T, B) transform as a $SU(2)_L$ doublet with hypercharge $Y = 1/6$, similarly to the SM quantum numbers of the elementary field q_L. The $(X_{5/3}, X_{2/3})$ states form an exotic doublet with $Y = 7/6$ and the state $\tilde{T}$ has the SM quantum numbers of t_R.

The complete Lagrangian (in the top sector) is described by:

$$\mathcal{L} = \mathcal{L}_{\text{elem}} + \mathcal{L}^{\mathbf{5}}_{\text{comp}} + \mathcal{L}^{\mathbf{5}}_{\text{mix}}, \tag{2.5}$$

where $\mathcal{L}_{\text{elem}}$ represents the elementary sector, $\mathcal{L}_{\text{comp}}$ describes the composite sector and $\mathcal{L}_{\text{mix}}$ contains the elementary-composite mixing terms. We now describe each of these terms, explicitly.

The elementary sector Lagrangian is simply written as

$$\mathcal{L}_{\text{elem}} = \bar{q}_L i \not{D} q_L + \bar{t}_R i \not{D} t_R \,, \tag{2.6}$$

where D represents the $SU(3)_C \times SU(2)_L \times U(1)_Y$ covariant derivative.

The composite sector is written directly in terms of the $SO(4)$ multiplets:

$$\begin{aligned}\mathcal{L}^{\mathbf{5}}_{\text{comp}} = \; & \overline{\Psi}_{\mathbf{4}} i(\not{D} - i\not{e})\Psi_{\mathbf{4}} - M_4 \overline{\Psi}_{\mathbf{4}}\Psi_{\mathbf{4}} + \overline{\Psi}_{\mathbf{1}} i\not{D}\Psi_{\mathbf{1}} - M_1 \overline{\Psi}_{\mathbf{1}}\Psi_{\mathbf{1}} \\ & + \left(-i\, c_L\, \overline{\Psi}_{\mathbf{4}} P_L \not{d}\, \Psi_{\mathbf{1}} - i\, c_R\, \overline{\Psi}_{\mathbf{4}} P_R \not{d}\, \Psi_{\mathbf{1}} + \text{h.c.}\right). \end{aligned} \tag{2.7}$$

where $P_{L,R} = (1 \mp \gamma_5)/2$ are the left and right projectors and c_L and c_R are couplings, expected to be order one[1]. The covariant derivative D contains only the gluon and hypercharge gauge bosons, that is, $D_\mu = \partial_\mu + ig_s G_\mu + i\frac{2}{3}g' B_\mu$. The interactions containing the remaining electroweak gauge fields come from the d_μ and e_μ symbols, which are defined through the Maurer-Cartan form

$$iU^{-1}(\partial_\mu + ig_a A^a_\mu T^a)U \;\; = \;\; d_{\mu,\hat{a}} T^{\hat{a}} + e_{\mu,a} T^a \;\equiv d_\mu + e_\mu \;\; , \tag{2.8}$$

where $T^{\hat{a}}$ are the broken generators and T^a are the generators of the unbroken $SO(4)$ group. The gauge fields A^a_μ belong to the algebra of $SO(4) \cong SU(2)_L \times SU(2)_R$ and the EW gauge fields arise when we gauge some of its associated generators: the W fields gauge $SU(2)_L$ and B_μ gauges T^3_R. Then, the hypercharge is given by $Y = 2/3 + T^3_R$ [2]. We list the all SO(5) generators, including the ones corresponding to the gauged $SU(2)_L \times U(1)_Y$, in App. A. The e_μ symbol term contains corrections to the electroweak interactions of the resonances due to compositeness. These are detailed in Appendix C. In Equation 2.7, we also have a mass term for each $SO(4)$ multiplet with the masses being M_4 for the fourplet and M_1 for the singlet. Their non-degeneracy arises from the spontaneous breaking of $SO(5)$, whose origin we do not address here, but, in our analysis, we can treat M_4 and M_1 as independent parameters.

The terms in parentheses in Eq. (2.7) introduce additional resonance-Higgs and resonance-gauge boson interactions that arises when integrating out heavy resonances not present in the low energy theory. These interactions are allowed by the model symmetries and their full expansion is shown in Appendix C. These operators do not modify the top Yukawa at tree level, as long as we assume that c_{LR} are real. Thus it

[1] If the strong sector respects parity, we expect $c_L = c_R$. We will take this as a simplifying assumption in the analysis of the **14** representation below.

[2] The factor of 2/3 arises because in order to reproduce the SM fermion hypercharges one needs to introduce an extra $U(1)_X$ factor, under which $\Psi_{\mathbf{5}}$ has charge $X = 2/3$. For further details, see [44]

has no effect on the $t\bar{t}h$ process. On the other hand, the $t\bar{t}hh$ process cross section is modified but the distributions have mainly the same shape, except for some tuned points. We will further discuss these features in Section 3.6.

Since some fermionic resonances have the same SM quantum numbers as the elementary fields, mixing terms between them are allowed. For this, it is convenient to express the elementary fields as embeddings of $SO(5)$ as:

$$Q_L^{\mathbf{5}} = \frac{1}{\sqrt{2}}\begin{bmatrix} -ib_L \\ -b_L \\ -it_L \\ t_L \\ 0 \end{bmatrix}, \quad T_R^{\mathbf{5}} = \begin{bmatrix} 0 \\ 0 \\ 0 \\ 0 \\ t_R \end{bmatrix}, \tag{2.9}$$

and $\mathbf{\Psi_4}$ and $\mathbf{\Psi_1}$ as (see Appendix B for further details)

$$\mathbf{\Psi_4} = \frac{1}{\sqrt{2}}\begin{bmatrix} -iB + iX_{5/3} \\ -B - X_{5/3} \\ -iT - iX_{2/3} \\ T - X_{2/3} \\ 0 \end{bmatrix}, \quad \mathbf{\Psi_1} = \begin{bmatrix} 0 \\ 0 \\ 0 \\ 0 \\ \tilde{T} \end{bmatrix}. \tag{2.10}$$

Then, the mass mixing Lagrangian is written as

$$\begin{aligned} \mathcal{L}_{\text{mix}}^{\mathbf{5}} &= f\,\overline{Q}_L^{\mathbf{5}} U \left[y_{L4}\mathbf{\Psi_4} + y_{L1}\mathbf{\Psi_1}\right] + \text{h.c.} \\ &+ f\,\overline{T}_R^{\mathbf{5}} U \left[y_{R4}\mathbf{\Psi_4} + y_{R1}\mathbf{\Psi_1}\right] + \text{h.c.} \end{aligned} \tag{2.11}$$

which implements the *partial compositeness* hypothesis [67].

Therefore, in the $\{\bar{t}_L,\ \overline{T}_L,\ \overline{X}_{2/3,L},\ \overline{\tilde{T}}_L\}$ vs $\{t_R,\ T_R,\ X_{2/3,R},\ \tilde{T}_R\}$ basis, the charge 2/3 mass matrix is given by

$$\mathcal{M}_{2/3}^{\mathbf{5}} = \begin{bmatrix} 0 & \frac{1}{2}y_{L4}f(1+\sqrt{1-\xi}) & \frac{1}{2}y_{L4}f(1-\sqrt{1-\xi}) & \frac{1}{\sqrt{2}}y_{L1}f\sqrt{\xi} \\ -\frac{1}{\sqrt{2}}y_{R4}f\sqrt{\xi} & -M_4 & 0 & 0 \\ \frac{1}{\sqrt{2}}y_{R4}f\sqrt{\xi} & 0 & -M_4 & 0 \\ y_{R1}f\sqrt{1-\xi} & 0 & 0 & -M_1 \end{bmatrix}. \tag{2.12}$$

Diagonalization of this matrix leads to the physical fermion eigenstates, which are in general admixtures of the original elementary and composite states. The lightest one is identified with the observed top quark. Our numerical analysis follows from this mass matrix, as described in subsequent sections. The remaining resonances have masses

$$X_{5/3}: \qquad M_{X_{5/3}} = M_4 \ , \tag{2.13}$$

$$B: \qquad M_B = \sqrt{M_4^2 + y_{L4}^2 f^2} \ . \tag{2.14}$$

2.2 The Fermion Sector of the MCHM$_{14}$

The MCHM$_{14}$ scenario assumes the resonances fall into the **14** symmetric representation of $SO(5)$. Under $SO(4)$, the representation decomposes as a singlet, $\mathbf{\Psi_1}$, a fourplet, $\mathbf{\Psi_4}$, and a nonet, $\mathbf{\Psi_9}$. The first two are described in Eq. (2.4). We describe the states in $\mathbf{\Psi_9}$ as:

$$\mathbf{\Psi_9} \ \sim \ (U_{8/3}, U_{5/3}, U_{2/3}, V_{5/3}, V_{2/3}, V_{-1/3}, F_{2/3}, F_{-1/3}, F_{-4/3}) \ . \tag{2.15}$$

Under $SU(2)_L$, this nonet breaks into three triplets, U with $Y = 5/3$, V with $Y = 2/3$ and F with $Y = -1/3$.

The complete Lagrangian of the MCHM$_{14}$ (in the top sector) is decribed by:

$$\mathcal{L} \ = \ \mathcal{L}_{\rm elem} + \mathcal{L}^{\mathbf{14}}_{\rm comp} + \mathcal{L}^{\mathbf{14}}_{\rm mix}, \tag{2.16}$$

where the elementary sector, $\mathcal{L}_{\rm elem}$, is given by Eq. (2.6). The composite sector is obtained adding the kinematic and mass terms for the nonet $\mathbf{\Psi}_9$ (the precise structure of $\mathbf{\Psi}_9$ is given in App. B) to Eq. (2.7). Additionally the inclusion of the nonet allows new terms involving the d_μ symbol. Then we have:

$$\begin{aligned}
\mathcal{L}^{\mathbf{14}}_{\rm comp} \ &= \ \overline{\mathbf{\Psi}}_{\mathbf{4}} i(\not{D} - i\not{e}) \mathbf{\Psi_4} - M_4 \overline{\mathbf{\Psi}}_{\mathbf{4}} \mathbf{\Psi_4} + \overline{\mathbf{\Psi}}_{\mathbf{1}} i \not{D} \mathbf{\Psi_1} - M_1 \overline{\mathbf{\Psi}}_{\mathbf{1}} \mathbf{\Psi_1} \\
&+ \ {\rm Tr}\left[\overline{\mathbf{\Psi}}_{\mathbf{9}} \left(i \not{D} \mathbf{\Psi_9} - i\left[\not{e}, \mathbf{\Psi_9}\right]\right)\right] - M_9 {\rm Tr}\left[\overline{\mathbf{\Psi}}_{\mathbf{9}} \mathbf{\Psi_9}\right] \\
&+ \ \left(-i\, c_4\, \overline{\mathbf{\Psi}}_4 \not{d}\, \mathbf{\Psi}_1 - i\, c_9\, \overline{\mathbf{\Psi}}^{ij}_{\mathbf{9}} \not{d}^i\, \mathbf{\Psi}^j_{\mathbf{4}} - i\, \frac{c_{T9}}{4\pi f}\, \overline{\mathbf{\Psi}}^{ij}_{\mathbf{9}}\, d^i_\mu d^{j\,\mu}\, \tilde{T} + {\rm h.c.}\right),
\end{aligned} \tag{2.17}$$

where c_4, c_9 and c_{T9} are couplings of order one and i and j are $SO(4)$ indices. We are assuming, for simplicity, that the strong sector respects parity symmetry. Since

the interaction term between $\mathbf{\Psi_9}$ and $\tilde{T}$ is suppressed by an extra power of the cutoff $\Lambda \lesssim 4\pi f$, we expect it to be subdominant. The explicit form of the terms including the d_μ and e_μ symbols are reported in Appendix C.

The $\mathcal{L}^{\mathbf{14}}_{\rm mix}$ term in Eq. (2.17) accounts for the mixing between the elementary and composite states. To write it down, it is convenient to embed the elementary and composite states into **14** representations of $SO(5)$, similarly to what was done for the **5** scenario. We denote the elementary embeddings by $Q^{\mathbf{14}}_L$ and $T^{\mathbf{14}}_R$ and continue using the notation $\mathbf{\Psi_9}$, $\mathbf{\Psi_4}$ and $\mathbf{\Psi_1}$ for the composite embeddings. These are 5×5 traceless symmetric matrices and are given in Appendix B. Then, we have

$$\begin{aligned}\mathcal{L}^{\mathbf{14}}_{\rm mix} &= f\,\mathrm{Tr}\left[U^{\mathsf{T}}\overline{Q}^{\mathbf{14}}_L U\left(y_{L9}\mathbf{\Psi_9}+y_{L4}\mathbf{\Psi_4}+y_{L1}\mathbf{\Psi_1}\right)\right]+\text{h.c.}\\ &+ f\,\mathrm{Tr}\left[U^{\mathsf{T}}\overline{T}^{\mathbf{14}}_R U\left(y_{R9}\mathbf{\Psi_9}+y_{R4}\mathbf{\Psi_4}+y_{R1}\mathbf{\Psi_1}\right)\right]+\text{h.c.}\end{aligned} \tag{2.18}$$

Thus, the charge $2/3$ mass matrix in the $\{\bar{t}_L,\ \overline{T}_L,\ \overline{X}_{2/3,L},\ \overline{\tilde{T}}_L,\ \overline{U}_{2/3,L},\ \overline{V}_{2/3,L},\ \overline{F}_{2/3,L}\}$ vs $\{t_R,\ T_R,\ X_{2/3,R},\ \tilde{T}_R,\ U_{2/3,R},\ V_{2/3,R},\ F_{2/3,R}\}$ basis is given by:

$$\mathcal{M}^{\mathbf{14}}_{2/3} = \tag{2.19}$$

$$\begin{bmatrix} 0 & \frac{1}{2}y_{L4}fa_+ & -\frac{1}{2}y_{L4}fa_- & -\frac{\sqrt{5}}{4}y_{L1}fs_{2h} & -\frac{1}{2}y_{L9}fb_- & -\frac{1}{2}y_{L9}fs_{2h} & \frac{1}{4}y_{L9}fb_+ \\ \frac{\sqrt{5}}{4}y_{R4}fs_{2h} & -M_4 & 0 & 0 & 0 & 0 & 0 \\ -\frac{\sqrt{5}}{4}y_{R4}fs_{2h} & 0 & -M_4 & 0 & 0 & 0 & 0 \\ y_{R1}f\left(1-\frac{5}{4}s_h^2\right) & 0 & 0 & -M_1 & 0 & 0 & 0 \\ \frac{\sqrt{5}}{4}y_{R9}fs_h^2 & 0 & 0 & 0 & -M_9 & 0 & 0 \\ -\frac{\sqrt{5}}{4}y_{R9}fs_h^2 & 0 & 0 & 0 & 0 & -M_9 & 0 \\ \frac{\sqrt{5}}{4}y_{R9}fs_h^2 & 0 & 0 & 0 & 0 & 0 & -M_9 \end{bmatrix}, \tag{2.20}$$

where

$$s_h^2=\xi\ ,\quad s_{2h}=2\sqrt{\xi}\sqrt{1-\xi}\ ,\quad a_\pm=1\pm\sqrt{1-\xi}-2\xi\ ,\quad b_\pm=\sqrt{\xi}\left(1\pm\sqrt{1-\xi}\right)\ .$$

The charge $-1/3$ mass matrix in the $\{\bar{b}_L,\ \overline{B}_L,\ \overline{V}_{-1/3,L},\ \overline{F}_{-1/3,L}\}$ vs $\{B_R,\ V_{-1/3,R},\ F_{-1/3,R}\}$ basis takes the form

$$\mathcal{M}^{\mathbf{14}}_{-1/3} = \begin{bmatrix} y_{L4}f\sqrt{1-\xi} & -\frac{1}{\sqrt{2}}y_{L9}f\sqrt{\xi} & \frac{1}{\sqrt{2}}y_{L9}f\sqrt{\xi} \\ -M_4 & 0 & 0 \\ 0 & -M_9 & 0 \\ 0 & 0 & -M_9 \end{bmatrix}. \tag{2.21}$$

The remaining states have masses

$$X_{5/3}: \qquad M_{X_{5/3}} = M_4 \ , \tag{2.22}$$

$$U_{8/3}, U_{5/3}, V_{5/3}, F_{-4/3}: \qquad M_{U_{8/3}} = M_{U_{5/3}} = M_{V_{5/3}} = M_{F_{-4/3}} = M_9 \tag{2.23}$$

2.3 Partial Compositeness and Higgs Couplings

The described models incorporate the partial compositeness paradigm of [67] via linear mixing of the elementary fields q_L and t_R with composite operators transforming as singlets, fourplets or nonets of the $SO(4)$ symmetry as described by Eqs. (2.11) and (2.18). In addition to giving rise to the top mass, the same operators are responsible for the top-Higgs Yukawa coupling, which is of central importance to this work.

We describe the mechanism in Figure 2.1. The green boxes represent insertions of the Higgs field doublet (see Eq. (B.2)) in Eqns. (2.11) and (2.18), to leading order in H/f. For instance, the mixing between $\mathbf{\Psi}_1$ and T_R can happen at 0-th order in H, while the $\mathbf{\Psi}_1$-Q_L mixing requires an insertion of the Higgs field transforming as a $\mathbf{4}$ of $SO(4)$: $\mathbf{4}_{Q_L} \otimes \mathbf{4}_H \supset \mathbf{1}$. Similarly, the mixing between the fourplet $\mathbf{\Psi}_4$ and Q_L can happen at 0-th order in H, but requires an H-insertion when mixing with T_R: $\mathbf{4}_{\Psi_4} \otimes \mathbf{4}_H \supset \mathbf{1}$. Both of these cases lead to a linear, SM-like coupling $\bar{q}_L \tilde{H} t_R$, up to corrections non-linear in H.

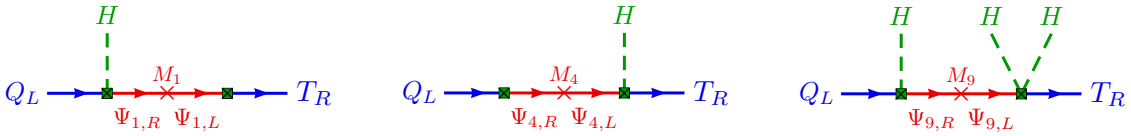

Figure 2.1: Top-Higgs Yukawa coupling through mixing with singlet, 4-plet and nonet resonances (the mixing is represented by the green squares). The first two cases lead to a SM-like coupling to the Higgs (for $H \ll f$), while the nonet exchange leads to a cubic, non-renormalizable coupling $\bar{q}_L \tilde{H} t_R H^\dagger H$, at leading order in H/f.

Mixing the nonet $\mathbf{\Psi_9}$ with the elementary fields is qualitatively different. While it requires one Higgs field insertion for the mixing Q_L-$\mathbf{\Psi}_9$ ($\mathbf{4}_{Q_L} \otimes \mathbf{4}_H \otimes \mathbf{9}_{\Psi_9}$), two insertions are needed for the mixing T_R-$\mathbf{\Psi}_9$ ($\mathbf{4}_H \otimes \mathbf{4}_H \otimes \mathbf{9}_{\Psi_9} \supset \mathbf{1}$). In this case, the leading order coupling is the non-SM like, non-renormalizable operator $\bar{q}_L \tilde{H} t_R H^\dagger H$.

To get the top Yukawa interaction we replace H by its vev, which, in unitary gauge is:

$$H = \frac{1}{\sqrt{2}} \begin{pmatrix} 0 \\ h_0 + h \end{pmatrix} \tag{2.24}$$

and take the term linear in h. From the operators described above, the top Yukawa strength gets a factor 1 when induced by the linear operator and a factor 3 when induced by the cubic operator. Therefore, when various channels are present simultaneously, the top Yukawa can be enhanced w.r.t the SM. Additionally, when $M_1 = M_4$, the leading term is cubic.

The same effect has an impact on the coupling of the Higgs to two gluons (ggh), normalized to the SM top contribution, which is given by:

$$c_g \;=\; \frac{v}{2}\frac{d}{dh_0}\log\det\left(\mathcal{M}^\dagger\mathcal{M}\right) \;, \tag{2.25}$$

where $\mathcal{M}$ is the fermion mass matrix, assuming all states are much heavier than the Higgs boson (for our purposes, light state contributions can be neglected).

For the MCHM$_5$, using $\mathcal{M} = \mathcal{M}^{\mathbf{5}}_{2/3}$ in Eq. (2.12), this gives

$$c_g^{\mathbf{5}} \;=\; \frac{1-2\xi}{\sqrt{1-\xi}} \;. \tag{2.26}$$

For the MCHM$_{14}$, one gets

$$c_g^{\mathbf{14}} \;=\; c_g^t + c_g^b \;, \tag{2.27}$$

where

$$c_g^t = \frac{4\,(1-r_1)\,r_9 - \left[(21-3\sqrt{\xi-1})/2\,r_1 + 23 r_9 - 32 r_1 r_9\right]\xi + 4\,(7/2\,r_1 + 5 r_9 - 8 r_1 r_9)\,\xi^2}{r_1/2\,\xi + \sqrt{1-\xi}\,[4\,(1-r_1)\,r_9 - (7/2\,r_1 + 5 r_9 - 8 r_1 r_9)\,\xi]} \;, \tag{2.28}$$

arises from the charge $2/3$ sector, $\mathcal{M}^{\mathbf{14}}_{2/3}$ in Eq. (2.20), and

$$c_g^b \;=\; \xi\sqrt{1-\xi}\,\frac{y_L^2 f^2\left(1-r_9^2\right)}{r_9^2\,(M_4^2 + y_L^2 f^2) + y_L^2 f^2\,(1-r_9^2)\,\xi} \;, \tag{2.29}$$

arises from the charge $-1/3$ sector, $\mathcal{M}^{\mathbf{14}}_{-1/3}$ in Eq. (2.21). For the latter, we explicitly removed the zero-mode (the physical bottom quark) and neglected its contribution

to the ggh coupling. In Eqns. (2.28) and (2.29) we defined $r_1 = M_1/M_4$ and $r_9 = M_9/M_4$ and we assume $y_{Li} \equiv y_L$ and $y_{Ri} \equiv y_R$ for $i = 1, 4, 9$ (see Section 3.1).

When $M_1 = M_4$ or in the limit $r_9 \to 0$ with r_1, ξ fixed (but not for small non-zero M_9), one finds

$$c_g^t \;\approx\; 3 - \frac{8}{3}\,\xi \;, \tag{2.30}$$

while

$$c_g^t \;=\; 1 - \frac{3r_1 + 8r_9 - 11 r_1 r_9}{2\,(1-r_1)\,r_9}\,\xi + \mathcal{O}(\xi^2) \tag{2.31}$$

in all other cases, reflecting the underlying cubic versus linear coupling of the top quark to the Higgs field. In all cases, $c_g^b \sim \xi \ll 1$. Global constraints on the gluon fusion process from Higgs measurements, which allow for about 20% deviations from unity in c_g at the 95% C.L. [68], will then also impose constraints on the allowed deviations in the top Yukawa coupling from the SM limit. We should note that the large enhancement shown in Eq. (2.30) actually happens in a region of parameter space where the top mass cannot be generated for perturbative values of $y_{L,R}$. We can see this from the approximate expressions for the top mass in the MCHM$_5$ and in the MCHM$_{14}$, given by

$$\begin{aligned} m_t^{\mathbf{5}} &\approx \frac{1}{\sqrt{2}}\sqrt{\xi}\sqrt{1-\xi}\,\frac{y_L y_R f^2}{\sqrt{Z_L Z_R}|M_1|}\,|1-r_1| \\ m_t^{\mathbf{14}} &\approx \frac{\sqrt{5}}{2}\sqrt{\xi}\sqrt{1-\xi}\,\frac{y_L y_R f^2}{\sqrt{Z_L Z_R}|M_1|}\left|1 - r_1 - \frac{3r_1 + 5r_9 - 8 r_1 r_9}{4 r_9}\,\xi\right| \;, \end{aligned} \tag{2.32}$$

where $y_{Li} \equiv y_L$ and $y_{Ri} \equiv y_R$ for $i = 1, 4, 9$ (see Section 3.1). The "wavefunction renormalization" factors have the form $Z_{L,R} = 1 + y_{L,R}^2 f^2/M_{4,1}^2 + \mathcal{O}(\xi)$.

2.4 Higgs Decays

The amplitudes of the processes we are interested in ($t\bar{t}h$ and $t\bar{t}hh$) are completely determined by the Lagrangians so far described. However, in order to consider the possible modifications of the Higgs decays, we must specify how the light families of quarks and leptons are introduced in Composite Higgs models. These modifications

are expected to be small, as the observed 125 GeV Higgs has SM-like properties. Then, the dominant Higgs decays are $h \to b\bar{b}, W^+W^-, gg, \tau^+\tau^-, c\bar{c}, ZZ$ like in the SM. We are neglecting the decays into channels with low branching ratios (BR) as $\gamma\gamma$ (BR= 0.23%), γZ (BR= 0.15%) and $\mu^+\mu^-$ (BR= 0.002%) or even rarer decay channels.

$H \to b\bar{b}$ is the most important decay channel (with about BR= 58%). To define its value, we still need to implement the b_R state, as b_L was already implemented along with the t_L state in a $SO(5)$ representation. Among several possibilities we choose to embed b_R in a **10** representation of $SO(5)$ and mix it with composite resonances in the same representations in both MCHM_5 and MCHM_{14} models. These models were introduced in [46] and were called $\text{MCHM}_{5,5,10}$ and $\text{MCHM}_{14,14,10}$. The remaining parts of lepton and quark sectors are chosen to follow the same implementation.

Under the previous assumptions, it is found that the couplings of the composite Higgs to the vector bosons and to light $f\overline{f}$ pairs are controlled by two model-dependent functions that depend only on ξ. In the MCHM_5 the coupling of the Higgs to a pair of gluons depends also only on ξ, but in the MCHM_{14} it depends on additional microscopic parameters, as shown in Section 2.3.

The partial widths are then simply obtained by rescaling the SM ones. For the MCHM_5, one finds [46]

$$\begin{aligned}
\Gamma(h \to b\bar{b}) &= F_2(\xi)^2\, \Gamma_{\text{SM}}(h \to b\bar{b}) \,, \\
\Gamma(h \to c\bar{c}) &= F_1(\xi)^2\, \Gamma_{\text{SM}}(h \to c\bar{c}) \,, \\
\Gamma(h \to \tau^+\tau^-) &= F_2(\xi)^2\, \Gamma_{\text{SM}}(h \to \tau^+\tau^-) \,, \\
\Gamma(h \to VV) &= F_2(\xi)^2\, \Gamma_{\text{SM}}(h \to VV) \,, \\
\Gamma(h \to gg) &= F_1(\xi)^2\, \Gamma_{\text{SM}}(h \to gg) \,,
\end{aligned} \tag{2.33}$$

where

$$F_1(\xi) = \frac{1-2\xi}{\sqrt{1-\xi}} \,, \qquad F_2(\xi) = \sqrt{1-\xi} \,. \tag{2.34}$$

For the MCHM_{14}, the bottom channel is controlled by F_1 instead of F_2, and the ggh

coupling is controlled by $c_g^{\mathbf{14}}$ of Eq. (2.27) instead of $F_1(\xi)$.

The total Higgs width in the MCHM models under consideration can then be written as

$$\begin{aligned}\Gamma_5(h) &= \Big\{F_2(\xi)^2\left[\mathrm{BR}_{\mathrm{SM}}(\mathrm{b\bar{b}})+\mathrm{BR}_{\mathrm{SM}}(\mathrm{VV})+BR_{\mathrm{SM}}(\tau^+\tau^-)\right] \\ &\quad + F_1(\xi)^2\left[\mathrm{BR}_{\mathrm{SM}}(\mathrm{gg})+\mathrm{BR}_{\mathrm{SM}}(\mathrm{c\bar{c}})\right]\Big\}\,\Gamma_{\mathrm{SM}}(h)\ , \qquad (2.35)\\ \Gamma_{14}(h) &= \Big\{F_2(\xi)^2\left[\mathrm{BR}_{\mathrm{SM}}(\mathrm{VV})+\mathrm{BR}_{\mathrm{SM}}(\tau^+\tau^-)\right] \\ &\quad + F_1(\xi)^2\left[\mathrm{BR}_{\mathrm{SM}}(\mathrm{b\bar{b}})+\mathrm{BR}_{\mathrm{SM}}(\mathrm{c\bar{c}})\right]+(c_g^{\mathbf{14}})^2\,\mathrm{BR}_{\mathrm{SM}}(\mathrm{gg})\Big\}\,\Gamma_{\mathrm{SM}}(h)\ , \qquad (2.36)\end{aligned}$$

and the branching fractions can also be expressed in terms of the functions F_1, F_2, $c_g^{\mathbf{14}}$, and SM quantities.

Chapter 3

Phenomenological Analysis Strategy

3.1 Parameter Space

From Section 2.1, we can see that the top sector of the MCHM$_5$ is controlled by 8 parameters: the masses M_i, and the dimensionless parameters y_{Li}, y_{Ri}, c_L and c_R for $i = 1, 4$. In the case of the MCHM$_{14}$ (see Section 2.2), we have 12 parameters: M_i, y_{Li}, y_{Ri}, c_4, c_9 and c_{T9} for $i = 1, 4, 9$. These parameters are complex, a priori. However not all phases are physical and some of them can be absorbed into convenient field redefinitions, keeping only the physical ones.

Since the process of absorbing unphysical phases are similar in both MCHM scenarios, we will only describe it explicitly for the simpler MCHM$_5$ case. From Eqs. (2.7) and (2.11), let us take the following terms:

$$\begin{aligned}
\mathcal{L}_{\text{redef}} \;=\; & \overline{\Psi}_1 i\not{D}\Psi_1 - M_1\overline{\Psi}_{1,L}\Psi_{1,R} - M_1^*\overline{\Psi}_{1,R}\Psi_{1,L} \\
& + \overline{\Psi}_4 i\not{D}\Psi_4 - M_4\overline{\Psi}_{4,L}\Psi_{4,R} - M_4^*\overline{\Psi}_{4,R}\Psi_{4,L} \\
& + f\,\overline{Q}_L^{\mathbf{5}} U\left[y_{L4}\Psi_{\mathbf{4}} + y_{L1}\Psi_{\mathbf{1}}\right] + \text{h.c.} \\
& + f\,\overline{T}_R^{\mathbf{5}} U\left[y_{R4}\Psi_{\mathbf{4}} + y_{R1}\Psi_{\mathbf{1}}\right] + \text{h.c.}
\end{aligned} \tag{3.1}$$

Here, we are considering complex M_i's. After all redefinitions we will end up with real M_i's as in Eq. (2.7). Notice also that we are not including the terms containing c_L and c_R. This is because, after all phase absorptions, the remaining phases can be easily included in redefinitions of these parameters.

We can write the parameters in Eq. (3.1) in terms of their magnitudes and phases

as:

$$M_i = |M_i| e^{i\theta_{M_i}} \tag{3.2}$$

$$y_{Li} = |y_{Li}| e^{i\theta_{Li}} \tag{3.3}$$

$$y_{Ri} = |y_{Ri}| e^{i\theta_{Ri}} \tag{3.4}$$

Let us start by absorbing the phase of each y_{Li}. The corresponding terms can be written as:

$$\mathcal{L}_{\text{redef}} \subset f|y_{Li}| e^{i\theta_{Li}} \overline{Q}^5_L U(\Psi_{i,L} + \Psi_{i,R}) = f|y_{Li}| e^{i\theta_{Li}} \overline{Q}^5_L U \Psi_{i,R} \tag{3.5}$$

If we make the redefinition $\Psi_{i,L,R} \to e^{-i\theta_{Li}} \Psi_{i,L,R}$, the kinetic and mass terms in Eq. (3.1) remain invariant. The phases only appear in the terms containing y_{Ri}'s. Thus, we have:

$$\begin{aligned}
\mathcal{L}_{\text{redef}} \;=\; & \overline{\Psi}_1 i \not{D} \Psi_1 - M_1 \overline{\Psi}_{1,L} \Psi_{1,R} - M_1^* \overline{\Psi}_{1,R} \Psi_{1,L} \\
& + \overline{\Psi}_4 i \not{D} \Psi_4 - M_4 \overline{\Psi}_{4,L} \Psi_{4,R} - M_4^* \overline{\Psi}_{4,R} \Psi_{4,L} \\
& + f\, \overline{Q}^{\mathbf{5}}_L U \left[|y_{L4}| \Psi_{\mathbf{4}} + |y_{L1}| \Psi_{\mathbf{1}} \right] + \text{h.c.} \\
& + f\, \overline{T}^{\mathbf{5}}_R U \left[y_{R4} e^{-i\theta_{L4}} \Psi_{\mathbf{4}} + y_{R1} e^{-i\theta_{L1}} \Psi_{\mathbf{1}} \right] + \text{h.c.}
\end{aligned} \tag{3.6}$$

Let us proceed absorbing the phase of each M_i. For this, we can make the redefinitions $\Psi_{i,L} \to e^{-i\theta_{M_i}} \Psi_{i,L}$ to end up with:

$$\begin{aligned}
\mathcal{L}_{\text{redef}} \;=\; & \overline{\Psi}_1 i \not{D} \Psi_1 - |M_1| \overline{\Psi}_1 \Psi_1 \\
& + \overline{\Psi}_4 i \not{D} \Psi_4 - |M_4| \overline{\Psi}_4 \Psi_4 \\
& + f\, \overline{Q}^{\mathbf{5}}_L U \left[|y_{L4}| \Psi_{\mathbf{4}} + |y_{L1}| \Psi_{\mathbf{1}} \right] + \text{h.c.} \\
& + f\, \overline{T}^{\mathbf{5}}_R U \left[y_{R4} e^{-i\theta_{L4}} \Psi_{\mathbf{4}} + y_{R1} e^{-i\theta_{L1}} \Psi_{\mathbf{1}} \right] + \text{h.c.}
\end{aligned} \tag{3.7}$$

where now $\Psi_i \equiv \Psi_{i,R} + e^{-i\theta_{M_i}} \Psi_{i,L}$. Finally we can absorb the phase of one of the remaining y_{Ri}, let's say y_{R4}. The corresponding terms are written as:

$$\mathcal{L}_{\text{redef}} \subset f\, \overline{T}^{\mathbf{5}}_R U \left[|y_{R4}| e^{i\theta_{R4}} e^{-i\theta_{L4}} \Psi_{\mathbf{4}} \right] \tag{3.8}$$

If we make the redefinition $T^5_R \to e^{i(\theta_{R4}-\theta_{L4})}T^5_R$ we finally obtain

$$\begin{aligned}\mathcal{L}_{\text{redef}} \;=\; & \overline{\Psi}_1 i\not{D}\Psi_1 - |M_1|\overline{\Psi}_1\Psi_1 \\ & + \overline{\Psi}_4 i\not{D}\Psi_4 - |M_4|\overline{\Psi}_4\Psi_4 \\ & + f\,\overline{Q}^{\mathbf{5}}_L U\left[|y_{L4}|\Psi_{\mathbf{4}} + |y_{L1}|\Psi_{\mathbf{1}}\right] + \text{h.c.} \\ & + f\,\overline{T}^{\mathbf{5}}_R U\left[|y_{R4}|\Psi_{\mathbf{4}} + y_{R1}e^{i(\theta_{L4}-\theta_{R4}-\theta_{L1})}\Psi_{\mathbf{1}}\right] + \text{h.c.}\end{aligned} \tag{3.9}$$

So, we remain with three physical phases for the MCHM$_5$: those of c_L, c_R and y_{R1}. Following an analogous procedure, we can deduce that the MCHM$_{14}$ contains five physical phases: c_4, c_9, c_{T9} and two of the y_{Ri}'s. Alternatively, we can put the phases in M_1, c_L and c_R for the MCHM$_5$ and in M_1, M_4, c_4, c_9 and c_{T9} for the MCHM$_{14}$. For simplicity, we will assume that the CP symmetry is conserved in the strong sector[1]. Thus, we consider all parameters to be real. With this, we are left with three unfixed physical signs for the MCHM$_5$ (sign(M_1), sign(c_L) and sign(c_R)) and five unfixed physical signs for the MCHM$_{14}$ (sign(M_1), sign(M_4), sign(c_4), sign(c_9) and sign(c_{T9})). The effect of the operators controlled by the parameters c_L and c_R will be analysed in Section 3.6. There, we will see, that, in our analysis, we can neglect them. Therefore, we are finally left only with the M_i, y_{Li} and y_{Ri} parameters.

In the $SO(5)$ symmetric limit we have $M_1 = M_4$, $y_{L1} = y_{L4}$ and $y_{R1} = y_{R4}$ for the MCHM$_5$ case and $M_1 = M_4 = M_9$, $y_{L1} = y_{L4} = y_{L9}$ and $y_{R1} = y_{R4} = y_{R9}$ for the MCHM$_{14}$. When these equalities do not hold, the $SO(5)$ symmetry breaks to $SO(4)$. In the case of the mass parameters, this breaking is "soft", that is, the Higgs effective potential is not sensitive to UV scales. However, in the case of the dimensionless couplings y_{Li} and y_{Ri}, deviations from the $SO(5)$ symmetry leads to a UV sensitive Higgs potential, which can deviate the Higgs mass from its measured value of 125 GeV. For this reason, and to simplify the number of model's free parameters, we choose to focus on cases where:

$$y_{Li} \equiv y_L \;, \qquad y_{Ri} \equiv y_R \;, \tag{3.10}$$

for all i. In conclusion, we are left with the following set of parameters:

- MCHM$_5$: f, $|M_1|$, $|M_4|$, sign(M_1), y_L and y_R.

[1] It is also worth noting that not imposing CP conservation leads to severe constraints. These (as well as the flavor structure of the models) are beyond the scope of our analysis, and we refer the reader to [69] for an example of a composite Higgs model addressing these issues.

- MCHM$_{14}$: f, $|M_1|$, $|M_4|$, $|M_9|$, sign(M_1), sign(M_4), y_L and y_R.

One of these parameters (we choose it to be y_R) can be further fixed if we require to reproduce the top mass. Therefore, we demand that:

$$\text{Det}(\mathcal{M}_{2/3}\mathcal{M}_{2/3}^T - \overline{m}_t^2 \mathbb{1}) = 0 \ , \tag{3.11}$$

This equation is solved numerically for y_R for each chosen set of the other parameter values. If no real solution is found, the parameter space point is discarded. For instance, in the $SO(5)$ symmetric limit, the determinants of the mass matrices in Eqns. 2.12 and 2.20 are zero. Therefore, the top mass cannot be reproduced, as expected in the absence of the $SO(5) \to SO(4)$ symmetry breaking. Consequently points near the $SO(5)$ limit will hardly accommodate the observed top mass.

In Eq. (3.11), we are considering $\overline{m}_t$ to be the running top mass at the resonances scale (around 2-3 TeV), that is, $\overline{m}_t = 150$ GeV[2]. While this running top mass is considered when diagonalizing the mass matrices, at the scale of the processes of interest, $\bar{t}th$ and $t\bar{t}hh$, which is around 200 GeV, we consider the pole top mass, $m_t = 173$ GeV.

To extract the physical quantities for a particular point in the parameter space defined by the values of M_i and y_L, we first find the value of y_R that satisfy Eq. (3.11). Then, the mass matrix is diagonalized using the unitary transformations U_L and U_R in such a way that:

$$U_L \mathcal{M}_{2/3} U_R^\dagger = \text{diag}(m_t, M_{T^{(1)}}, , M_{T^{(2)}}, \ldots) \ , \tag{3.12}$$

The non-null elements of the diagonal matrix in Eq. (3.12) represent the spectrum of the model, with all these masses being real and positive. This process is done with Mathematica [70]. The charge $-1/3$ sector of the MCHM$_{14}$ follows the same process[3]. The physical spectrum and the elements of U_L and U_R are then passed as inputs for the next steps of the analysis.

[2]Later, in section 5, we will consider resonances with masses up to tens of TeV, such that strictly speaking, a different running top mass should be picked depending on the energy reached in each parameter space point. However, we find that the effect of the choice of top mass at this scale is negligible and would be masked in comparison with the spread in physical parameters obtained from the numerical scan, so we simply fix $\overline{m}_t = 150$ GeV.

[3]The bottom mass in Eq. (2.21) vanishes. Although one can easily incorporate a finite bottom mass, its effect in the diagonalization is negligible. The correct couplings between the Higgs boson and the bottom quark are taken into account as described in Section 2.4.

Quantities as the Yukawa matrix in the mass eigenbasis can be computed from the rotation matrices as:

$$Y_{2/3}^{\text{mass}} = U_L Y_{2/3}^{\text{gauge}} U_R^{\dagger} \,, \tag{3.13}$$

where

$$Y_{2/3}^{\text{gauge}} \;=\; \frac{d}{dh}\mathcal{M}_{2/3} \tag{3.14}$$

is the Yukawa matrix in the gauge eigenbasis. The $(1,1)$ entry of $Y_{2/3}^{\text{mass}}$ corresponds to the top Yukawa coupling. It includes all tree-level effects arising from the Higgs compositeness and the mixing with the vector-like resonances.

Since the mass matrices depend non-linearly in h (through $\sqrt{\xi} = \sin\frac{h_0+h}{f}$), couplings between two tops and a number of Higgs bosons arise. In our analysis, in particular, the coupling $t\bar{t}hh$ will be of importance. The Feynman rule associated to this coupling is equal to i times the $(1,1)$ entry of $\frac{1}{2}d^2\mathcal{M}_{2/3}/dh^2$, after rotating it to the mass eigenbasis.

3.2 MCHM Scales, low versus high

The aim of this work is to study the parameter space of both MCHM_5 and MCHM_{14} at two different scales that are motivated by future planned or projected experimental searches. Therefore, we divide the analysis in two parts.

The first part considers the parameter space relevant to the experimental reach of the LHC accelerator in the near future which includes two operational run stages: the current Run-3 stage planned to finish in 2026, with a total integrated luminosity of around 400 fb^{-1} at a CM energy of $13-14$ TeV, and the HL-LHC stage planned to start operations in 2028 with a luminosity 10 times higher and a CM energy of 14 TeV or slightly higher. The region of the parameter space that covers this scale will be called "Low Scale MCHM" (LS-MCHM). This will be the focus of the rest of this chapter and of Chapter 4.

In the second part we consider the region of the parameter space that is relevant to projected future colliders expected to operate at energies around $\sqrt{s} = 100$ TeV or higher [15, 17, 71]. We label this region as the "High Scale MCHM" (HS-MCHM)

and will be the subject of Chapter 5. To study a point in the High scale MCHM we require any of the following situations:

1. No new physics (in terms of mass or precision reach) is discovered at the HL-LHC.

2. Some evidence (at 3σ effect) is found at the HL-LHC. This can be a new high mass resonance or a $\mu(t\bar{t}h)$ deviation from the SM.

3. A deviation on $\mu(t\bar{t}h)$ is present at 5σ and $\mu(t\bar{t}hh)$ is observed, but with sizeable uncertainty. A higher energy pp collider would allow higher precision measurements and looking for further effects.

It is worth stressing that, although the Low Scale MCHM points are studied at $\sqrt{s} = 14$ TeV, we also simulate them at 100 TeV and 150 TeV to account for the cases in which the point passes one of the listed situations above. Therefore some results in Chapter 4 will also show quantities simulated at energies higher than $\sqrt{s} = 14$ TeV.

3.2.1 Parameter regions in the Low Scale MCHM

The following are the parameter ranges considered in the Low Scale MCHM_5:

$$|M_1| \in [0.8, 3.0] \text{ TeV}, \qquad M_4 \in [1.2, 3.0] \text{ TeV},$$
$$f \in [0.8, 2.0] \text{ TeV}, \qquad y_L \in [0.5, 3.0].$$

In the case of the Low Scale MCHM_{14}, we used:

$$|M_1| \in [0.8, 3.0] \text{ TeV}, \quad |M_4| \in [1.2, 3.0] \text{ TeV}, \quad M_9 \in [1.3, 4.0] \text{ TeV},$$
$$f \in [0.8, 2.0] \text{ TeV}, \quad y_L \in [0.5, 3.0].$$

In order to remain in a perturbative regime, justifying the present tree-level analysis, we will take $y_L < 3$. For the same reason, we also check that y_R, as determined by the top mass, is below 4. The distribution of points within those ranges was not uniform, due to computing constraints, but we strive to cover most of the parameter space.

3.2.2 Parameter regions in the High Scale MCHM

The region of the parameter space covered by the High Scale MCHM is defined by the possible reach of a high energy pp collider operating with at least $\sqrt{s} = 100$ TeV and 20 ab^{-1} integrated luminosity [72].

For the High Scale MCHM$_5$ we consider:

$$\begin{aligned} |M_1| &\in [2, 30] \text{ TeV}, & M_4 &\in [2, 30] \text{ TeV}, \\ f &\in [0.8, 8.0] \text{ TeV}, & y_L &\in [0.5, 3.0], \end{aligned}$$

and for the High Scale MCHM$_{14}$ we use:

$$\begin{aligned} |M_1| &\in [2, 30] \text{ TeV}, & |M_4| &\in [2, 30] \text{ TeV}, & M_9 &\in [2, 30] \text{ TeV}, \\ f &\in [0.8, 8.0] \text{ TeV}, & y_L &\in [0.5, 3.0]. \end{aligned}$$

It is worth noticing that these ranges must be linked continuously to the ones defined for the LS-MCHM, such that some points in the HS-MCHM are already tackled by the HL-LHC. We will see in the next two chapters that this is the case for some LS-MCHM showcase points that are still of interest in the HS-MCHM.

3.3 Simple Physical Observables

The diagonalization of the $Q = 2/3$ mass matrix leads to several physical quantities of interest. There is a rich spectrum of vector-like states. Up to small EW symmetry breaking effects, these vector-like masses are approximately given by:

- MCHM$_5$:

$$M_4 \ , \qquad \sqrt{M_4^2 + y_L^2 f^2} \ , \qquad \sqrt{M_1^2 + y_R^2 f^2} \ ,$$

- MCHM$_{14}$:

$$M_4 \ , \qquad \sqrt{M_4^2 + y_L^2 f^2} \ , \qquad \sqrt{M_1^2 + y_R^2 f^2} \ , \qquad M_9 \quad (\text{degeneracy} = 3) \ .$$

We will use the mass of the lightest state, which we call $T^{(1)}$, as a proxy for the scale of the new physics. These resonances present important lower bounds obtained by experimental direct searches. At the time in which the analyses presented in this

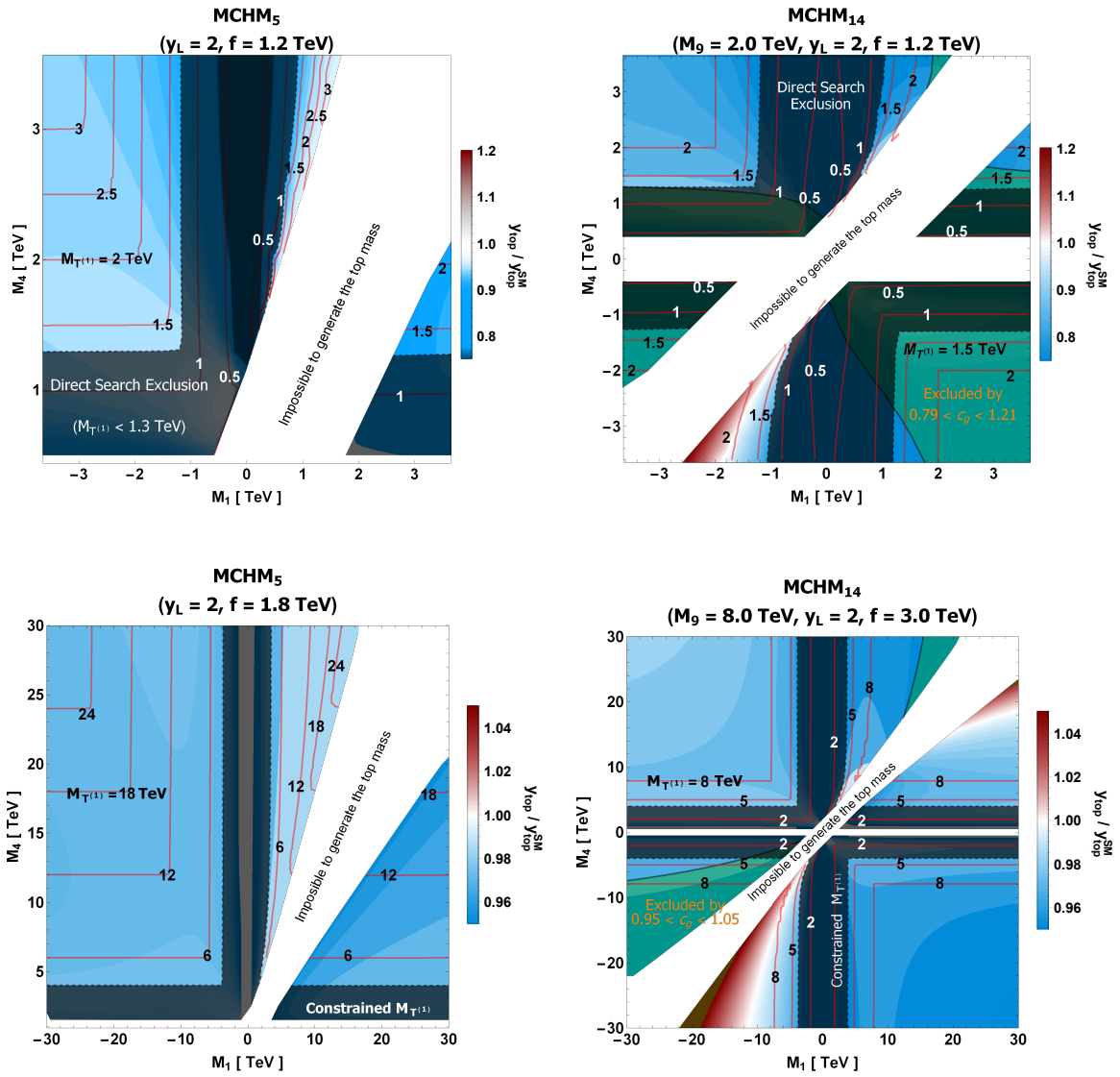

Figure 3.1: Normalized value of the Yukawa coupling of the top, $y_{\text{top}}/y_{\text{top}}^{\text{SM}}$ in the M_1-M_4 plane for the MCHM$_5$ (left) and MCHM$_{14}$ (right). Top figures focus on $\mathcal{O}(1)$ TeV scale, bottom ones expand it to higher mass scales. Also shown are contours of constant mass of the lightest top partner, $M_{T^{(1)}}$. Overlayed regions indicate constraints: the dark one is given by direct exclusion of top partners in the top plots [34, 35], and by expected constraints in the HL-LHC in the bottom ones ($M_{T^{(1)}} < 4$ TeV) [41]; the green region is constrained by c_g measurements [68] in the top plot and by the c_g expected constraints [41] in the bottom one. In the white region, the top mass cannot be reached without violating perturbativity.

Thesis were performed, we considered the results in [35] (from the ATLAS collaboration) and in [34] (from the CMS collaboration). These searches consider vector-like top partner resonances decaying exclusively in the bW, tZ and th channels. These bounds depend mildly on the decay branching fractions and were around 1.3 TeV. As we will in Chapters 4 and 5, some points in these models present additional three-body decay channels. An extensive study of those channels in the MCHM$_5$ and their effect on the bounds reported by the experimental analyses will be shown in Chapters 6 and 7, respectively. However, in this chapter and the following two, we will ignore these possible modifications.

We also consider the deviations from the SM of the top quark decay width. However, the previous direct bounds imply that such deviations are well within the experimental uncertainties, and therefore do not impose additional bounds on the models.

The top Yukawa coupling is of central importance in our study as it is present both in the $t\bar{t}h$ and $t\bar{t}hh$ processes. We will explore here the quantity $y_{\rm top}/y_{\rm top}^{\rm SM}$, the top Yukawa coupling normalized to its SM value, such that it indicates a suppression of the SM top Yukawa if it is less than one and an enhancement when it is bigger than one. In order to have a first picture of its behaviour in the parameter space of Composite Higgs models, we performed a grid scan in the M_1 - M_4 plane for fixed values of y_L and f in the MCHM$_5$ and fixed values of y_L, f and M_9 in the MCHM$_{14}$. We followed the strategy described in Section 3.1, that is, numerically solving Eq. (3.11) for y_R. The results of the scans are shown in Figure 3.1 for the MCHM$_5$ (at the left) and for the MCHM$_{14}$ (at the right). At the top, we considered $f = 1200$ GeV, $y_L = 2$, $M_9 = 2$ TeV and mass parameters ranges $|M_{1,4}| \leq 3.5$ TeV. These plots are relevant for the LS-MCHM as defined in Section 3.2.1. At the bottom of Figure 3.1, we considered a larger region in the M_1 - M_4 plane ($|M_{1,4}| \leq 30$ TeV) to account for the HS-MCHM as defined in Section 3.2.2. We took $y_L = 2$ and $f = 1.8$ TeV for the MCHM$_5$ and $y_L = 2$, $f = 3$ TeV and $M_9 = 8$ TeV for the MCHM$_{14}$. Blue (red) areas correspond to suppression (enhancement) $y_{\rm top}^{\rm SM}$ and the white areas correspond to regions in the parameter space in which there is no solution for y_R (in the perturbative region), that is, the top mass cannot be reproduced. As we can see, the top Yukawa in the MCHM$_5$ always presents a suppression since it is approximately determined by $F_1(\xi)$ in Eq. (2.34), while in the MCHM$_{14}$, it can be enhanced for some regions as was already shown by [49]. In the LS-MCHM$_{14}$, the enhancement only happens in a small region in the quadrant with $M_{1,4} < 0$, while

the HS-MCHM$_{14}$ plot shows that it can also takes place in a small region in the quadrant with $M_{1,4} > 0$. Additionally, we show red contour lines that represent the mass of the lightest 2/3 charged top partner, $M_{T^{(1)}}$. As mentioned before, direct searches([34, 35]) impose lower bounds for these masses which are represented by the overlayed dark regions. Green regions in the LS-MCHM$_{14}$ display the analogous 2 sigmas boundaries for c_g (the ggh coupling normalized to its SM value), at the time of this study [68]. For the HS-MCHM$_{14}$, they display the prospect for c_g constraints by the end of the HL-LHC run [41]. In the MCHM$_5$, c_g only depends on f and it is not constrained in the parameter space regions displayed in the plots.

3.4 Event Generation

Both MCHM's were implemented in FeynRules (v2.3) [73]. The generated UFO files can be interfaced with MadGraph (MG5) [74]. In the results showed in the following sections and in Chapters 4 and 5, the MG5 version used was v2.6.2. We developed a Python script that, given a parameter space point, feeds the numerical input from the diagonalization into the "param_card.dat" file for further MG5 processing. Finally, we simulate the processes $t\bar{t}h$ and $t\bar{t}hh$ in MG5.

It is worth noticing, that the fully developed framework just described can be directly connected to detector fast simulation softwares as DELPHES or to detailed full simulations as the ones of CMS or ATLAS. For instance, in Chapters 7 and 8 we will use DELPHES to perform a fast simulation in the context of the study of 3-body decays in Composite Higgs Models. Also, in Section 4.4.3, we will show a study from the CMS Collaboration in which some of the points suggested in this work were fully simulated by using the configurations of the future CMS-Phase 2 detector that will be operating at the HL-LHC.

3.5 Description of the processes of interest

3.5.1 The $t\bar{t}h$ process

The Feynman diagrams of the $t\bar{t}h$ process at tree level in the MCHM scenarios are identical to the ones in the SM. They involve top/anti-top pair production with one Higgs radiating from the top lines. Diagrams in which a Higgs radiates from initial $q\bar{q}$ lines can be neglected as either the Yukawa couplings are small or the

heavier flavours are PDF suppressed. Therefore, the $t\bar{t}h$ cross section, $\sigma_{\text{MCHM}}(t\bar{t}h)$, is directly related to the corresponding SM cross section, $\sigma_{\text{SM}}(t\bar{t}h)$, via:

$$\sigma_{\text{MCHM}}(t\bar{t}h) \;=\; \left(\frac{y_t}{y_t^{\text{SM}}}\right)^2 \sigma_{\text{SM}}(t\bar{t}h)\ . \tag{3.15}$$

All modifications due to Higgs compositeness or mixing with vector-like fermions, are contained in the top Yukawa coupling. Thus, we only expect a modification in the total cross section with respect to the SM but no modification on kinematical distributions.

3.5.2 The $t\bar{t}hh$ Process

In the case of the $t\bar{t}hh$ process, the additional Higgs boson allows for a richer dependence on the new physics than in $t\bar{t}h$. We can identify two qualitatively different contributions:

1. Resonant processes, that involve the production of vector-like charge 2/3 resonances that decay into th. They can be present in two ways. Either they appear in pairs, from QCD pair production, or singly, as an intermediate state in a fermion line that involves flavor-changing Yukawa interactions. However, this process is largely dominated by QCD pair production.

2. Non-resonant processes, in which only the diagrams without intermediate top partners are included (see Figure 3.2).

Depending on the resonance mass, their pair production in the resonant processes can lead to important enhancements in cross section with respect to the SM. On the other hand, the non-resonant processes carries qualitatively different information. For that reason, we decide to define a "non-resonant cross section (NR-$t\bar{t}hh$)" from the subset of non-resonant processes Feynman diagrams. Similarly, we can define a resonant cross section considering only diagrams involving resonances. We find that the total $t\bar{t}hh$ cross section is well approximated by the sum of these resonant and non-resonant cross sections.

In Figure 3.3, we show the distributions of the invariant mass of th for a point in the parameter space of the MCHM$_5$. We show the distributions for the full $t\bar{t}hh$(in red), for NR-$t\bar{t}hh$ (in black) and for the SM (in dashed blue). We present these distributions for two values of CM energy: 14 TeV and 100 TeV. There we can see that

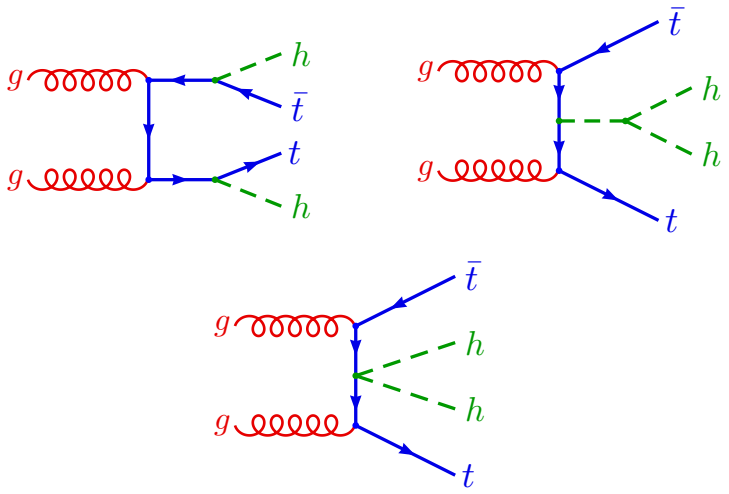

Figure 3.2: Representative diagrams for the non-resonant $t\bar{t}hh$ process, illustrating the three distinct physical subprocesses: the Yukawa vertex, the Higgs trilinear self-coupling and the "double Higgs" Yukawa vertex arising in composite Higgs scenarios.

the non-resonant contribution follows the SM cross section but with a suppression, while the resonant part increases significantly the full $t\bar{t}hh$ cross section, being more important for larger CM energies. These different kinematical behaviours between the non-resonant and resonant subprocesses suggest that they can be separated experimentally, in principle.

3.5.3 The Non-Resonant $t\bar{t}hh$ Process

The Feynman diagrams in the non-resonant $t\bar{t}hh$ can be grouped into three categories, depending on the kind of vertices they contain. These are shown in Figure 3.2 and are:

1. Diagrams containing only the tth vertex.

2. Diagrams containing both the tth vertex and the trilinear Higgs self-interaction: $\lambda = \left[(1-2\xi)/\sqrt{1-\xi}\right] \lambda_{\text{SM}}$.

3. Diagrams containing the $tthh$ vertex ("double Higgs" Yukawa vertex).

The first two categories involve the same diagrams as in the SM. On the other hand, the third category of diagrams are not present in the SM as the $tthh$ vertex is a consequence of the non-linearity of the Higgs sector in Composite models [76]. Thus, it would be extremely interesting if evidence of this coupling is found. In

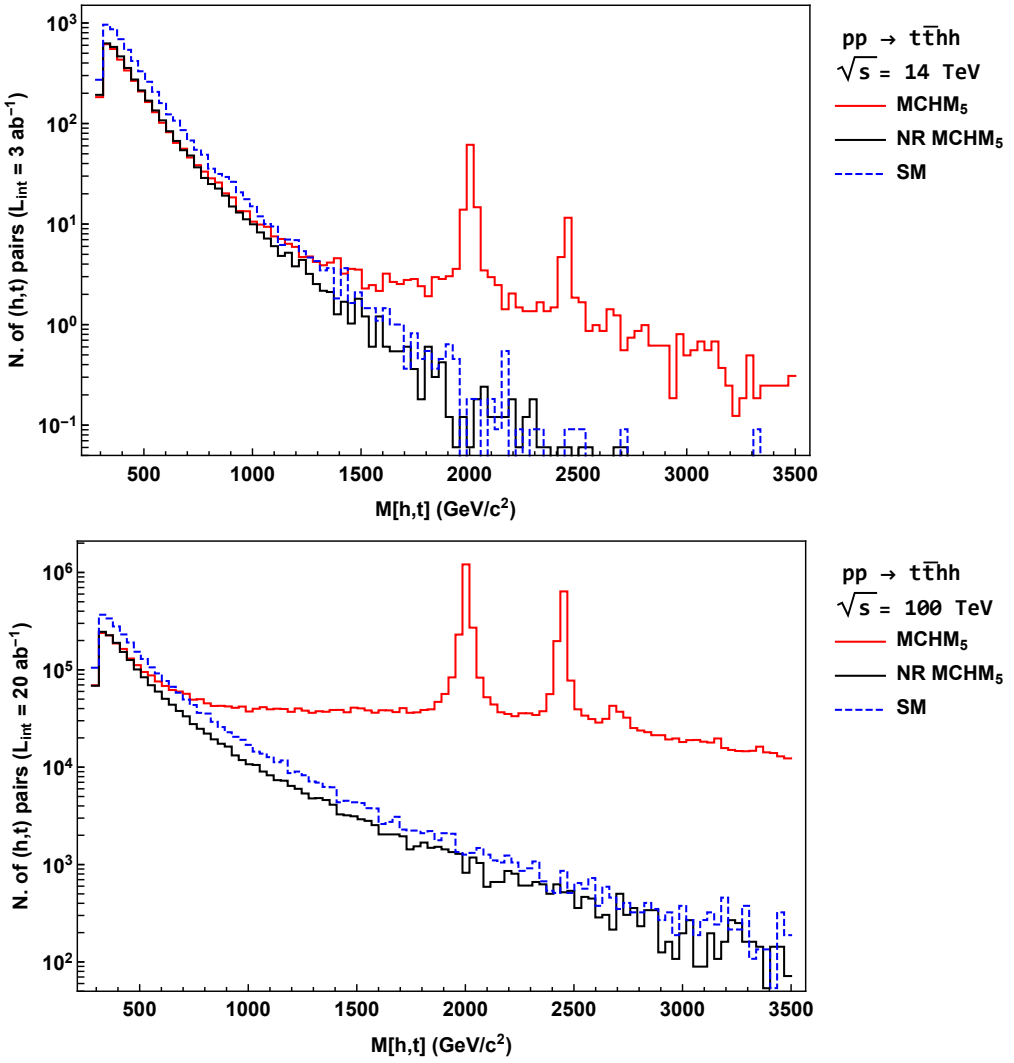

Figure 3.3: Distribution of the invariant mass of the top quark and a Higgs boson in the MCHM$_5$ ($M_1 = -2.5$ TeV, $M_4 = 2.0$ TeV, $f = 1.0$ TeV, $y_L = 1.5$). The red continuous line shows the distribution of the full $t\bar{t}hh$ process in the MCHM$_5$, while the NR-$t\bar{t}hh$ cross section is shown in black. For comparison, we also show in dashed blue the SM $t\bar{t}hh$ distribution. The upper (lower) plot corresponds to 14 TeV (100 TeV) CM energy. Histograms generated with MadAnalysis 5 [75].

Section 4.3, we will present a study to estimate the relative importance of each of these subprocess categories.

3.6 Analysis of the d_μ-symbol Operators

So far we have assumed that the terms involving d_μ symbols operators in Eqs. (2.7) and (2.17) are irrelevant to the present study. Here, we justify this assumption. To that end, we survey the possible effects that these operators could have on the processes of our interest, namely, $t\bar{t}h$ and $t\bar{t}hh$. The complete expansion of these Lagrangian terms in the gauge basis are shown in Appendix C. Although we are only analyzing the MCHM$_5$, the conclusions we reach are valid also for the MCHM$_{14}$.

3.6.1 Effect on the $t\bar{t}h$ Process

Let us consider Eq. (C.3). We can notice that these terms are antisymmetric in Ψ_1 and Ψ_4. Therefore, when they contain the same mass eigenstate fermions, they cancel out with their respective complex conjugate term. That is, d_μ symbol operators does not modify the tth vertex. Since the only non-QCD vertex in the $t\bar{t}h$ process at LO is the tth vertex, this process is not affected in any way by the d_μ symbol operators. The same reasoning can be applied to the MCHM$_{14}$ scenario (see Eq. (C.4)).

3.6.2 Effect on the $t\bar{t}hh$ Process

Unlike the $t\bar{t}h$ process, the presence of vector-like resonances in the $t\bar{t}hh$ process makes it sensitive to the d_μ symbol operators. The modifications could enter in two ways. First, the d_μ symbol operators contain Yukawa-like terms that couple a Higgs to two fermions with different flavour. These vertices are present in the $t\bar{t}hh$ process. Secondly, the resonance widths can be affected as well, leading to modifications in the final cross section.

To investigate the implications of these modifications in our study, we selected some points in the parameter space of the MCHM$_5$ and performed a scan in the parameters that control the d_μ symbol terms, namely, c_L and c_R. To be under the perturbative regime, we consider the range c_L, $c_R \in [-3, 3]$. We show the outcome of this scan for one point in Fig. 3.4. At the left, we can see that the $t\bar{t}hh$ cross section is modified by a factor that lies in the range $[0.3, 2]$ with respect to the cross section

with $c_L = c_R = 0$. The modification is highly correlated to the branching ratio of the decay channel $T^{(1)} \to th$. This can be seen in the right plot, where we show the modification of this BR w.r.t. the $c_L = c_R = 0$ case. We see that there is a fine tuned region (in red) in which the BR is be suppressed (BR=0) and the $t\bar{t}hh$ cross section takes its minimum values in the corresponding regions. For these regions the resonant component of $t\bar{t}hh$ is suppressed leaving basically only the non-resonant component.

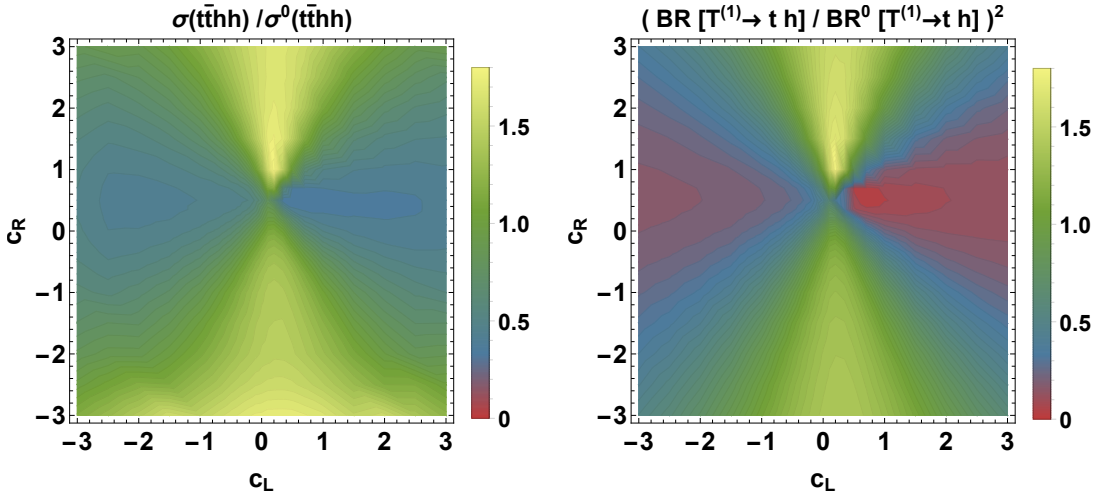

Figure 3.4: Variation with c_L and c_R of the $t\bar{t}hh$ cross section, normalized to the cross section $\sigma^0(c_R = 0, c_L = 0)$, in the MCHM$_5$ ($M_1 = -0.96$ TeV, $M_4 = 1.4$ TeV, $f = 1.2$ TeV, $y_L = 0.88$).

In Figure 3.5 we show the normalized p_t distributions of the most energetic Higgs (at the top) and the most energetic top quark (at the bottom) for the same point used in Figure 3.4 and four combinations of (c_L, c_R). Additionally, we show the corresponding SM distributions for comparison. We can see that different combinations leads to similar distribution shapes, except for the combination $c_L = c_R = 0.5$ in which the distributions tends to the SM shape. This happens because this combination is near the fine tuned point in which BR($T^{(1)} \to th$) tends to zero (see Fig 3.4). This behaviour occurs for other kinematical distributions and choices of point in the MCHM$_5$ parameter space as well, with the (c_L, c_R) fined tuned point being located at different combinations for each MCHM$_5$ point. Therefore, we notice two qualitatively different situations:

1. Most of the points in the (c_L, c_R) plane have similar distribution shapes differing only in the value of the total cross section by a factor in the range $[0.3, 6]$ for

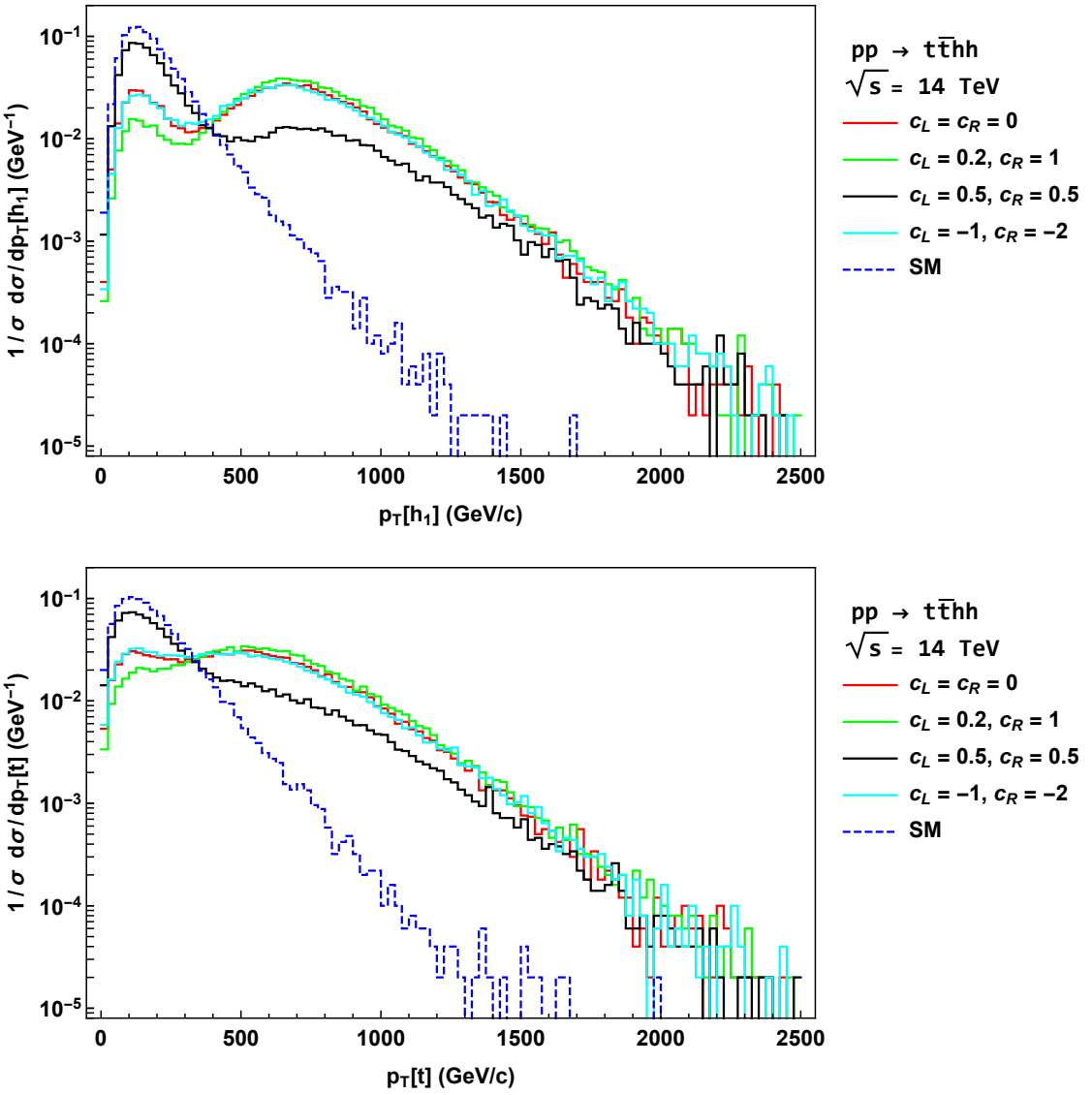

Figure 3.5: p_t distribution of the most energetic Higgs (h_1) and the top particle for 4 combinations of (c_L, c_R) in the MCHM$_5$ ($M_1 = -0.96$ TeV, $M_4 = 1.4$ TeV, $f = 1.2$ TeV, $y_L = 0.88$). The SM is shown for comparison and all curves are normalized to unity area. Histograms generated with MadAnalysis 5 [75].

$\sqrt{s} = 14$ TeV and $[0.3, 8]$ for $\sqrt{s} = 100$ TeV. This is equivalent to a K-factor. Since we are working at LO and we would need to rescale the cross sections, anyway, for them to be compared with experiments, there is no advantage in introducing these additional free parameters.

2. There is a small region around a fine tuned point in the $(c_L,\, c_R)$ space in which the distributions become those of a non-resonant $t\bar{t}hh$ because for these points $\mathrm{BR}(T^{(1)} \to th)$ tends to zero. It would be interesting to explore what happens to other branching ratios in this case but that is out of the scope of the present work.

We have verified that these conclusions are qualitatively the same for the MCHM_{14}. Therefore, we will ignore the d_μ-symbol terms by taking $c_L = c_R = 0$ in the MCHM_5 and $c_4 = c_9 = c_{T9} = 0$ in the MCHM_{14}.

3.7 Strategy to select example points and benchmark points

In next chapters we will present the results of the scan of the parameter space for both LS-MCHM and HS-MCHM and both fermionic representations (**5** and **14**). Since it will be unfeasible to analyze the kinematical distributions of each scanned point, we decided to select two sets of points in each scenario. We labeled these classes of points as "example points" and "benchmark points". Their selection criteria are described below.

The example points are chosen based on striking features or on how accessible they are in the near future (at the start of the HL-LHC), towards the end of the HL-LHC or in the much longer term with a 100 TeV pp collider. The striking features are based on experimental results from the LHC or on prospect studies on the HL/HE-LHC or the FCC-hh project. Therefore, these points could carry a bias and not necessarily represent all possibilities present in the models. However, we will still use them as a way to get an idea of what could happen in the future.

To study the parameter space of the models in a more comprehensive way, we decided to use a *"clustering strategy"* as it was proposed in [77]. It consists in using a test statistic to group the points into "clusters" based on the similarity between

their kinematical distributions. This same test statistic can then be used to select one point in each cluster, that is the most similar to the others in the same cluster. This selected point can act as a typical representative of the cluster and any analysis designed to search for it will be covering all possible phenomena in the cluster. These points are called benchmark points. In the following we describe the main steps of the technique. For further details, we refer the reader to [77].

Given a set of kinematic distributions for a point in the parameter space of the model, we organize them one after the other to form a single distribution. We label this sample as S_a, where a identifies the parameter space point. Next, to measure the similarity between two samples, we use the log-likelihood ratio:

$$TS_{ab} = -2 \sum_{i=1}^{N_{bins}} \left[log(n_{(i,a)}!) + log(n_{(i,b)}!) - 2log\left(\frac{n_{(i,a)} + n_{(i,b)}}{2}! \right) \right], \quad (3.16)$$

where $n_{(i,a)}$ is the number of events contained in the i-th bin of the sample S_a, $n_{(i,b)}$ represents the same for the sample S_b and N_{bins} is the number of bins in the sample. If samples S_a and S_b are identical, TS_{ab} is zero. As their similarity decreases, TS_{ab} also decreases, becoming more negative. Therefore, given two pair of samples, (S_a, S_b) and (S_c, S_d), $TS_{ab} > TS_{cd}$ implies that the pair (S_a, S_b) are more similar between them than the pair (S_c, S_d). Then, given a set of N_{samples}, we use this test statistic to group them into clusters following the steps:

1. We identify each sample as being the unique member of a cluster. Therefore, the initial number of clusters is equal to the number of samples $N_{\text{clusters}} = N_{\text{samples}}$.

2. We compute the similarity between two clusters as the minimum TS_{ab} among all pairs formed by a sample of one cluster and a sample of the other one. That is, $TS^{min} = min_{ab}(\{TS_{ab}\})$, where a runs over all samples in the first cluster and b runs over all samples of the second cluster.

3. We compute TS^{min} between all possible pairs of clusters. The pair of clusters with the highest TS^{min} are the most similar. Therefore, we merge them into one cluster. In this way, the number of clusters, N_{clusters}, decreases by one.

4. We repeat step 3 until the desired N_{clusters} is obtained.

To find the sample with the most representative behaviour in a cluster, we compute $TS_a^{min} = min_b(\{TS_{ab}\})$ for each sample S_a, where S_b represents all other

samples in the cluster but S_a. We choose the representative sample as the one with the highest TS_a^{min}. The corresponding parameter space point is the benchmark point of the cluster. We can do this at each step of the clustering algorithm.

There is no definite way to choose the ideal number of clusters. However, a very small number of clusters implies too heterogeneous behaviours among the distributions inside the clusters, making the benchmark sample to lose its representativity. On the other hand, with a large number of clusters, despite the high homogeneity of their samples, we could end up with too many benchmark points, not reaching the true potential of the clustering algorithm. Therefore, we can run the algorithm until we are left with only two clusters ($N_{cluster} = 2$), recording the complete algorithm history, and examine each step considering the features just described to find the appropriate number of clusters. Similarly, we decide by experimentation which kinematic distributions are used in the algorithm.

Chapter 4

Low Scale MCHM

In Section 3.3, we showed the results of a grid scan in M_1 and M_4 leaving other parameters fixed, to have a general picture of the behaviour of some observables in the parameter space of the models (see Figure 3.1). In order to survey the complete parameter space, we need to scan over all parameters of the model. To that end, we decided to perform a random scan, that is, we arbitrarily choose points in the parameter space of the model without fixing any parameter (apart from y_R which is fixed to reproduce the top mass). In this way, we can cover the parameter space in a more comprehensive and effective way. In this chapter we present the results of the scans performed in the LS-MCHM scenarios.

As it was defined in Section 3.2.1, in the LS-MCHM we restrict ourselves to the following parameter intervals:

$$\begin{aligned} |M_1| &\in [0.8, 3.0] \text{ TeV}, & M_4 &\in [1.2, 3.0] \text{ TeV}, \\ f &\in [0.8, 2.0] \text{ TeV}, & y_L &\in [0.5, 3.0]. \end{aligned}$$

for the LS-MCHM$_5$, and

$$\begin{aligned} |M_1| &\in [0.8, 3.0] \text{ TeV}, & |M_4| &\in [1.2, 3.0] \text{ TeV}, & M_9 &\in [1.3, 4.0] \text{ TeV}, \\ f &\in [0.8, 2.0] \text{ TeV}, & y_L &\in [0.5, 3.0]. \end{aligned}$$

for the LS-MCHM$_{14}$.

Additionally, in order to better survey the parameter space, we define the following regions in the M_1-M_4 plane[1]:

Region I: $M_1,\ M_4 > 0$

[1]We remind the reader that only the sign of M_1 is a free parameter in the MCHM$_5$, while the signs of both masses are free in the MCHM$_{14}$. See section 3.1

Region II: $M_1 < 0$, $M_4 > 0$

in the MCHM$_5$ and MCHM$_{14}$ and

Region III: M_1, $M_4 < 0$

Region IV: $M_1 > 0$, $M_4 < 0$

in the MCHM$_{14}$. We will use these regions definitions also in Chapter 5, where we show the results of the HS-MCHM scan.

Each of these regions is randomly populated with around 200 points. As already mentioned in Section 3.1, points not reproducing the top mass are discarded. Then, for each point, we generate the events for the processes under consideration and their respective kinematic distributions.

In Section 4.1, we show the behaviour of the physical processes in the scanned regions and Sections 4.2 and 4.4 describe the selected example points and benchmark points, respectively.

4.1 The $t\bar{t}h$ and $t\bar{t}hh$ Processes Over the Parameter Space

4.1.1 The $t\bar{t}h$ Process

As shown in Eq. (3.15), the $t\bar{t}h$ cross section is related to the SM one by a simple rescaling of the top Yukawa coupling. The deviations of the top Yukawa coupling from the SM limit have two distinct origins:

- Deviations due to the composite nature of the Higgs boson, which arise from the dependence on the Higgs through trigonometric functions. This depends only on ξ, but is model-dependent and can in principle be used to distinguish the MCHM$_5$ from the MCHM$_{14}$.
- Deviations arising from the mixing of the top quark with the new $Q = 2/3$ resonances. This effect depends on all the microscopic parameters of the model in a complicated manner through the diagonalization of the mass matrix. However, since resonances are much heavier than the top quark, these deviations are typically subdominant compared to the ones arising from Higgs compositeness.

Therefore, the $t\bar{t}h$ cross section in the MCHM scenarios is largely controlled by a single parameter, which we can take to be the scale of global symmetry breaking, f. In Fig. 4.1, we show the dependence of the signal strength $\mu(t\bar{t}h)$ along the various points in the parameter scan of the MCHM scenarios. Although we are displaying the signal strengths for $\sqrt{s} = 14$ TeV, the corresponding $\sqrt{s} = 100$ TeV values are the same, as $\mu(t\bar{t}h)$ does not depend on the CM energy, at tree level. In addition, selected example points are also shown.

The most recent experimental measurements of $\mu(t\bar{t}h)$ at the time of the elaboration of this study were those of CMS [27] and ATLAS [26]. The reported best fits were: $\mu(t\bar{t}h) = 1.14^{+0.31}_{-0.27}$ for the combined 13 TeV result at an integrated luminosity of 35.9 fb^{-1} from CMS and $\mu(t\bar{t}h) = 1.32^{+0.28}_{-0.26}$ for the combined 13 TeV result at an integrated luminosity of up to 79.8 fb^{-1} given by ATLAS. The 1σ and 2σ limits from CMS are shown in Figure 4.1. The ATLAS study have not reported the 2σ limits in their measurements.

The two plots at the top of Figure 4.1 corresponds to the MCHM$_5$. At the left, we can see that, in Region I, the points follow two different behaviours, that correspond to the regions above (with $M_4 > M_1$) and below (with $M_4 < M_1$) the white area in Figure 3.1 in which different average values of the mixing parameters $y_{L,R}$ are needed to reproduce the correct top mass. The lower set of points generally have smaller $M_{T^{(1)}}$ masses (below ~ 1.6 TeV) and $\mu(t\bar{t}h)$ which are in tension with the experimental measurements, although still within the 2σ interval. Points with $M_{T^{(1)}} > 2$ TeV are clustered around the second curve with $\mu(t\bar{t}h)$ larger than 0.8. In contrast, points in Region II tend to follow a unique curve with some dispersion around it and resonance masses homogeneously distributed. As it can be seen in both Regions, all points present a suppression in $\sigma(t\bar{t}h)$ as it is expected in the MCHM$_5$. The example points are shown in both Regions: P_2 and P_5 in Region I, and P_1, P_3 and P_4 in Region II.

The remaining three plots in Figure 4.1 show the results of the scan for the MCHM$_{14}$ case. Three different behaviours are identified concerning the dependence of $\mu t\bar{t}h$ with f. In Region I, the points group into two curves similarly to what happen in the Region I of the MCHM$_5$. However for this case, $\mu(t\bar{t}h)$ can get values as low as 0.2. Therefore, a bigger fraction of points are in tension with the 2σ experimental limits. Regions II and IV are both similar to Region II in

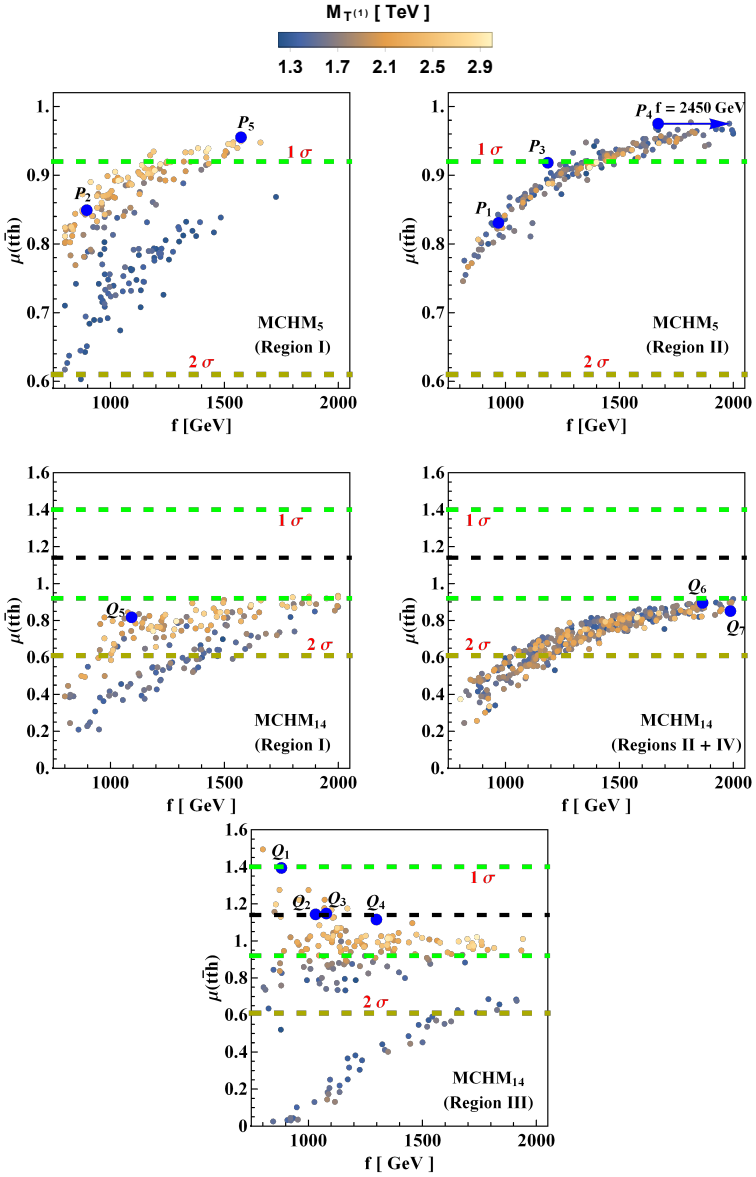

Figure 4.1: Normalized $t\bar{t}h$ cross section as a function of f for 14 TeV CM energies. We also color code the lightest vector-like mass. The upper left (right) plot corresponds to the Region I (II) of the MCHM$_5$. The lower left, central and right plots correspond to the Regions I, II + IV and III of the MCHM$_{14}$, respectively. The blue arrow in the upper right plot indicates that the example point P_4 is outside the horizontal range of the plot with $f = 2450$ GeV. The green (brown) dashed line shows the 1σ (2σ) limits given by the CMS $\mu(t\bar{t}h)$ measurements while the black dashed line represents the central value [27].

the MCHM_5, although with a higher dispersion. Therefore, we joined them in a single plot. The main difference here is also that $\mu(t\bar{t}h)$ can get values as low as 0.2. In Regions I, II ad IV we can notice that only a few points are slightly inside the 1σ interval limit, which happens for high values of f. That is, for the MCHM_{14}, in these Regions, values of $\sigma(t\bar{t}h)$ close to the SM limit are more difficult to obtain than in the MCMH_5 case, for the same degree of Higgs compositeness.

Region III of the MCHM_{14} behaves differently as compared to the other regions as we could already spot in Figure 3.1. In this region, an enhancement of $\sigma(t\bar{t}h)$ with respect to the SM is possible as it is also visible in the bottom plot of Figure 4.1. This is a main distinctive feature of the MCHM_{14} as compared to the MCHM_5 . To further explore this region, we perform an additional scan of 100 points, extending M_9 down to 1.3 TeV. All of these points are shown in Figure 4.1. There are two groups of points. One group follows a curve that gathers a big part of the low $M_{T^{(1)}}$ points. All these points have a suppressed $\sigma(t\bar{t}h)$ with values that can get down to zero for low values of f. On the other hand, the other group of points are gathered around the SM limit $\mu(t\bar{t}h) = 1$ taking values that can be either smaller or bigger than one. These points are more spread the lower the f value is or the higher the compositeness is. The points in this group are, most of them, within the 1σ experimental limits, unlike the other regions in the MCHM_{14} . The selected example points in the four regions of the MCHM_{14} are also shown in the plots. These are: Q_5 in Region I, Q_6 in Region II, Q_7 in Region IV and Q_1, Q_2, Q_3 and Q_4 in Region III.

We conclude that $\mu(t\bar{t}h)$ is a key observable, not only to indicate that there is some BSM effect, but to reject the MCHM_5 while keeping the MCHM_{14} as still possible, if an enhancement w.r.t the SM is confirmed. If a deficit is, instead, observed, both MCHM scenarios are still possible. Their distinction will depend on detailed phenomenology.

4.1.2 The $t\bar{t}hh$ Process

In Figure 4.2 we show how the signal strength $\mu(t\bar{t}hh)$ depends on the mass of the lightest $Q = 2/3$ resonance, $M_{T^{(1)}}$ for both MCHM scenarios and three CM energies: 14 TeV, 100 TeV and 150 TeV. All scanned points (in all regions) are included in the corresponding plots: 400 points for the MCHM_5 and 900 for the MCHM_{14}. As expected, lighter resonances can significantly enhance the $t\bar{t}hh$ cross section due to

QCD pair production. In turn, larger CM energies also increase the value of $\mu(t\bar{t}hh)$, as can be clearly seen for the example points shown in the plots.

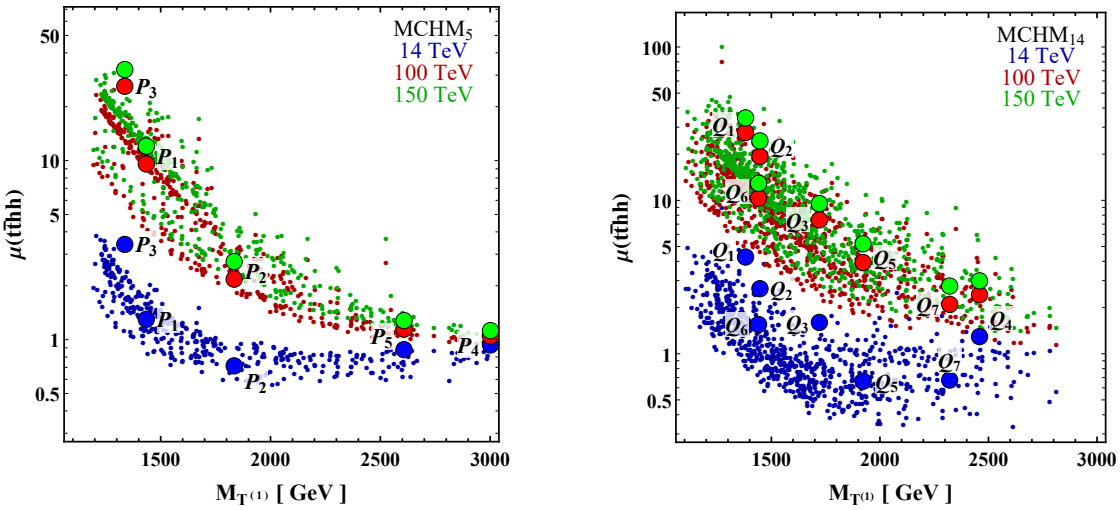

Figure 4.2: Normalized $t\bar{t}hh$ cross section as a function of the lightest $Q = 2/3$ vector-like mass, for 14, 100 and 150 TeV CM energies. The left (right) plots correspond to the MCHM_5 (MCHM_{14}).

Additionally, we show in Figure 4.3 the ratio between the non-resonant contribution and the total $t\bar{t}hh$ cross section as a function of $\text{M}_{T^{(1)}}$. The trends in the MCHM_5 and MCHM_{14} are similar. For heavier resonances, the resonant contributions decreases and the total cross section becomes dominated by the non-resonant contribution. Therefore, even when resonances are rather heavy (let's say around 3 TeV) we can expect deviations from the SM. It is interesting, then, to search for these deviations in addition to the dedicated resonance searches.

Finally, Figure 4.4 shows the NR-$t\bar{t}hh$ cross section (normalized to the SM $t\bar{t}hh$ cross section) as a function of the normalized $t\bar{t}h$ cross section. There is a clear correlation which reflects the fact that both are mainly controlled by the top Yukawa coupling, as explained before.

4.2 Selected Example Points

As explained in Section 3.7, we selected a number of example points to illustrate the physics of the MCHM scenarios. The selection criteria considers the present experimental results including the LHC measurement of the $t\bar{t}h$ production pro-

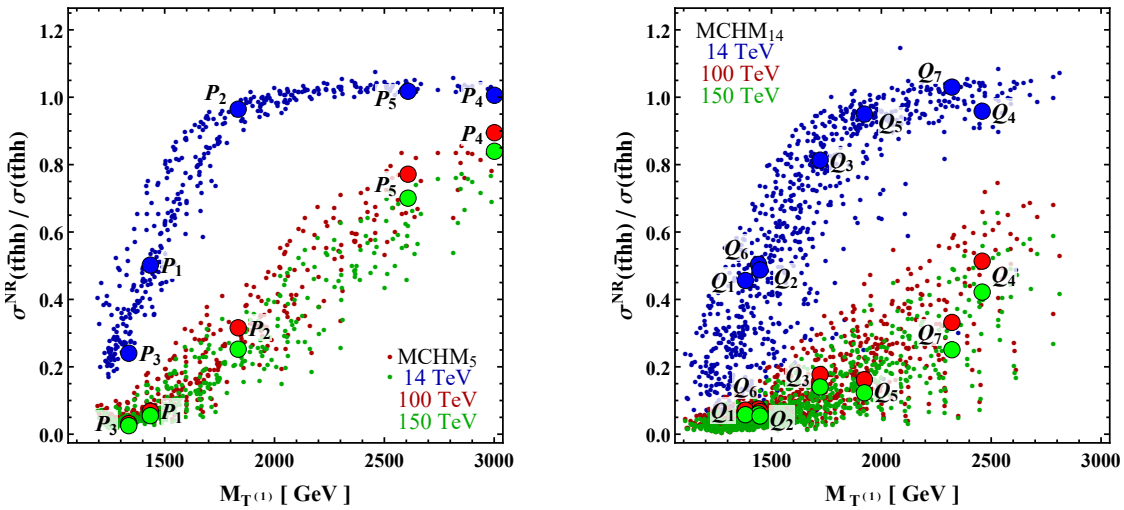

Figure 4.3: Ratio between the non-resonant $t\bar{t}hh$ cross section and the total $t\bar{t}hh$ cross section as a function of the lightest $Q = 2/3$ vector-like mass, for 14, 100 and 150 TeV CM energies. The left (right) plots correspond to the MCHM$_5$ (MCHM$_{14}$).

cess [26, 27], its prospects at the start of the HL-LHC [41], and the exclusion limits on the pair production of heavy vector-like top partners currently obtained by ATLAS and CMS [34, 35, 78]. Additionally, we consider the results of the parameter scan from the plots in Section 4.1.

In Tables 4.1 and 4.2, we list the selected example points for the MCHM$_5$ and MCHM$_{14}$, respectively. These tables include the parameters that characterize each example point, the signal strength of the relevant processes at different energies, the spectra of vector-like fermionic resonances and the BRs of the lightest top partner.

4.2.1 Selected example points and their main features for the LS-MCHM$_5$

In Table 4.1 we show the example points selected for the MCHM$_5$. Two of them (P_2 and P_5) belong to Region I and three (P_1, P_3 and P_4), to Region II.

The point P_1 has a low value of the f scale (strong compositeness) and a $t\bar{t}hh$ process with 50% of non resonant contribution. The $t\bar{t}h$ cross section has a suppression w.r.t the SM value which is close to the estimated 1σ lower limit by the end of Run 3 (with at least 300 fb^{-1}) [79, 80], and w.r.t. the masses of the two lightest heavy top partners and the charge 5/3 resonance. The P_1 scenario will be fully scanned (including its overall resonances spectrum) at the HL-LHC where a 1σ

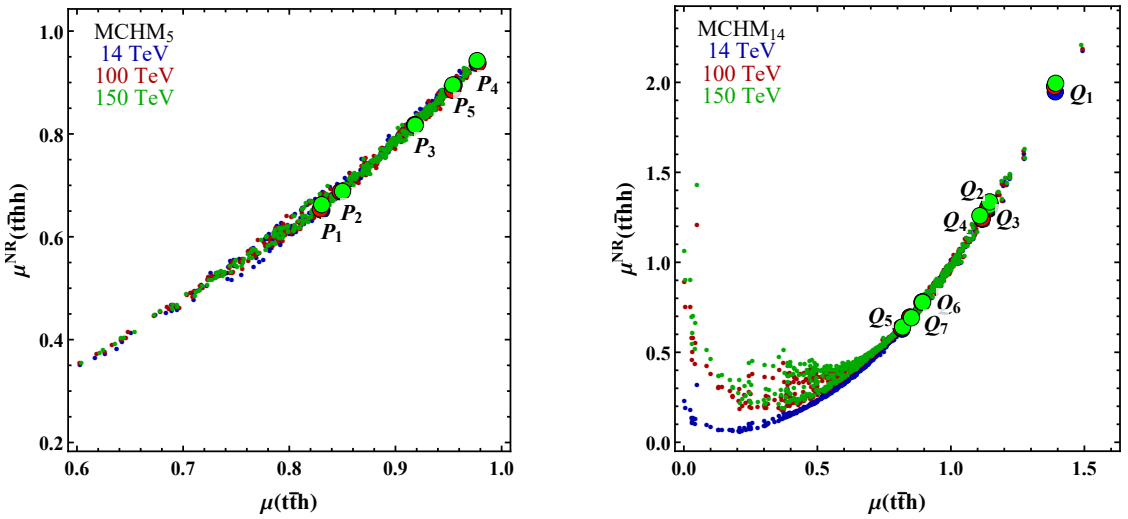

Figure 4.4: Correlation between the normalized $t\bar{t}h$ and non-resonant $t\bar{t}hh$ cross sections, for 14 and 100 TeV CM energies. The left (right) plot corresponds to the MCHM$_5$ (MCHM$_{14}$).

		P$_1$	P$_2$	P$_3$	P$_4$	P$_5$
parameters	M$_1$(GeV)	-1317	800	-960	-3550	914
	M$_4$(GeV)	1580	2311	1400	3000	2632
	f(GeV)	969	896	1186	2450	1573
	y$_L$	1.66	1.80	0.88	1.00	2.36
	y$_R$	0.62	1.95	0.87	0.85	2.41
$\mu(t\bar{t}h)$ (All Energies)		0.83	0.85	0.92	0.98	0.96
$\mu(t\bar{t}hh)$ (14 TeV)		1.30	0.71	3.40	0.93	0.88
$\mu(t\bar{t}hh)$ (100 TeV)		9.58	2.18	26.01	1.05	1.15
NR-$t\bar{t}hh/t\bar{t}hh$ (14 TeV)		0.50	0.97	0.24	1.01	1.02
NR-$t\bar{t}hh/t\bar{t}hh$ (100 TeV)		0.07	0.32	0.03	0.90	0.77
$M_{T^{(1)}}$ (TeV)		1.44	1.83	1.34	3.00	2.61
$M_{T^{(2)}}$ (TeV)		1.59	2.37	1.45	3.82	3.91
$M_{T^{(3)}}$ (TeV)		2.25	2.83	1.76	3.99	4.56
$M_{B^{(1)}}$ (TeV)		2.25	2.82	1.75	3.87	4.56
$M_{X_{5/3}}$ (TeV)		1.58	2.31	1.40	3.06	2.63
$\Gamma_{T^{(1)}}$ (GeV)		24.7	95.2	4.1	26.7	16.5
BR(T$^{(1)}$ $\to$th)		0.33	0.30	0.61	0.31	0.33
BR(T$^{(1)}$ $\to$W$^+$b)		0.46	0.46	0.06	0	0.16
BR(T$^{(1)}$ $\to$tZ)		0.22	0.20	0.26	0.30	0.26
BR(T$^{(1)}$ $\to$W$^+$W$^-$t)		0	0.04	0.07	0.39	0.25

Table 4.1: Properties of selected example points in the LS-MCHM$_5$. Red and blue column headings indicate points belonging to Region I and II respectively.

uncertainty of 4.3% is expected on $\mu(t\bar{t}h)$ [41]. On the other hand, the slight increase of the $t\bar{t}hh$ production cross section w.r.t the SM at 14 TeV, might not be reachable at high luminosity. Furthermore, it is possible that it will only be visible at higher CM energies when the discrepancy with the SM value further increases. This makes this eventual scenario interesting to look at, even if possibly quickly disregarded at a certain stage of the HL-LHC run.

Unlike P_1, the point P_2 shows a high NR-$t\bar{t}hh$ and a clear deficit in $\mu(t\bar{t}hh)$; both effects are also visible for points P_4 and P_5. However, P_2, as it happens with P_1, presents a deficit in $\mu(t\bar{t}h)$ because both have a rather low f value (strong compositeness). Points P_4 and P_5, instead, have a high f value which translates into a $\mu(t\bar{t}h)$ very close to 1.

Point P_3 has still a rather low f value with, as striking features, the strong increase in $\mu(t\bar{t}hh)$ at the expense of the low NR-$t\bar{t}hh$ contribution (see dominant decay of the lightest resonance into th) and $\mu(t\bar{t}h)$ getting close to 1. All the expected resonances, in this case, have relatively low mass well reachable at the HL-LHC (and even may be before, i.e. by the end of the forthcoming Run 3). The HL-LHC increased luminosity will allow to measure the th decay branching ratio, predicted to be dominant with respect to tZ. Besides, the full HL-LHC dataset could indicate a possible excess in $\mu(t\bar{t}hh)$.

Points P_4 and P_5 share similar features. The heavy top partners make the NR-$t\bar{t}hh$ contribution to be dominant even at high CM energies. The large values of f also keep the $\mu(t\bar{t}h)$ very close to one (especially the point P_4). Although, the $\mu(t\bar{t}hh)$ also present values very close to the SM one, a first indication of their deficit could already be evidenced at the HL-LHC. Therefore, although the points P_4 and P_5 look more like scenarios for the higher CM energy hadron colliders, a first breakthrough on such scenarios, especially for P_5 could be achieved by the end of the HL-LHC. Finally, note that the lightest resonance in both cases has a low branching ratio into Wb (especially P_4), while a more important 3-body decay. This enhanced W^+W^-t channel arises for points in which $T^{(1)}$ has a larger fourplet contribution and then is almost degenerate with $X_{5/3}$ (both are controlled by M_4). We will discuss this effect in Chapter 6.

It is worth noting that, as expected in these models (see sections 2.2 and 3.3), in all cases, there is a mass degeneracy between several resonances, with a mass splitting from a few tens of GeV down to a few hundreds of MeV, due to EWSB effects.

The different scenarios described as example points for the MCHM$_5$ present interesting features that allow distinguishing them from each other. They represent a variety of cases, covering different locations of the MCHM$_5$ parameter space. Thus, they are interesting for exploring this Minimal Composite Higgs Model.

4.2.2 Selected example points and their main features for the LS-MCHM$_{14}$

As already mentioned, the MCHM$_{14}$ parameter space was split into 4 Regions in the $M_1 - M_4$ plane (See Figure 3.1 and the definitions at the beginning of the present chapter). In the Low Scale MCHM$_{14}$, we saw that Region III is special as it is the only one in which there is a enhancement in $\mu(t\bar{t}h)$. We extended the ranges of M_9 in this region (1.3 TeV up to 4 TeV), while in the remaining regions M_9 takes 2 TeV as its lowest value. In Table 4.2, we show the selected example points in the LS-MCHM$_{14}$. We chose 4 points belonging to Region III (Q_1, Q_2, Q_3 and Q_4) and one point for each of the remaining regions (Q_5 in Region I, Q_6 in Region II and Q_7 in Region IV).

		Q_1	Q_2	Q_3	Q_4	Q_5	Q_6	Q_7
parameters	M_1(GeV)	-1173	-1054	-1084	-1579	976	-1387	2998
	M_4(GeV)	-1823	-1826	-1767	-2512	1991	1443	-2318
	M_9(GeV)	1382	1448	2036	2714	3096	3115	2875
	f(GeV)	882	1032	1078	1298	1093	1865	1987
	y_L	1.98	1.93	2.95	2.71	1.49	1.52	0.94
	y_R	3.90	2.78	2.67	2.46	3.04	0.34	0.54
$\mu(t\bar{t}h)$ (All Energies)		1.40	1.14	1.15	1.11	0.82	0.89	0.85
$\mu(t\bar{t}hh)$ (14 TeV)		4.27	2.66	1.60	1.29	0.66	1.55	0.67
$\mu(t\bar{t}hh)$ (100 TeV)		27.70	19.32	7.46	2.42	3.93	10.36	2.09
NR-$t\bar{t}hh/t\bar{t}hh$ (14 TeV)		0.46	0.49	0.81	0.96	0.95	0.50	1.03
NR-$t\bar{t}hh/t\bar{t}hh$ (100 TeV)		0.07	0.07	0.18	0.51	0.16	0.07	0.33
$M_{T^{(1)}}$ (TeV)		1.38	1.45	1.72	2.46	1.92	1.44	2.32
$M_{T^{(2)}}$ (TeV)		1.38	1.45	2.01	2.70	2.47	1.52	2.82
$M_{T^{(3)}}$ (TeV)		1.41	1.46	2.04	2.71	3.09	2.96	2.87
$M_{B^{(1)}}$ (TeV)		1.38	1.45	2.02	2.70	2.53	2.98	2.84
$M_{X^{(1)}_{5/3}}$ (TeV)		1.38	1.45	1.77	2.51	1.99	1.44	2.32
$\Gamma_{T^{(1)}}$ (GeV)		12.2	7.8	55.2	121.1	54.9	9.5	24.2
BR($T^{(1)} \to$th)		0.39	0.28	0.44	0.38	0.50	0.42	0.37
BR($T^{(1)} \to W^+$b)		0.35	0.48	0.14	0.13	0.12	0.15	0.02
BR($T^{(1)} \to$tZ)		0.16	0.13	0.30	0.27	0.23	0.34	0.35
BR($T^{(1)} \to W^+W^-$t)		0.09	0.09	0.12	0.22	0.14	0.08	0.27

Table 4.2: Properties of the selected example points in the LS-MCHM$_{14}$. The colors in the column headings indicate the region, with red and orange meaning, respectively, Regions I and III (with same sign M_1 and M_4) and blue and cyan, regions II and IV (with opposite sign M_1 and M_4), respectively.

We chose all points in Region III in such a way that they present enhancements in $t\bar{t}h$, as this is one of the main observables we can use to distinguish both MCHM scenarios. We notice that, unlike the MCHM$_5$ example points, relatively high deviations from the SM $t\bar{t}h$ can be found with small values of f. The $\mu(t\bar{t}h)$ value is close to the 1σ experimental limit in [27].

Points Q_1 and Q_2 have small f and M_9 values. The point Q_1 is close to the 1σ CMS experimental limit [27]. Its three lightest 2/3-charged resonances are also near to the ATLAS and CMS limits, which makes it a good example for a high $\mu(t\bar{t}hh)$ enhancement (this can also be seen in some example points in the MCHM_5) where 50% of it comes from the non-resonant contribution at 14 TeV. Apart from the resonant mass degeneracy, this point basically differs from an equivalent MCHM_5 scenario by the enhancement in $\mu(t\bar{t}h)$. The point Q_2 presents qualitatively similar features as the point Q_1, but with slightly heavier resonances and a smaller $\mu(t\bar{t}h)$ enhancement. The enhancement in $\mu(t\bar{t}hh)$ is still high, although it is smaller than for Q_1.

Points Q_3 and Q_4, have both slightly higher f values as compared to the previous two points but much higher M_9 values (around 2 TeV for Q_3 and 2.7 TeV for Q_4). Both points present a $\mu(t\bar{t}h)$ enhancement well within the considered experimental limits and heavier resonances, which translates into a high non-resonant $\mu(t\bar{t}hh)$ contribution. In the case of Q_4 the mass of the lightest resonance is high enough to keep a 50% contribution of the non-resonant part at 100 TeV.

The three remaining example points have different f values (around 1 TeV for Q_5 and around 2 TeV for Q_6 and Q_7). They all have a relatively large M_9 (around 3 TeV). These example points show a suppression in $\sigma(t\bar{t}h)$ and no strong enhancement in $\sigma(t\bar{t}hh)$. The points Q_5 and Q_7 have large NR-$t\bar{t}hh$ contributions due to their heavy lightest resonances. Point Q_6 has only 50% NR-$t\bar{t}hh$ contribution at 14 TeV. All the NR-$t\bar{t}hh$ relative contributions decrease sharply at 100 TeV, as more phase space becomes available for the production of resonances.

The use of these preliminary observables shows that it will be difficult to disentangle between both MCHM scenarios if a suppression in $\sigma(t\bar{t}h)$ is measured and a much more detailed analysis will be required. In some cases, the HL-LHC can give us a first indication, but a potential discovery will likely need higher energy and luminosity.

4.3 NR-$t\bar{t}hh$ contributions in the MCHM$_5$ and the MCHM$_{14}$

In Section 3.5.3 we saw that the Feynman diagrams of the non-resonant $t\bar{t}hh$ contribution can be categorized into three groups of diagrams, namely, the ones shown in Figure 3.2. This categorization was done based on the kinds of vertices they contain. To quantify the importance of these vertices, we simulated the contributions separately disregarding conveniently some of the Feynman diagrams categories for the selected example points. The results are shown in Tables 4.3 and 4.4 for the MCHM$_5$ and the MCHM$_{14}$, respectively.

		P$_1$	P$_2$	P$_3$	P$_4$	P$_5$	Disregarded diagrams
$\sigma_{\not{hh}}/\sigma_{\rm NR}^{t\bar{t}hh}$	(14 TeV)	1.05	1.04	1.03	1.01	1.01	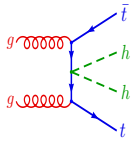
$\sigma_{\not{hh}}/\sigma_{\rm NR}^{t\bar{t}hh}$	(100 TeV)	1.05	1.03	1.03	1.01	1.01	
$\sigma_{\rm Yuk}/\sigma_{\rm NR}^{t\bar{t}hh}$	(14 TeV)	0.86	0.85	0.84	0.82	0.82	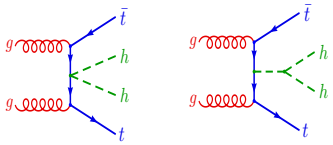
$\sigma_{\rm Yuk}/\sigma_{\rm NR}^{t\bar{t}hh}$	(100 TeV)	0.87	0.87	0.87	0.85	0.85	
$\sigma_{\rm NR}^{t\bar{t}hh}/\sigma_{\rm SM}^{t\bar{t}hh}$	(14 TeV)	0.65	0.69	0.82	0.94	0.90	
$\sigma_{\rm NR}^{t\bar{t}hh}/\sigma_{\rm SM}^{t\bar{t}hh}$	(100 TeV)	0.65	0.69	0.82	0.93	0.89	
$(y_t/y_t^{\rm SM})^4$		0.69	0.72	0.85	0.95	0.91	

Table 4.3: Study of NR-$t\bar{t}hh$ for the MCHM$_5$ points in table 4.1. The cross sections $\sigma_{\not{hh}}$ and $\sigma_{\rm Yuk}$ are obtained by disregarding the classes of diagrams on the last column and $\sigma_{\rm NR}$ is the total NR-$t\bar{t}hh$. The LO SM $t\bar{t}hh$ production is indicated by $\sigma^{\rm SM}$ and $\sigma_{\rm Yuk}^{\rm SM}$ means we disregarded the SM trilinear Higgs coupling. The top Yukawa couplings are indicated by y_t and y_t^{SM} in the MCHM and SM respectively.

From the $\sigma_{\not{hh}}/\sigma_{\rm NR}$ ratios, we can see that the double Higgs Yukawa couplings account for less than 5% of the total non-resonant process in both MCHM$_5$ and MCHM$_{14}$ and it hardly varies with the increase in CM energy. From the $\sigma_{\rm Yuk}/\sigma_{\rm NR}$ ratios, we notice that the trilinear Higgs self-interaction contribution can be around 15% in both MCHM$_5$ and MCHM$_{14}$. For comparison, the contribution of the trilinear Higgs self-interaction in the SM $t\bar{t}hh$ cross section is about 20%, with a very weak dependence on the CM energy. Therefore, the NR-$t\bar{t}hh$ cross section is largely dominated by the top Yukawa vertex as in the SM. Then, we can approximate

	Q_1	Q_2	Q_3	Q_4	Q_5	Q_6	Q_7
$\sigma_{\not{hh}}/\sigma_{\rm NR}^{t\bar{t}hh}$ (14 TeV)	0.95	0.97	0.96	0.98	1.06	1.03	1.05
$\sigma_{\not{hh}}/\sigma_{\rm NR}^{t\bar{t}hh}$ (100 TeV)	0.93	0.96	0.95	0.96	1.05	1.03	1.05
$\sigma_{\rm Yuk}/\sigma_{\rm NR}^{t\bar{t}hh}$ (14 TeV)	0.81	0.82	0.81	0.81	0.86	0.84	0.85
$\sigma_{\rm Yuk}/\sigma_{\rm NR}^{t\bar{t}hh}$ (100 TeV)	0.82	0.83	0.83	0.83	0.87	0.86	0.87
$\sigma_{\rm NR}^{t\bar{t}hh}/\sigma_{\rm SM}^{t\bar{t}hh}$ (14 TeV)	1.94	1.29	1.31	1.25	0.63	0.78	0.69
$\sigma_{\rm NR}^{t\bar{t}hh}/\sigma_{\rm SM}^{t\bar{t}hh}$ (100 TeV)	1.98	1.30	1.32	1.25	0.64	0.78	0.69
$(y_t/y_t^{\rm SM})^4$	1.94	1.30	1.31	1.24	0.67	0.80	0.72

Table 4.4: Study of NR-$t\bar{t}hh$ for the MCHM$_{14}$ points in table 4.2. The cross sections $\sigma_{\not{hh}}$ and $\sigma_{\rm Yuk}$ are obtained by disregarding the classes of diagrams shown on table 4.3 and $\sigma_{\rm NR}$ is the total NR-$t\bar{t}hh$. The LO SM $t\bar{t}hh$ production is indicated by $\sigma^{\rm SM}$ and $\sigma_{\rm Yuk}^{\rm SM}$ means we disregarded the SM trilinear Higgs coupling. The top Yukawa couplings are indicated by y_t and y_t^{SM} in the MCHM and SM respectively.

that the ratio $\sigma_{\rm NR}^{t\bar{t}hh}/\sigma_{\rm SM}^{t\bar{t}hh}$ scales as $(y_t/y_t^{\rm SM})^4$, as we can see in the last three lines of Tables 4.3 and 4.4. This also explains the behaviour of the distributions in Figure 3.3.

Since the trilinear Higgs coupling and the double Yukawa couplings have a low contribution to the non-resonant $t\bar{t}hh$ process, their measurements present challenges. Moreover, they are important to characterize the degree of Higgs compositeness. As we saw, the distributions of the NR-$t\bar{t}hh$ have very similar shapes as those of the SM $t\bar{t}hh$, with the only difference being the total cross section. The top Yukawa is more easily accessed through the $t\bar{t}h$ process. However, combined analyses between the $t\bar{t}h$ and the NR-$t\bar{t}hh$ processes will be needed to extract information about these couplings.

It is worth stressing the importance that the $t\bar{t}hh$ process has in the study of the trilinear Higgs self-coupling. Currently, this is the experimentally least constrained Higgs parameter. Therefore, its measurement is gaining relevance. The experimental "traditional" way to study it is through the hh production via gluon fusion process [81, 82], which, however, is still challenging due to its relatively low cross section and signature efficiency. For that reason, the CMS and ATLAS collaborations are now also searching in the hh production through the Vector Boson Fusion (VBF-hh) [83, 84]. Recently, the $t\bar{t}hh$ process has been pointed out as a complementary channel to study this coupling at the HL-LHC and the FCC-hh [85, 86]. Additionally, the experimental interest in the $t\bar{t}hh$ process is increasing and the first searches have

already been performed at CMS [28].

Phenomenologically, even though the cross sections of the $t\bar{t}hh$ and the VBF-hh are of the same order (fb) at 14 TeV, $t\bar{t}hh$ has some potential advantages. First, it does not suffer of destructive interference between their diagrams unlike in the hh production (see [87]). Also, the additional two top quarks strengthen the signal efficiency as compared to the hh or $hhjj$ signatures. Therefore, this channel is already accessible at the LHC and even more at the HL-LHC. Furthermore, as the $t\bar{t}hh$ cross section increases more sharply with energy, it would become an essential channel at a eventual FCC-hh for high precision and new physics measurements.

4.4 Clusterization of the LS-MCHM parameter space

To study the parameter space more exhaustively, we implemented the clustering strategy described in Section 3.7. In this way we obtain clusters grouping similar points in the parameter space of both the LS-MCHM$_5$ and LS-MCHM$_{14}$ scenarios based on kinematical quantities and select a benchmark point for each of them. In the following, we describe the procedure and results for each scenario.

4.4.1 Clustering of the LS-MCHM$_5$

For the MCHM$_5$, we first consider the 400 scanned points from Section 4.1 and remove all points that were experimentally excluded at 3σ level.[2]. For that, we imposed the following "cuts" [27, 34, 35, 68]:

$$0.33 \leq \mu(t\bar{t}h) \leq 2.07, \tag{4.1}$$

$$M_{T^{(1)}} \geq 1.3 \text{ TeV}, \tag{4.2}$$

$$0.69 \leq c_g \leq 1.33. \tag{4.3}$$

[2]Neither CMS nor ATLAS report the 3σ error directly, so the best we can do here is to assume a Gaussian error and estimate the 3σ threshold simply by multiplying their 1σ intervals by 3, using the ATLAS/CMS combined value when available and the smallest one otherwise.

In the last expression, c_g is the ratio between the value of the ggh coupling in the MCHM over the same value in the SM. Additionally, we checked for the exclusion of points due to the cross sections of the $t\bar{t}Z$ and $t\bar{t}W$ processes. For the $t\bar{t}Z$ case, we considered the CMS measurement of $\sigma(t\bar{t}Z) = 0.95 \pm 0.08$ pb at 1σ level and a integrated luminosity of 77.5 fb^{-1} [88]. The $t\bar{t}Z$ signal strength, $\mu(t\bar{t}Z)$ was obtained as the ratio of that measured cross section over the SM cross section prediction, $\sigma^{SM} = 0.84 \pm 0.10$ pb, which give us $\mu(t\bar{t}Z) = 1.13 \pm 0.16$. For the $t\bar{t}W$, the value of the signal strength $\mu(t\bar{t}W)$ was directly taken from the latest ATLAS collaboration study [89]. The reported value was $\mu(t\bar{t}W) = 1.44 \pm 0.32$ at 1σ level and a integrated luminosity of 36.1 fb^{-1}. We verified that all points in the scan passed these constraints at 3σ level [3].

After the implementation of these constraints, we are left with 348 points that are used as the input for the clustering algorithm. Using MadGraph 5 we generate events for the $t\bar{t}hh$ process for each of these points. We used a fixed luminosity of 3000 fb^{-1}. At parton level, there are only three different particles present: the top, the anti-top and two Higgs bosons (we focused on the most energetic one). Using MadAnalysis we generated histograms for the following kinematic distributions:

- invariant mass of the top/Higgs pair: $M[t, h_1]$,
- transverse momenta: $p_T[t]$ and $p_T[h_1]$,
- angular distances in the transverse plane: $\Delta_R[t, h_1]$ and $\Delta_R[t, \bar{t}]$,
- angular distance to the beam axis: $\theta[t]$ and $\theta[h_1]$,

and used them to build the samples for the clustering algorithm. These samples could contain one or more distributions.

Since the invariant mass distribution, $M[t, h_1]$, shows explicitly the resonant structure, we can think of using it alone to construct the clusters. However, as we checked, with this approach the algorithm focuses too much on the exact position of the resonance peaks instead of more general features like the two peak structure that appears in the Higgs p_T distribution. This would cause us to end with many benchmark points for the regions with lighter and narrower resonances and just a few for the rest of the parameter space. We found that adding the angular distribution $\theta[t]$ makes the clustering to be more evenly distributed. Using other angular

[3] Once again 3σ is roughly estimated as three times the 1σ intervals.

distributions does not change much the results.

The final number of clusters was chosen to be $N_{cluster} = 11$. We found that choosing 10 clusters implies the merge of the two most populated clusters containing all samples with heavy ($M_{T^{(1)}} \gtrsim 1.5$ TeV) and wide resonances. Taking a smaller number of clusters just worsens the situation. On the other hand, a bigger number of clusters only splits the low populated clusters which are already very homogeneous.

The resulting $N_{cluster} = 11$ clusters obtained using the $M[t, h_1]$ and $\theta[t]$ distributions for the LS-MCHM$_5$ are shown in Figures 4.5 and 4.6, where we also included the $p_T[h_1]$ distributions to show their typical behaviour. There we note that all clusters are very homogeneous, that is, the elements of each cluster are very similar. This ensures us that the benchmark points (black curves in the plots) are good representatives of the behaviour of each cluster. As we can see in the plots, this happens even for the $p_T[h_1]$, which were not considered for the clustering procedure. We have checked that this is also the case for other distributions. The only exception is cluster 3, in Figure 4.5, which groups all the points with $M_{T^{(1)}} \gtrsim 1.65$ TeV. This happens because the corresponding curves have a lower count of events in their resonant part as compared to the non resonant region. As this behaviour is common for all points with heavy resonances, they are grouped into the same cluster. A possible workaround would be to perform a separate clustering for these samples to produce more clusters and benchmark points. However, we decided not to follow this possibility because we already covered this region when choosing the example points P_2, P_4 and P_5 shown in Table 4.1. These points were, indeed, grouped in cluster 3 of Figure 4.5 where they are shown as green curves.

The obtained clusters allow us to understand general features of the parameter space. For instance in Figures 4.5 and 4.6 we can see the separation between the points in Region I (red curves) and Region II (blue curves). While samples from Region I were mainly located in clusters 3 to 7, samples from Region II dominate the remaining clusters. We can also notice that resonances in Region I are generally wider than those of Region II. They can be clearly distinguished in clusters 4, 5 and 7 where curves from both regions are present. This distinction can be explained by the way in which the top mass is generated through the Yukawa interactions. They are represented in Figure 2.1 by the first two diagrams in the case of the MCHM$_5$. Both mixings between elementary fields and singlet or fourplet resonances require

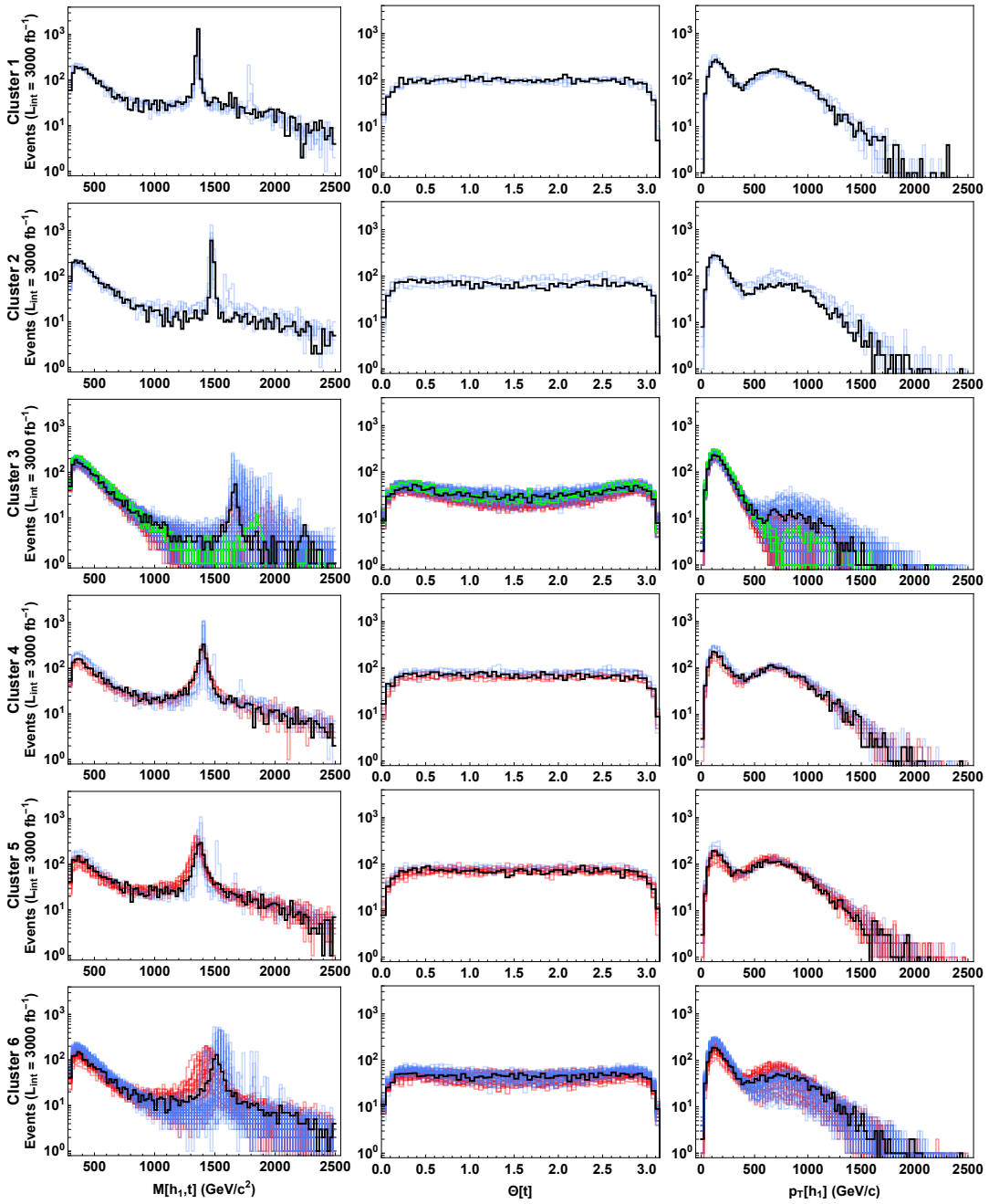

Figure 4.5: Distributions at $\sqrt{s} = 14$ TeV for the invariant mass of the pair composed by top and most energetic Higgs (first column), angular distribution of the top (second column) and transverse momenta of the most energetic Higgs, organized in clusters by similarity (clusters 1 through 6). Red and blue curves indicate respectively points in Regions I and II of the MCHM_5, the benchmark point for each cluster is shown in black and the example points of table 4.1 are shown in green (cluster 3 contains P_2, P_4 and P_5).

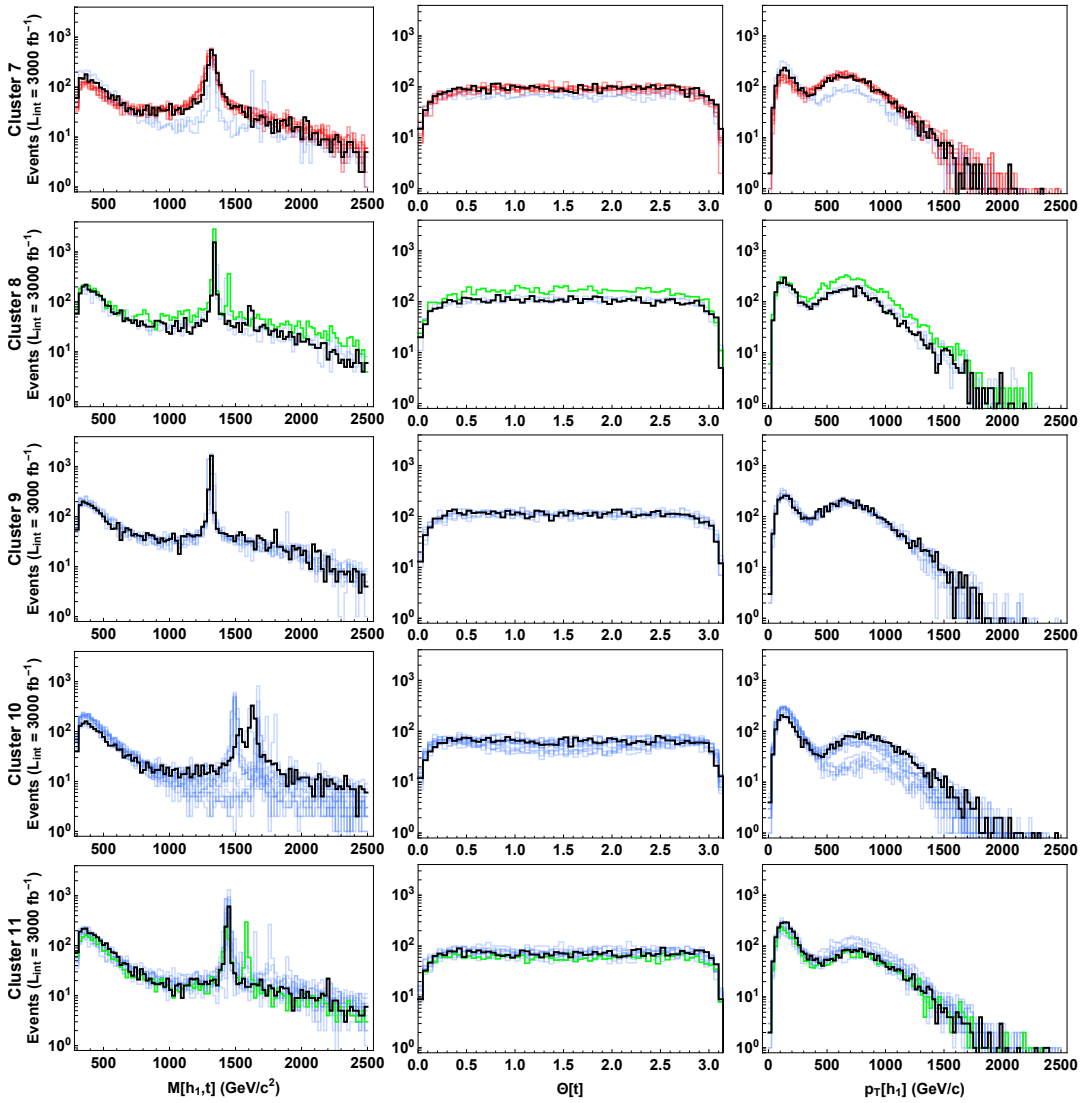

Figure 4.6: Distributions at $\sqrt{s} = 14$ TeV for the invariant mass of the pair composed by top and most energetic Higgs (first column), angular distribution of the top (second column) and transverse momenta of the most energetic Higgs, organized in clusters by similarity (clusters 7 through 11). Red and blue curves indicate respectively points in Regions I and II of the MCHM_5, the benchmark point for each cluster is shown in black and the example points of Table 4.1 are shown in green (P_3 is in cluster 8 and P_1 is in cluster 11).

the insertion of the product $y_L y_R$ and an additional factor M_1 for the singlet and M_4 for the fourplet. These two diagrams must interfere destructively since the pNGB Higgs vacuum misalignment is generated by $SO(5)$ breaking and must vanish in the $SO(5)$ symmetric $M_4 = M_1$ limit. Therefore, we have $m_t \sim y_L y_R |M_4 - M_1|$ as shown in Eq. 2.32. Since in Region I, M_1 and M_4 are of same sign, they cancel each other and in order to reproduce the top mass larger values of $y_{L,R}$ are needed. In turn, that implies larger partial widths, leading to wider resonances.

Another interesting general feature is the presence in many cases of more than one peak in the $M[h_1, t]$ distribution. While cluster 9 represents well the usual simplifying assumption used in top partner searches, namely the presence of only one resonance decaying to the th, tZ or bW channels, many of the other clusters contain a sizeable presence of more complicated peak structures, coming specially from Region II. Cluster 10 is the perfect example of this, as its benchmark point has a double peak structure with the second resonance giving a stronger contribution than the lightest one. Most exclusion limits for top partners are obtained through analyses optimized for the situation in cluster 9, and it would be interesting to see how those limits change if more resonances are considered, specially if they overlap significantly.

In Figure 4.7 we show how the benchmark points are placed in the parameter space, together with the example points of Table 4.1 and the rest of the points in the scan not excluded by constraints. We can see that the benchmark points, complemented by the example ones, are well distributed in the parameter space. We finally list the benchmark points and their main features in Table 4.5, where we can verify many of the features visible in the distribution plots of Figures 4.5 and 4.6. Points in Region I (C_4, C_5, C_6 and C_7) have on average higher couplings y_L and y_R and wider $T^{(1)}$ than those in Region II, although the extreme cases in each region can be similar. The point C_7, which contains a narrow $T^{(1)}$ for Region I standards, is quite similar to C_{10}, in which $T^{(1)}$ is exceptionally wide for Region II.

Another striking feature of Table 4.5 is that for all of the benchmark points (but C_3) there is at least a 10% branching ratio in 3-body decays. Similarly striking and linked to the previous observation, we note that for all points but this same C_3 point, the 2-body decay into bW is very small, namely between 0% and 2.4%. That is relevant as most top partner searches were done under the assumption that the

three 2-body channels (th, tZ and bW) comprise the full width. We will explore the phenomenology of these non-standard branching ratios in Chapter 6.

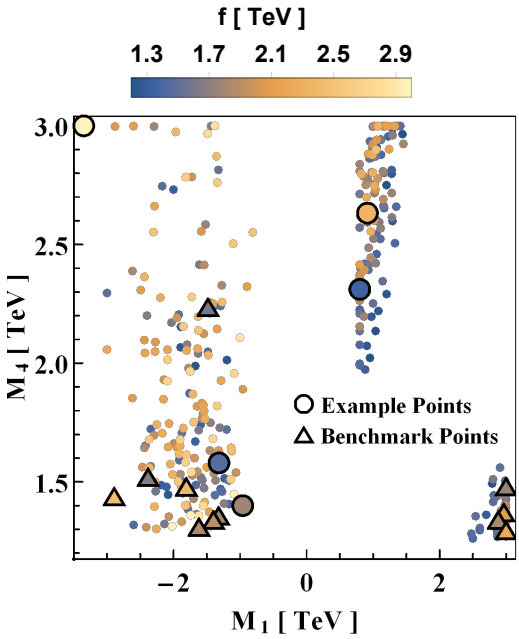

Figure 4.7: Low scale scan of the MCHM$_5$ parameter space, including example points of table 4.1, benchmark points of table 4.5 and the points consistent with constraints in Eqs. 4.1 and 4.2.

		C_1	C_2	C_3	C_4	C_5	C_6	C_7	C_8	C_9	C_{10}	C_{11}
parameters	M_1(GeV)	-1323	-1809	-1483	2965	2882	2999	3000	-1400	-1618	-2384	-2892
	M_4(GeV)	1357	1479	2235	1370	1339	1479	1295	1339	1309	1519	1437
	f(GeV)	1199	1593	1071	1393	1220	1168	1484	1265	1229	1110	1646
	y_L	0.91	2.25	1.38	2.35	1.83	2.33	1.98	1.34	1.22	0.51	1.03
	y_R	0.88	0.58	0.72	3.38	3.57	3.28	3.25	0.66	0.74	2.30	0.85
$\mu(t\bar{t}h)$ (All Energies)		0.90	0.94	0.86	0.83	0.78	0.79	0.84	0.91	0.90	0.81	0.94
$\mu(t\bar{t}hh)$ (14 TeV)		2.14	1.47	0.80	1.51	1.53	1.02	2.00	2.25	2.41	1.39	1.58
$\mu(t\bar{t}hh)$ (100 TeV)		14.58	8.84	3.28	10.28	11.18	7.04	13.42	15.20	16.11	13.68	10.57
NR-$t\bar{t}hh/t\bar{t}hh$ (14 TeV)		0.37	0.59	0.88	0.45	0.40	0.61	0.35	0.36	0.33	0.46	0.55
NR-$t\bar{t}hh/t\bar{t}hh$ (100 TeV)		0.05	0.10	0.22	0.07	0.05	0.09	0.05	0.05	0.05	0.05	0.08
$M_{T^{(1)}}$ (TeV)		1.36	1.48	1.66	1.40	1.38	1.51	1.32	1.34	1.31	1.54	1.44
$M_{T^{(2)}}$ (TeV)		1.63	2.02	2.24	3.55	2.61	3.10	3.22	1.61	1.80	1.63	2.20
$M_{T^{(3)}}$ (TeV)		1.79	3.88	2.68	5.55	5.21	4.85	5.67	2.17	2.02	3.47	3.21
$M_{B^{(1)}}$ (TeV)		1.74	3.87	2.68	3.55	2.60	3.10	3.22	2.16	1.99	1.62	2.22
$M_{X_{5/3}}$ (TeV)		1.36	1.48	2.24	1.37	1.34	1.48	1.29	1.34	1.31	1.52	1.44
$\Gamma_{T^{(1)}}$ (GeV)		8.83	5.49	26.22	51.92	60.01	71.68	44.33	6.44	7.49	43.78	10.63
BR($T^{(1)} \to$th)		0.49	0.45	0.31	0.44	0.43	0.42	0.44	0.47	0.47	0.34	0.45
BR($T^{(1)} \to W^+$b)		0.018	0	0.47	0.004	0.004	0.003	0.006	0.024	0.016	0.005	0.010
BR($T^{(1)} \to$tZ)		0.39	0.41	0.22	0.42	0.43	0.42	0.43	0.40	0.41	0.50	0.41
BR($T^{(1)} \to W^+W^-$t)		0.11	0.13	0	0.13	0.13	0.16	0.12	0.10	0.10	0.14	0.12

Table 4.5: Benchmark points for the MCHM$_5$ at low scale and their main features. Red and blue column headings indicate points belonging to Region I and II respectively.

4.4.2 Clustering of the LS-MCHM$_{14}$

In a similar fashion as done for the LS-MCHM$_5$, we applied the clustering procedure to the points in the parameter space of the MCHM$_{14}$ that satisfy the constraints in Equations. 4.1 and 4.2. The best result, following the requirement of homogeneity while keeping a small number of clusters, was obtained considering the $M[t, h_1]$, $p_T[h_1]$ and $\Delta R[h_1, t]$ distributions in the samples and stopping at 12 clusters. The distribution of the benchmark points in the parameter space is shown in Figure 4.8 and their main properties are listed in Table 4.6. The clusters and the kinematical distributions of the points within them are shown in Figures D.1 and D.6 of Appendix D. Their general features are very similar to the MCHM$_5$, with the points without light resonances decaying to $t\bar{t}hh$ being grouped into less homogeneous clusters (specially clusters 4 and 9). When M_1 and M_4 have opposite signs (Regions II and IV), as anticipated due to the $1 - r_1$ term in Eq. 2.32, there is still a predisposition towards narrower resonances. However, there is now an additional correction that is proportional to ξ and is also dependent on the sign of M_4 (given that $M_9 > 0$), which weakens this tendency. Consequently, this tendency becomes less noticeable, particularly if one considers only the benchmark points.

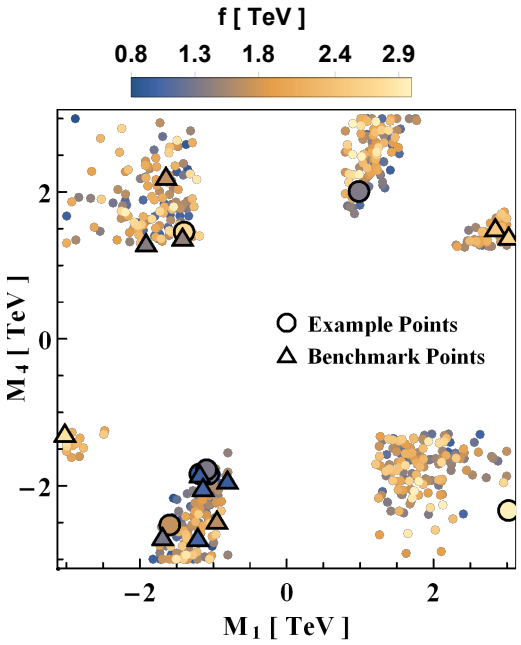

Figure 4.8: Low scale scan of the MCHM$_{14}$ parameter space, including example points of table 4.2, benchmark points of table 4.6 and the points consistent with constraints in Eqs. 4.1 and 4.2.

Figure 4.8 shows that the parameter space is being reasonably well covered

		D_1	D_2	D_3	D_4	D_5	D_6	D_7	D_8	D_9	D_{10}	D_{11}	D_{12}
parameters	M_1(GeV)	-1173	-943	-1899	-1631	2819	-2998	-801	-1130	-1677	2999	-1408	-1202
	M_4(GeV)	-1823	-2447	1297	2196	1501	-1272	-1907	-2005	-2670	1387	1373	-2679
	M_9(GeV)	-1382	2000	3587	3236	2909	3473	1500	1467	2000	3542	2965	1353
	f(GeV)	881	1275	1114	1288	1742	1912	863	931	1071	1807	1155	921
	y_L	1.98	1.33	0.75	2.68	1.92	1.11	1.23	2.93	2.06	1.37	1.04	1.25
	y_R	3.90	1.07	0.71	0.30	2.53	1.86	1.67	1.23	2.65	1.86	0.49	1.99
$\mu(t\bar{t}h)$ (All Energies)		1.39	0.90	0.62	0.71	0.74	0.68	0.93	0.98	1.22	0.74	0.68	1.02
$\mu(t\bar{t}hh)$ (14 TeV)		4.27	0.97	2.82	0.55	0.87	1.81	2.15	1.57	1.70	1.22	1.83	3.32
$\mu(t\bar{t}hh)$ (100 TeV)		27.7	6.32	28.0	3.05	6.77	13.7	19.9	11.2	5.21	9.21	16.0	24.8
NR-$t\bar{t}hh/t\bar{t}hh$ (14 TeV)		0.46	0.82	0.12	0.87	0.61	0.25	0.37	0.61	0.87	0.44	0.23	0.30
NR-$t\bar{t}hh/t\bar{t}hh$ (100 TeV)		0.07	0.13	0.01	0.16	0.08	0.03	0.04	0.09	0.28	0.06	0.03	0.04
$M_{T^{(1)}}$ (TeV)		1.38	1.62	1.31	1.69	1.54	1.31	1.42	1.46	2.00	1.42	1.38	1.35
$M_{T^{(2)}}$ (TeV)		1.38	2.00	1.51	2.20	2.85	2.45	1.50	1.47	2.00	2.79	1.49	1.35
$M_{T^{(3)}}$ (TeV)		1.41	2.00	2.06	3.16	2.91	3.47	1.50	1.47	2.02	3.54	1.81	1.38
$M_{B^{(1)}}$ (TeV)		1.38	2.00	1.53	3.18	2.86	2.45	1.50	1.47	2.00	2.80	1.80	1.35
$M_{X^{(1)}_{5/3}}$ (TeV)		1.38	2.00	1.30	2.20	1.50	1.27	1.50	1.47	2.00	1.39	1.37	1.35
$\Gamma_{T^{(1)}}$ (GeV)		12.2	91.5	19.9	157	83.1	53.1	64.2	79.2	17.7	63.4	17.5	7.45
BR($T^{(1)} \to$th)		0.40	0.25	0.45	0.26	0.41	0.42	0.28	0.11	0.26	0.42	0.46	0.38
BR($T^{(1)} \to W^+$b)		0.35	0.51	0.04	0.48	0.005	0.01	0.45	0.61	0.36	0.009	0.08	0.09
BR($T^{(1)} \to$tZ)		0.16	0.24	0.41	0.22	0.42	0.44	0.24	0.27	0.20	0.43	0.34	0.22
BR($T^{(1)} \to W^+W^-$t)		0.09	0	0.10	0.04	0.16	0.13	0.02	0.02	0.18	0.14	0.08	0.09

Table 4.6: Benchmark points for the low scale $MCHM_{14}$ scan and their main features. Column headings indicate region, with red and orange meaning respectively Regions I and III (with same sign M_1 and M_4) and blue and cyan respectively for regions II and IV (with opposite sign M_1 and M_4).

between the example points from Section 4.2.2 and the benchmark points obtained here. Table 4.6 includes numerous points that exhibit a sizeable 3-body decay in all regions, and many scanned points have overlapping resonances (as observed in the benchmark points of clusters 3, 8 and 11). Both of these factors are significant considerations for top partner searches and constraints.

Lastly, we would like to draw attention to the benchmark points D_1 and D_9, which display a noteworthy enhancement in $\sigma(t\bar{t}h)$. These points highlight the potential for such an occurrence to arise in the $MCHM_{14}$.

4.4.3 Prospected sensitivity of the HL-LHC of some example points

In view of the importance that the $t\bar{t}hh$ process is gaining in the context of the future HL-LHC, the CMS Collaboration performed a prospect study on the sensitivity that can be achieved for the SM $t\bar{t}hh$ cross section measurement in the CMS Phase-2 detector that will be operating in the HL-LHC at $\sqrt{s} = 14$ TeV and 3000 fb^{-1} [29]. Additionally, in the same study, the sensitivity of the MCHM was addressed using some of the benchmark points we suggested in the previous sections.

In the following, we roughly describe their strategy and their main results. For details, we refer the reader to the original paper [29].

The study considers the topology in which the top pair decays semileptonically (one top decaying leptonically and the other hadronically) and each Higgs decays into a bottom pair, accounting for a total of one lepton (either electron or muon), missing energy and eight jets from which at least six of them come from a bottom. The search is done for events with one lepton, a minimum of 4 jets (from which at least 3 of them are b-tagged) and moderate missing transverse energy. Signal and background processes were simulated considering the CMS-Phase 2 conditions. Several discriminating variables were defined and used to train a multi-classifier deep neural network (DNN). The trained DNN was then used to categorize the events according to their likeliness to signal or background processes. Finally, the upper limits on the signal strength are obtained. This strategy was used for both the SM and the MCHM cases. For the MCHM analysis, two benchmark points were used: The point C_2 for the MCHM_5 shown in Table 4.5 and the point D_7 for the MCHM_{14} shown in Table 4.6.

Figure 4.9 shows the distribution of some kinematical variables for the SM-$t\bar{t}hh$ and both MCHM-$t\bar{t}hh$ points. We can clearly see an excess of events in the high energy ranges of the MCHM distributions as compared with the SM, which is due to the high energetic jets produced from the resonance decays. These differences in distributions (specially in the H_T ones) shows a clear discrimination between the non-resonant SM-$t\bar{t}hh$ and the MCHM. We can also notice that the point D_7 presents more events than the point C_2. This happens because, while in the C_2 point the lightest 2/3-charged resonance (with a mass around 1.5 TeV) is much lighter than the other resonances (the next heavier having a mass around 2 TeV) the point D_7 has one 2/3-charged top partner with mass 1.42 TeV and two just slightly heavier top partners with 1.5 TeV.

In Figure 4.10, we show the results on the 95% upper limits of the $t\bar{t}hh$ signal strength for both points C_2 and D_7. The signal strength is defined with respect to the cross section of the $t\bar{t}hh$ process in each MCHM scenario. These results were obtained for three different scenarios of systematic uncertainties: “YR18”, “YR18 conservative” and “Statistics-only”. The ”YR18“ scenario is the most realistic as it considers the systematic uncertainties expected for the CMS-Phase 2 and provided in

the HL-LHC Yellow Report for Higgs Physics [41] [4]. Following this scenario, in the case of the MCHM_{14}^{D7}, the upper limit on the $t\bar{t}hh$ signal strength is $1.08^{+0.43}_{-0.3}$ and in the MCHM_{5}^{C2} is $1.72^{+0.78}_{-0.53}$. The difference is explained by the resonance structure described before, which favours the isolation of $t\bar{t}hh$ events from the MCHM_{14}^{D7} as compared to the MCHM_{5}^{C2}. Therefore, while the MCHM_{14}^{D7} can be reached with reasonable precision within the HL-LHC, the MCHM_{5}^{C2} will need a refinement in the analysis methodology and other measurements to be more conclusive.

[4] For details of the definition of these scenarios, we refer the reader to [29].

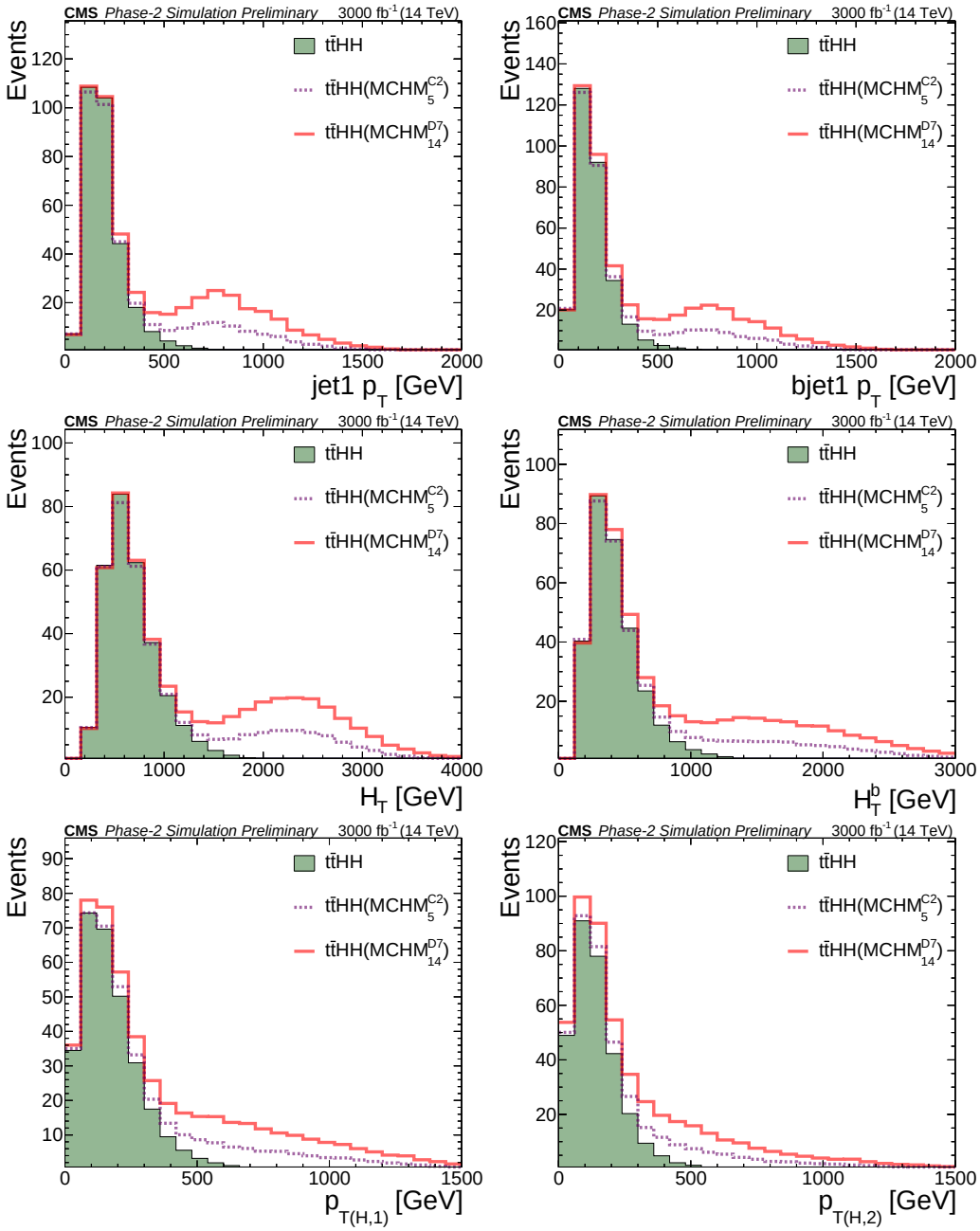

Figure 4.9: Distributions of the variables that discriminate the most between the SM-*tthh* and the MCHM-*tthh*. Plots extracted from [29].

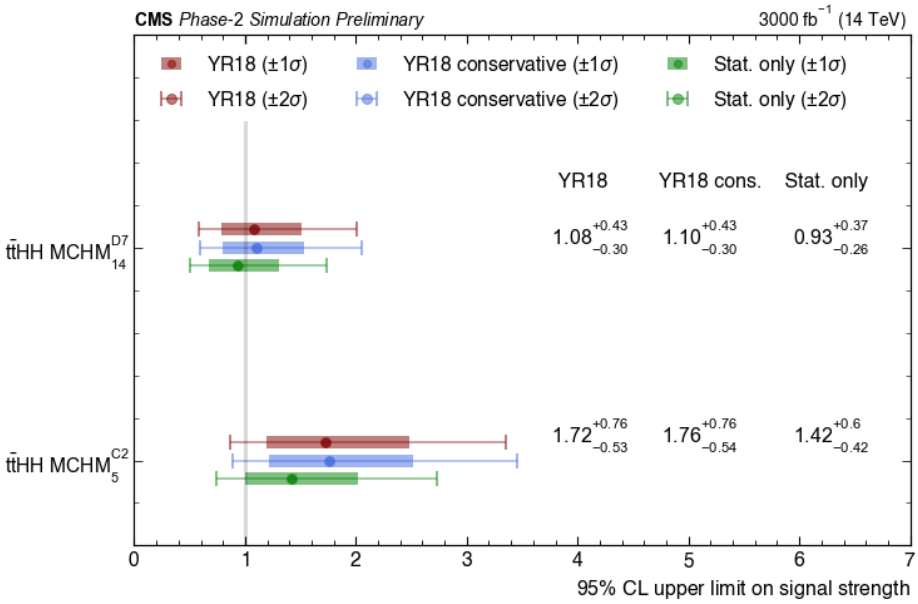

Figure 4.10: The 95% upper limits of the *tthh* signal strength in the MCHM$^{C_2}_5$ and the MCHM$^{D_7}_{14}$ scenarios. The results are shown for different scenarios of systematic uncertainties. Plot extracted from [29].

Chapter 5

High Scale MCHM

We extend our analysis to continue the analysis of the two studied MCHM scenarios, extending the dimensionful parameters to higher scales that can be accessible only in the context of the high CM energy pp colliders in project [15, 17, 22, 23, 24, 71]. A higher CM energy around 100 TeV is requested to confront scenarios with very high mass resonances, with a possible deviation of the $t\bar{t}h$ cross section from the SM value at the percent level (or even less), with the requested precision to study the $t\bar{t}hh$ process (e.g. the various NR components) and to measure the branching ratios of various decays of the produced resonances, even if, for instance, the lightest one is detected at the HL-LHC.

5.1 Scanning Over Parameter Space

We follow the same numerical strategy used for the LS-MCHM (see Section 3.1) with the extended ranges of parameters

$$|M_1| \in [2, 30] \text{ TeV}, \qquad M_4 \in [2, 30] \text{ TeV},$$
$$f \in [0.8, 8.0] \text{ TeV}, \qquad y_L \in [0.5, 3.0],$$

for the HS-MCHM$_5$ and

$$|M_1| \in [2, 30] \text{ TeV}, \qquad |M_4| \in [2, 30] \text{ TeV}, \qquad M_9 \in [2, 30] \text{ TeV},$$
$$f \in [0.8, 8.0] \text{ TeV}, \qquad y_L \in [0.5, 3.0].$$

for the HS-MCHM$_{14}$.

The parameter space of both scenarios is split in the same regions as in the Low Scale analysis (see the definitions in Chapter 4 before Section 4.1). For each model, we generate the events for the $t\bar{t}h$ and $t\bar{t}hh$ processes and their kinematic distributions for 200 random points in each region. The main results are shown

in Figure 5.1 and Figure 5.3, where we joined all points from all regions of the HS-MCHM$_5$ and the HS-MCHM$_{14}$, respectively.

The normalized $t\bar{t}h$ cross section, as a function of f for a center of mass energy of 100 TeV, is illustrated in Figure 5.1. As was already seen in the low scale study, the $t\bar{t}h$ cross section is predominantly dependent on the scale of global symmetry breaking, f. As expected, when f is high, we observe minor deviations from the SM, which are either suppressed or enhanced (only in the MCHM$_{14}$).

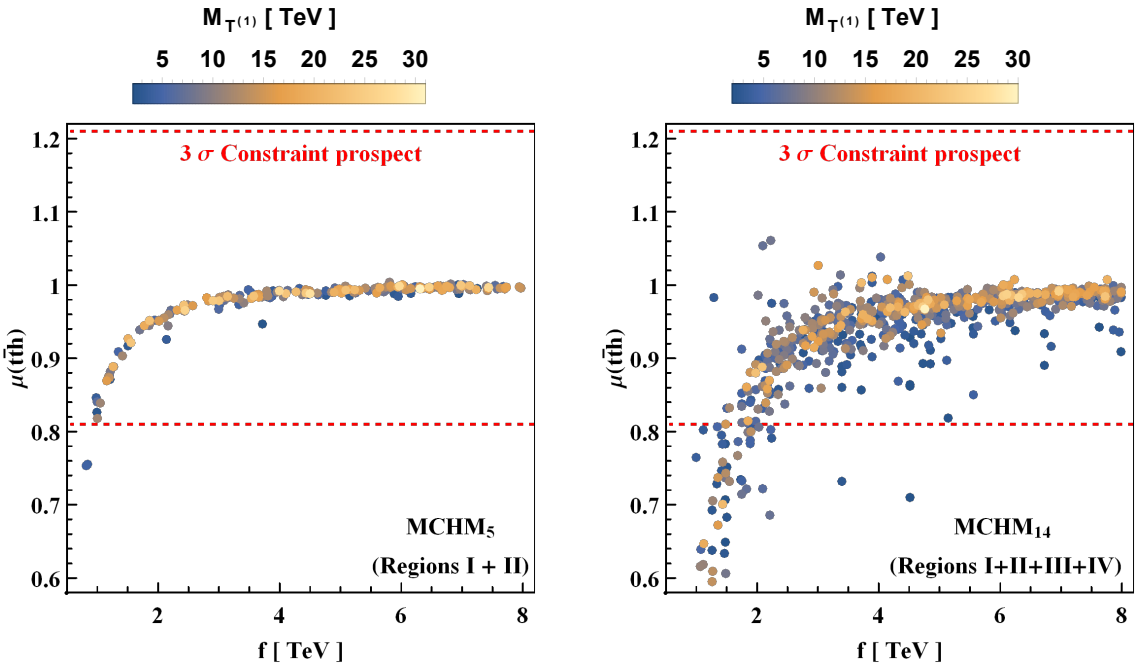

Figure 5.1: Normalized $t\bar{t}h$ cross section as a function of f. We also color code the lightest vector-like mass. These points are obtained by joining all the regions in each model. The dashed red lines represent the prospects for the 3σ uncertainty on the $t\bar{t}h$ signal strength after the HL-LHC measurements (see section 5.2).

Figure 5.3 illustrates the normalized $t\bar{t}hh$ cross section, at $\sqrt{s} = 100$ TeV, as a function of the mass of the lightest top resonance, $M_{T^{(1)}}$, with color coded values of f. As described in section 3.5.2, at low scales, the QCD vector-like pair production is the primary contributor to this cross section. However, this pair production process experiences a rapid decline for heavy resonances. Thus, it is expected that beyond a certain value of $M_{T^{(1)}}$, the QCD resonance pair production becomes a less significant component of the total $t\bar{t}hh$ cross section. The plots in Figure 5.3 indicate that the value of $M_{T^{(1)}}$ at which the cross section becomes independent of $M_{T^{(1)}}$ is approximately 4 TeV. For the MCHM$_5$ case shown in the left plot, there is no point with a

$\mu(t\bar{t}hh)$ greater than one beyond this value. This implies that the non-resonant part of the process, which is directly related to $\mu(t\bar{t}h)$ and always suppressed compared to the SM (as shown in Figure 4.4), becomes the main contributor. Since $\mu(t\bar{t}h)$ is mainly determined by the compositeness scale f (as seen in Figure 5.1), the cross section is strongly suppressed for points with smaller values of f, and approaches the SM limit as f increases.

However, the right plot of Figure 5.3 (pertaining to the MCHM_{14}) reveals that there are still points with significant enhancements relative to the SM beyond $MT^{(1)} \approx 4$ TeV. There are two types of points that exhibit this behavior. Some points display enhancements in the tth Yukawa coupling, which results in NR-$t\bar{t}hh$ enhancements and a corresponding increase of approximately 10% in $t\bar{t}hh$. The second type of point is more intricate and accounts for the greatest cross sections in the region above $M_{T^{(1)}} \approx 4$ TeV. These are finely-tuned points, in which the parameters create a strong-coupling interaction between the top, a vector-like resonance, and the Higgs. This vertex appears in diagrams like the one in Figure 5.2, which produce a single intermediate top partner (not to be confused with weak single production) and also increase the cross section. It is worth noting that the second type of point typically has a low compositeness scale ($f < 2$ TeV) and can be constrained by the increased precision on the measurement of the top Yukawa achievable by the HL-LHC (as illustrated in Fig 5.1).

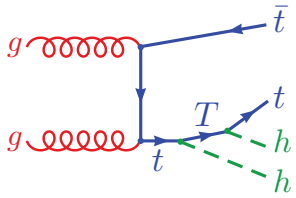

Figure 5.2: Example diagram for the Yukawa mediated single T contribution to $\bar{t}thh$.

5.2 Cluster analysis applied to the HS-MCHM

Following the LS-MCHM analysis of Sections 4.2 and 4.4, now we focus on finding representative points in the parameter space of the HS-MCHMs to examine their phenomenological characteristics. Since the scan covers a wider range of masses, we employ a slightly different clustering technique than the one described in Section 3.7. Specifically, we divided the scan points into smaller sets before clustering

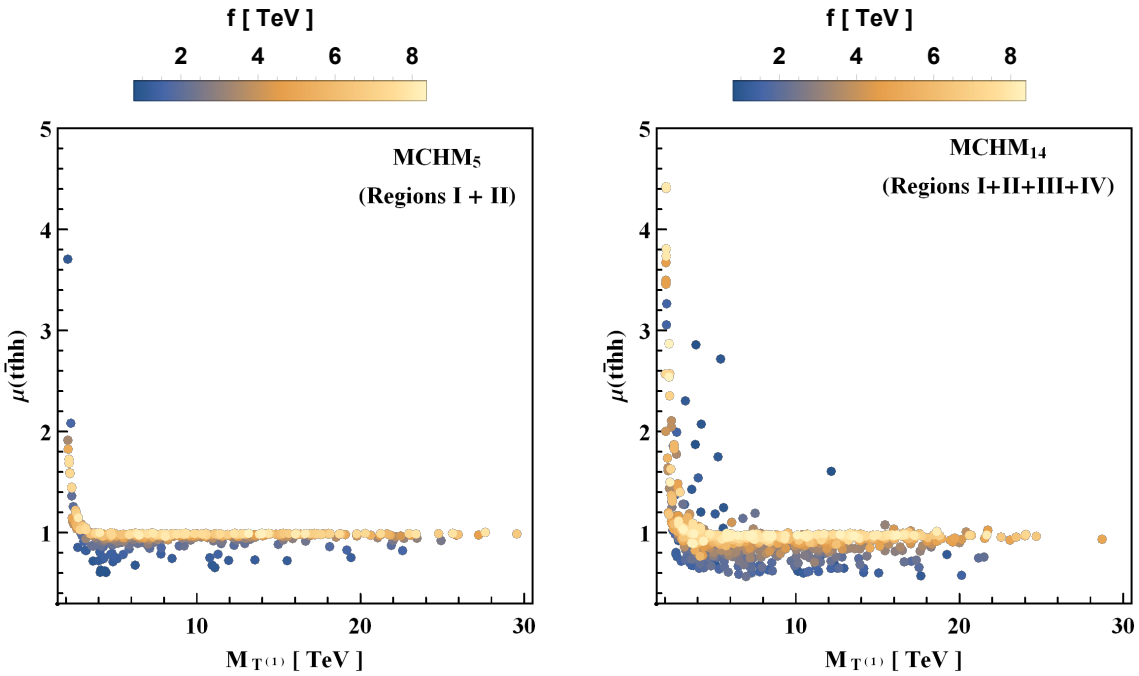

Figure 5.3: Normalized $t\bar{t}hh$ cross section as a function of the lightest $Q = 2/3$ resonance mass at $\sqrt{s} = 100$ TeV. The value of the global scale of symmetry breaking is also color coded. These points are obtained by joining all the regions in each model.

them. This approach, coupled with the fact that the model exhibits a more uniform phenomenological behavior at higher scales, generates sufficient points to highlight all the interesting features of the model. Therefore, we have not selected additional example points for the High Scale scan, and we proceed directly to the results of the clustering algorithm.

5.2.1 Clustering of the HS-MCHM$_5$

We begin by considering the 400 points obtained from the scan in the preceding section (200 in each region) and eliminate all points that do not satisfy the following constraints on κ_t and c_g, which correspond to the top Yukawa coupling and the ggh coupling normalized to the SM value [41]:

$$0.9 \leq \kappa_t \leq 1.1 \tag{5.1}$$

$$0.919 \leq c_g \leq 1.081 \tag{5.2}$$

These constraints are established based on the projected precision of the top Yukawa measurement in the HL-LHC. According to [41], the 1σ uncertainty on κ_t

is predicted to be 3.4% with an accumulated luminosity of 3000 fb^{-1}. To provide a rough estimate of the 3σ region, we limit our points to a range three times that uncertainty around the SM value $\kappa_t = 1$. We do the same for c_g. Our aim is to retain points that are less likely to be restricted by measurements when the 100 TeV pp collider commences its operation. We can use Equation 5.1 to derive constraints on $\mu(t\bar{t}h)$. We display these constraints as red dashed lines in Figure 5.1. These limits allow for relatively small values of $\mu(t\bar{t}h)$ ($\gtrapprox 0.8$). However, towards the end of the HL-LHC phase, the points close to this limit may be on the boundary of the allowed region, and may even be excluded, particularly if the central value of $\mu(t\bar{t}h)$ is above 1 or the precision is higher than anticipated. Nevertheless, it is still possible that the opposite scenario occurs (central value of $\mu(t\bar{t}h) < 1$, for example), so it is premature to discard these points.

We applied the clustering method described in Section 5.1 to the remaining points. Various combinations of kinematic distributions were tested, but in all cases, the clustering process placed too much emphasis on the peak positions of points with lighter resonances. This resulted in numerous low-population clusters for those points, while leaving those with heavier resonances grouped in a single cluster. This issue is comparable to what occurred in the clustering of the low-scale MCHM$_5$ (see cluster 3 in Fig. 4.6), but it is aggravated by the fact that we are now dealing with a broader range of parameters and a greater variety of resonance masses. Since our objective is to select points distributed across the entire parameter space, we decided to group the points into slices based on the mass of the lightest resonance and then apply the clustering algorithm to each slice separately. The following five slices were utilized:

$$\begin{aligned}
&2\text{ TeV} < M_{T^{(1)}} < 3\text{ TeV}\\
&3\text{ TeV} < M_{T^{(1)}} < 4\text{ TeV}\\
&4\text{ TeV} < M_{T^{(1)}} < 5\text{ TeV}\\
&5\text{ TeV} < M_{T^{(1)}} < 6\text{ TeV}\\
&6\text{ TeV} < M_{T^{(1)}} < 30\text{ TeV}
\end{aligned} \tag{5.3}$$

Using this approach, we guarantee to improve the overall homogeneity of the clustering. The final slice includes all the points that have resonances heavier than 6 TeV. This is due to the fact that the contribution of the resonances for these points is

negligible, as seen in Figure 5.3, and it is expected that they possess similar kinematic characteristics. The clustering of these points is carried out by utilizing the $M[t,h_1]$, $p_T[t]$, and $\theta[t]$ distributions and limiting each slice to 2 clusters, resulting in a total of 10 clusters. The detailed clustering plots are shown in Figures D.5 and D.6 in Appendix D, and Table 5.1 provides the corresponding benchmark points for each cluster.

		E_1	E_2	E_3	E_4	E_5	E_6	E_7	E_8	E_9	E_{10}
parameters	M_1(TeV)	22.7	19.2	11.1	23.0	26.5	3.6	19.3	10.5	-10.7	-27.5
	M_4(TeV)	2.4	2.1	3.2	3.2	4.0	22.5	5.1	5.1	25.6	11.3
	f(GeV)	1913	3273	7144	1190	1300	1711	1288	2812	2432	1412
	y_L	2.45	0.87	2.85	2.43	0.99	2.00	2.35	1.84	2.57	1.73
	y_R	1.10	1.24	2.01	1.54	3.53	1.31	2.35	3.13	1.11	2.96
$\mu(t\bar{t}h)$ (All Energies)		0.95	0.97	0.99	0.88	0.83	0.94	0.88	0.97	0.96	0.90
$\mu(t\bar{t}hh)$ (100 TeV)		1.26	1.91	1.03	0.82	0.81	0.86	0.75	0.91	0.92	0.78
NR-$t\bar{t}hh/t\bar{t}hh$ (100 TeV)		0.71	0.48	0.95	0.90	0.82	1.00	1.00	1.02	1.01	1.01
$M_{T^{(1)}}$ (TeV)		2.45	2.12	3.21	3.23	4.07	4.28	5.08	5.15	11.0	11.3
$M_{T^{(2)}}$ (TeV)		5.27	3.55	18.1	4.32	4.28	22.5	5.90	7.31	25.6	11.6
$M_{T^{(3)}}$ (TeV)		22.8	19.7	20.6	23.1	26.9	22.8	19.5	13.7	26.4	27.8
$M_{B^{(1)}}$ (TeV)		5.28	3.55	20.6	4.33	4.24	22.8	5.90	7.30	26.4	11.6
$M_{X_{5/3}}$ (TeV)		2.44	2.11	3.20	3.22	4.04	22.5	5.06	5.14	25.6	11.3
$\Gamma_{T^{(1)}}$ (TeV)		0.04	0.04	0.08	0.14	0.96	0.28	0.76	0.84	1.22	8.97
$\Gamma_{T^{(1)}}/M_{T^{(1)}}$		1.6%	1.9%	2.5%	4.3%	24%	6.5%	15%	16%	11%	79%
BR($T^{(1)}\to$th)		0.35	0.38	0.29	0.29	0.15	0.26	0.18	0.17	0.25	0.05
BR($T^{(1)}\to W^+$b)		0.003	0.004	0	0.001	0	0.50	0	0	0.50	0
BR($T^{(1)}\to$tZ)		0.34	0.37	0.28	0.28	0.33	0.25	0.18	0.18	0.25	0.06
BR($T^{(1)}\to W^+W^-$t)		0.30	0.25	0.43	0.43	0.52	0	0.64	0.65	0	0.89

Table 5.1: Benchmark points for the $MCHM_5$ at high scale and their main features. Red and blue column headings indicate points belonging to Region I and II respectively.

As a first key observation , Table 5.1 reveals the significance of the NR-$t\bar{t}hh$ contribution to the total cross-section. Only in point E_2 it is not the dominant contribution, although even for this point it still constitutes about half of the cross section. Even in the cases where the resonances fall in the 2-3 TeV range (E_1, E_3, and E_4), the NR contribution remains high, with values of 0.7 or greater. As the resonance mass increases, the NR component becomes the dominant factor. Additionally, as the $T^{(1)}$ pair production suppression increases, the $\mu(t\bar{t}hh)$ values get closer to or less than 1 for points with heavier resonances (E_3 to E_{10}), as expected for the NR contribution in $MCHM_5$.

The second remarkable feature that stands out is the prevalence of points with a considerable 3-body decay, with the exceptions of E_6 and E_9. This phenomenon occurs when both $M_{T^{(1)}}$ and $M_{X_{5/3}}$ are mainly determined by M_4, making them almost degenerate (unlike in E_6 and E_9, where $M_{T^{(1)}}$ is closer to M_1). In such cases, there is a noticeable suppression of BR($T^{(1)}\to W^+$b). This effect was already present

in the low scale scan but becomes more prominent here. The table shows that the 3-body decay becomes more significant as $M_{T^{(1)}}$ increases. For the majority of the benchmark points with this characteristic, the 3-body branching ratio increases from around $\sim 10\%$ at $M_{T^{(1)}} \approx 1.3$ TeV (see Table 4.5) to becoming the dominant decay channel at approximately $M_{T^{(1)}} \approx 3$ TeV, where it is already 25% in point E_2 (with $M_{T^{(1)}} = 2.1$ TeV). This emphasizes the importance of taking three body decays into account when attempting to extend the direct search exclusion of top partners. Additionally, the fact that this decay occurs through the exotically charged $X_{5/3}$ highlights the need to examine more comprehensive models of the fermionic sector instead of simplified models that only include a single electroweak doublet or singlet top partner.

In contrast, points E_6 and E_9 demonstrate behavior that is typically accurately modeled by simplified approaches. These cases feature $M_{T^{(1)}} \approx M_1$ being well distinguished from the rest of the spectrum, which is primarily composed of masses close to a significantly higher M_4. Consequently, the branching ratios follow the anticipated trend, with the branching ratio for the W^+b channel being twice that of the th and tZ channels.

Some of the characteristics that were already present in the low scale scan are also observable at higher scales, particularly the occurrence of double-peaked structures in numerous points. Notably, in points E_5 and E_{10} we identify two top partners that are proximate in mass. Furthermore, the exotic $X_{5/3}$ and the bottom partner $B^{(1)}$ are also in close proximity, enabling the 3-body decay to take place via either of these channels. Consequently, the width of $T^{(1)}$ undergoes a significant increase, with $(\Gamma/M)T^{(1)}$ reaching 24% for E_5 and even 79% for E_{10}. Points E_7 and E_8 also demonstrate similar behavior, albeit with a larger mass gap and smaller $(\Gamma/M)_{T^{(1)}}$.

Figure 5.4 displays the scanned points in the M_1 - M_4 plane with f color coding. It also shows the distribution of the benchmark points, which cover both regions of the model. , and we confirmed the uniformity of each cluster. In addition to confirming the uniformity of each cluster, we searched for points with behaviors that differ significantly from the benchmarks but found none. This suggests that the model's behavior is well-represented by the benchmark points, even in regions with a small number of them, such as Region II (negative M_1). Similarly, the same is true for regions with high M_1, M_4, and especially high f, where the points become increasingly similar to each other and the SM as we approach the decoupling limit

of the model. This is why only one point (E_3) was chosen to represent the high f region. Therefore, it would be unnecessary to select additional example points.

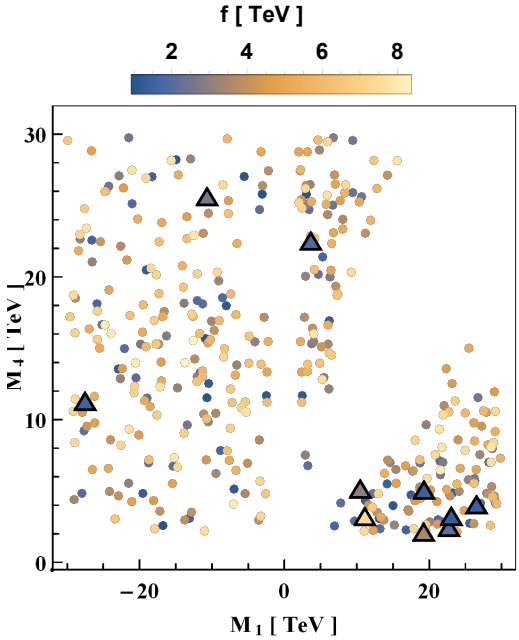

Figure 5.4: High scale scan of the MCHM$_5$ parameter space, including the benchmark points of table 5.1 represented by triangles and the points satisfying the constraint in Eq. 5.1. The compositeness scale f is color coded.

5.2.2 Clustering of the HS-MCHM$_{14}$

For the MCHM$_{14}$ at high scale, we initially began with 800 points that were evenly distributed throughout the four regions of the M_1 - M_4 space, as described in Section 5.1. Next, we selected all the points that adhered to the constraint outlined in Eq. 5.1 and proceeded with the clustering technique. Similarly to the MCHM$_5$, we separated the points into the five slices specified in Eq.5.3. Depending on the level of homogeneity of the clusters, we stopped at 2 or 3 clusters in each slice, and the corresponding benchmark points are listed in Table 5.2. The detailed plots of the clustering are shown in Figures D.5 and D.5 in the Appendix.

Many features are similar to the MCHM$_5$: the NR-$t\bar{t}hh$ once again becomes dominant once $M_{T^{(1)}}$ goes above 3 TeV, and both $\mu(t\bar{t}h)$ and $\mu(t\bar{t}hh)$ go below 1 when that happens. In principle, the MCHM$_{14}$ could allow for an increased top Yukawa and thus $\mu(t\bar{t}h) > 1$ and $\mu(t\bar{t}hh) > 1$ even in the non-resonant regime. Only one point with that behaviour was selected by the algorithm (F_{11}), but all scales for

		F_1	F_2	F_3	F_4	F_5	F_6	F_7	F_8	F_9	F_{10}	F_{11}
parameters	M_1(TeV)	-10.1	4.10	25.2	14.5	-4.20	27.5	-20.0	4.93	24.7	15.3	-16.7
	M_4(TeV)	-2.27	-15.9	3.71	29.6	29.7	11.3	4.04	-10.5	-24.9	7.37	-27.0
	M_9(TeV)	6.16	2.06	10.2	3.31	29.9	4.38	18.7	25.8	5.90	18.6	26.9
	f(TeV)	3.41	4.52	4.89	6.84	7.89	4.35	2.13	4.81	3.19	2.40	4.48
	y_L	1.29	1.83	0.53	2.07	2.41	2.20	2.23	2.58	1.94	2.39	2.38
	y_R	0.83	0.26	1.15	1.53	0.13	1.47	0.61	0.24	1.17	1.83	3.13
$\mu(t\bar{t}h)$ (All Energies)		0.93	0.86	0.96	0.92	0.97	0.98	0.90	0.97	0.90	0.89	1.01
$\mu(t\bar{t}hh)$ (100 TeV)		1.44	3.46	0.93	1.03	0.91	0.99	0.79	0.92	0.77	0.75	1.02
NR-$t\bar{t}hh/t\bar{t}hh$ (100 TeV)		0.59	0.22	0.97	0.81	1.02	0.97	0.99	1.01	1.01	1.02	0.99
$M_{T^{(1)}}$ (TeV)		2.28	2.06	3.72	3.31	4.36	4.38	4.04	5.07	5.90	7.38	21.7
$M_{T^{(2)}}$ (TeV)		4.90	2.06	4.53	3.31	29.7	4.38	6.18	10.45	5.90	9.29	26.9
$M_{T^{(3)}}$ (TeV)		6.16	2.11	10.2	3.35	29.9	4.40	18.7	16.2	5.92	15.9	26.9
$M_{B^{(1)}}$ (TeV)		4.92	2.06	4.52	3.31	29.9	4.38	6.22	16.2	5.90	9.31	26.9
$M_{X^{(1)}_{5/3}}$ (TeV)		2.27	2.06	3.71	3.31	29.7	4.38	4.04	10.5	5.90	7.37	26.9
$\Gamma_{T^{(1)}}$ (TeV)		0.05	0.06	0.24	0.18	0.83	0.25	0.09	0.63	0.60	2.77	45.8
$\Gamma_{T^{(1)}}/M_{T^{(1)}}$		2.2%	3.1%	6.4%	5.4%	19%	5.7%	2.3%	12%	10%	38%	211%
BR($T^{(1)} \to$th)		0.36	0	0.24	0	0.25	0	0.24	0.25	0	0.10	0.04
BR($T^{(1)} \to W^+$b)		0.006	0.27	0.001	0.21	0.50	0.16	0.01	0.50	0.11	0	0.07
BR($T^{(1)} \to$tZ)		0.35	0.53	0.25	0.41	0.25	0.32	0.23	0.25	0.23	0.10	0.03
BR($T^{(1)} \to W^+W^-$t)		0.28	0.20	0.50	0.39	0	0.52	0.52	0	0.66	0.79	0.86

Table 5.2: Benchmark points for the high scale MCHM_{14} scan and their main features. Column headings indicate the region at which the point belongs, with red and orange meaning respectively Regions I and III (with same sign M_1 and M_4) and blue and cyan respectively for regions II and IV (with opposite sign M_1 and M_4).

that point are so high that it is almost SM-like.

Regarding the spectrum and decay of the lightest top partner, while many points exhibit behavior similar to that of MCHM_5, the situation in MCHM_{14} is more diverse:

- The dominant behavior in the MCHM_5 is reproduced by points F_1, F_3, F_7, and F_{10}. The masses of $T^{(1)}$ and $X_{2/3}$ are essentially determined by M_4, with large branching ratios in 3-body decays and suppressed Wb decays. All the important observations made in the MCHM_5 case are applicable here.

- Points F_5 and F_8 exhibit a split spectrum resembling that of E_6 and E_9, where the mass of the top partner is determined by M_1 and the other particles in the spectrum are much heavier. The decay patterns follow those of the simplified models.

- The points F_2, F_4, F_6 and F_9 represent a novel scenario. These points have a mass scale mainly determined by M_9, and feature three top partners that are not only degenerate with each other, but also coincide in mass with the lightest exotically charged fermion and the bottom partner. Unlike the degenerate cases observed in MCHM_5, the width of $T^{(1)}$ does not increase in these points, and there is a suppression of the th channel. To disentangle these states

and determine their contribution to $t\bar{t}hh$, it would be necessary to conduct a thorough survey of all decay channels of $T^{(2)}$ and $T^{(3)}$, which is beyond the scope of this work.

Additionally, unlike F_4 and F_6, F_2 may potentially be confirmed at a 100 TeV machine due to the significant deviation from the SM observed in $\mu(tthh)$, as well as the high precision measurement of $\mu(tth)$, assuming it remains valid after the HL-LHC.

- The F_{11} is really SM-like in terms of several experimental observables. Even with the high precision achievable in $\mu(tth)$ and $\mu(tthh)$ measurements at a 100 TeV collider, it would not be possible to distinguish them from the SM. Additionally, the point has a very high mass and a highly degenerate resonance spectrum in M_4 and M_9, with a dominant 3-body decay of $T^{(1)}$ as a notable feature. It should be noted that points F_5 and F_8 share the same highly degenerate resonance spectrum in M_4 and M_9, but they have a decay channel pattern similar to simplified models. Further phenomenological and experimental studies would be necessary to fully disentangle the F_{11} point, but it is beyond the scope of this work.

The M_1-M_4 plane with color coded values of f is illustrated in Figure 5.5 to display the benchmark points. The clustering of the benchmark points covers this space uniformly, and thus we opted not to include example points.

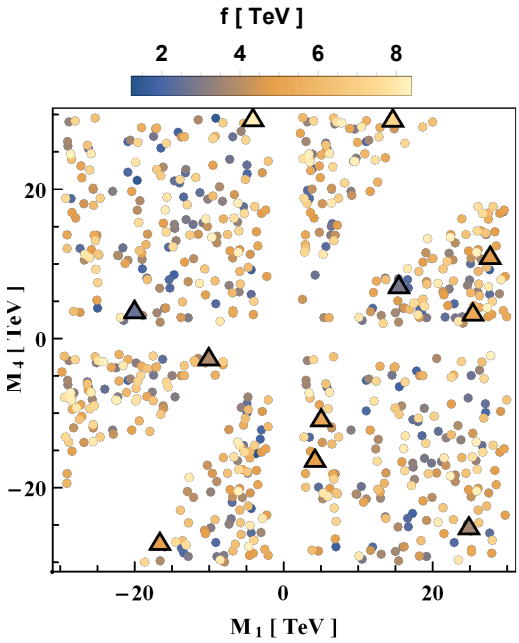

Figure 5.5: High scale scan of the MCHM_{14} parameter space, including the benchmark points of table 5.2 represented by triangles and the points satisfying the constraint in Eq. 5.1. The compositeness scale f is color coded.

Chapter 6

Three body decays in the MCHM$_5$

In Tables 4.5, 4.6, 5.1 and 5.2 we saw that there are points in the parameter space of the MCHM$_5$ and the MCHM$_{14}$ with a $T^{(1)}$ resonance with a sizable three body decay into W^+W^-t. Such decay channels are usually not consider in experimental searches, where two-body decays saturate the resonances width. In this chapter we explore the three body decays in more detail focusing on the MCHM$_5$ and in the following chapters we explore the implications of the existence of these decay channels on experimental studies.

A list of all two and three body decays of the resonances in the MCHM$_5$ is shown in Table 6.1, where T represents any of the three $2/3$ charged resonances; B, the $-1/3$ charged resonance and $X_{5/3}$, the $5/3$ charged resonance. The existence of these channels is conditioned by the phase space at each point in the model's parameter space. For instance, $T^{(2)}$ can only decay into $W^+W^-T^{(1)}$ if $M_{T^{(2)}} > 2M_W + M_{T^{(1)}}$. Also, we have to be careful to consider only the Feynman diagrams that contribute with off-shell intermediate states. For example, let us consider the decay $T^{(1)} \to b\bar{b}t$. In Figure 6.1 we show in (a) the only Feynman diagram contributing to this decay channel. Although the diagrams in (b) also produce the final states $b\bar{b}t$ from a T resonance, we can not consider them as being part of a 3-body decay because the intermediate h and Z bosons are on-shell, as the decays $h \to b\bar{b}$ and $Z \to b\bar{b}$ are kinematically allowed. In fact, these processes would represent two consecutive 2-body decays ($T \to th(Z)$ followed by $h(Z) \to b\bar{b}$) and including them would imply that we are considering redundant contributions.

Although there exists a variety of three body decays, most of them have a low branching ratio, either because the intermediate states are very off-shell or because they contain vertices that couple states belonging to different multiplets, making them negligible [90]. We found that the decay channels $T \to W^+W^-t$, $X_{5/3} \to W^+th$ and $X_{5/3} \to W^+tZ$ are the most important depending on the nature of the lightest T resonance. Before studying these decay channels deeply, we will make some defini-

	T	B	$X_{5/3}$
2-body decays	ht, hT Zt, ZT W^+b, W^+B $W^-X_{5/3}$	hb Zb W^-t, W^-T	W^+t, W^+T
3-body decays	W^+W^-t, W^+W^-T $W^-hX_{5/3}$ $W^-ZX_{5/3}$ $\bar{t}tt$, $\bar{T}tt$, $\bar{t}Tt$, $\bar{T}Tt$, $\bar{t}TT$ $\bar{t}bX_{5/3}$, $\bar{T}bX_{5/3}$, $\bar{t}BX_{5/3}$, $\bar{t}BX_{5/3}$ $\bar{b}hW^+$, $\bar{B}hW^+$ $\bar{b}ZW^+$, $\bar{B}ZW^+$ $b\bar{b}t$, $B\bar{b}t$, $b\bar{B}t$, $b\bar{b}T$, $B\bar{b}T$, $b\bar{B}T$ hht, hZt, ZZt, hhT, hZT, ZZT	$\bar{t}bt$, $\bar{t}bT$, $\bar{T}bt$, $\bar{T}bT$ bhh, bhZ, bZZ $W^-W^-X_{5/3}$ W^-bW^+ W^-ht, W^-hT W^-Zt, W^-ZT	W^+W^+b W^+th, W^+Th W^+tZ, W^+TZ $\bar{b}tt$, $\bar{b}Tt$, $\bar{b}TT$

Table 6.1: Two and three body decays of the resonances in the MCHM$_5$. T represents any of the three $2/3$ charged resonances and B and $X_{5/3}$, the $-1/3$ and $5/3$ charged resonances respectively. Phase space constraints may forbid many of these channels.

tions regarding these aspects.

The mass of the $2/3$ charged lightest top partner, $T^{(1)}$, is determined, as explained in Eq. 3.12, by the diagonalization of the mass matrix $\mathcal{M}_{2/3}$. In this way, the mass term of $T^{(1)}$ is given by:

$$-M_{T^{(1)}}\overline{T^{(1)}}_L T^{(1)}_R \tag{6.1}$$

with:

$$T^{(1)}_L = U_{L,21}t_L + U_{L,22}T_L + U_{L,23}X_{2/3L} + U_{L,24}\tilde{T}_L \tag{6.2}$$

and

$$T^{(1)}_R = U_{R,21}t_R + U_{R,22}T_R + U_{R,23}X_{2/3R} + U_{R,24}\tilde{T}_R \tag{6.3}$$

where the right side of the eqs. 6.2 and 6.3 contains the gauge-basis fields defined in Eq. 2.4. That is, $M_{T^{(1)}}$ receives the contributions of both $SO(4)$ multiplets in 2.4. When the mass of one of the multiplets (M_1 or M_4) is much larger than the other, it is clear that the multiplet with the lower mass contributes the most to the mass of $T^{(1)}$. However, when the masses are of the same order, the contributions of both multiplets can overlap. As the properties of $T^{(1)}$ depend on how much contribution it received from the multiplets, it would be useful if we establish a way to quantify their fourplet and singlet contributions. Since each chirality of $T^{(1)}$ have different multiplet contributions, we will first define the *left (right) fourplet contribution* for each chirality as:

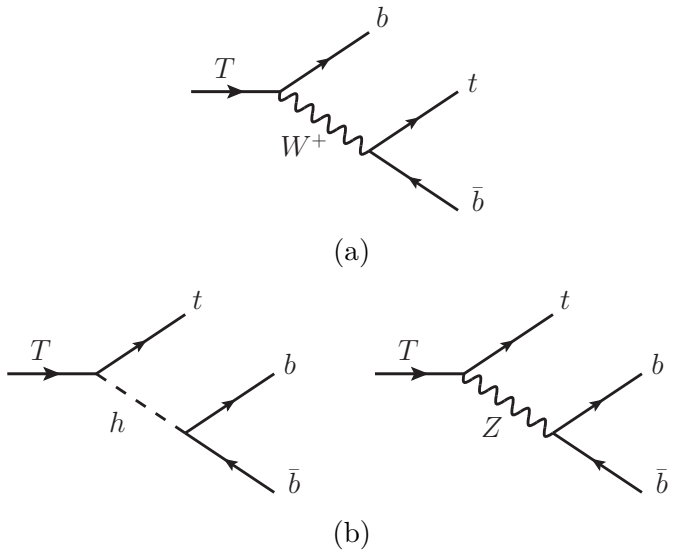

Figure 6.1: (a) Feynman diagram representing the only contribution to the 3-body decay $T \to b\bar{b}t$. (b) Feynman diagrams that produce the final state $b\bar{b}t$ from T but do not constitute a 3-body decay as the intermediate states h and Z are on-shell.

$$\eta^F_{L(R)} = U^2_{L(R),22} + U^2_{L(R),23} \tag{6.4}$$

and the *left (right) singlet contribution* as:

$$\eta^S_{L(R)} = U^2_{L(R),21} + U^2_{L(R),24} \tag{6.5}$$

Then, we define

$$\sin^2\theta = \frac{\eta^F_L + \eta^F_R}{2} \quad \text{and} \quad \cos^2\theta = \frac{\eta^S_L + \eta^S_R}{2}, \tag{6.6}$$

to help us measure the total fourplet/singlet contributions to $T^{(1)}$. A MCHM$_5$ point will be a pure fourplet if $\theta = \pi/2$ and a pure singlet when $\theta = 0$. We will define a point in the parameter space of the MCHM$_5$ to be *fourplet-like* if $\theta \geq \pi/4$ and *singlet-like* if $\theta < \pi/4$. We must keep in mind that this classification is not always accurate, since there are points in which no multiplet is clearly the most important. For these points this classification does not make sense. However, we will not worry about excluding those points because we only want to understand general features that differentiate fourplet-like from singlet-like points.

Since the most important contributions to cross sections come from the lightest

resonances, we will only consider here the 3-body decays of the lightest states. As mentioned in sections 2.1 and 3.3, the masses of the five resonances in the MCHM$_5$, up to electroweak corrections are:

$$M_T = \sqrt{M_1^2 + y_R^2 f^2}, \quad M_4, \quad \sqrt{M_4^2 + y_L^2 f^2} \tag{6.7}$$

$$M_B = \sqrt{M_4^2 + y_L^2 f^2} \tag{6.8}$$

$$M_{X_{5/3}} = M_4 \tag{6.9}$$

where resonances with the same mass belong to the same $SU(2)$ multiplet. This set of masses implies two possible scenarios for the lightest states:

- If $\sqrt{M_1^2 + y_R^2 f^2} < M_4$, the $2/3$ charged resonance with mass $\sqrt{M_1^2 + y_R^2 f^2}$ is the lightest state.
- If $\sqrt{M_1^2 + y_R^2 f^2} > M_4$, the $2/3$ charged resonance with mass M_4 and the $X_{5/3}$ resonances are both the lightest states (degenerate up to EW corrections).

The states with masses $\sqrt{M_4^2 + y_L^2 f^2}$ (The B resonance and one of the T resonances) are never the lightest states. Then, their cross section contributions for the processes analyzed in the present study (for instance, in resonance double production) are subdominant. For this reason, in this chapter we will only consider the three body decays of the states mentioned in the two scenarios listed above.

6.1 $T^{(1)}$ decays

When $T^{(1)}$ is the lightest BSM state, the allowed decay channels are the ones with only SM final states in Table 6.1. Those are the two body decay channels ht, Zt and W^+b and the three body ones W^+W^-t, $\bar{t}tt$, $\bar{b}hW^+$, $\bar{b}ZW^+$, $b\bar{b}t$, hht, hZt and ZZt.

In Figure 6.2 we show the distributions of the three body decays branching ratios of $T^{(1)}$ for the points in the LS-MCHM$_5$ parameter space scan after the constraints in Equations 4.1, 4.2 and 4.3. At the top, the distributions of all points are shown. The branching ratio distribution of the decay into W^+W^-t is shown in blue and the sum of the branching ratios into the remaining three body decays is shown in orange. There we can see that there are two regions in which the values of the branching ratio of the W^+W^-t channel are more frequent: one narrow region around 0.02 (with about 35% of the points), and other wider region

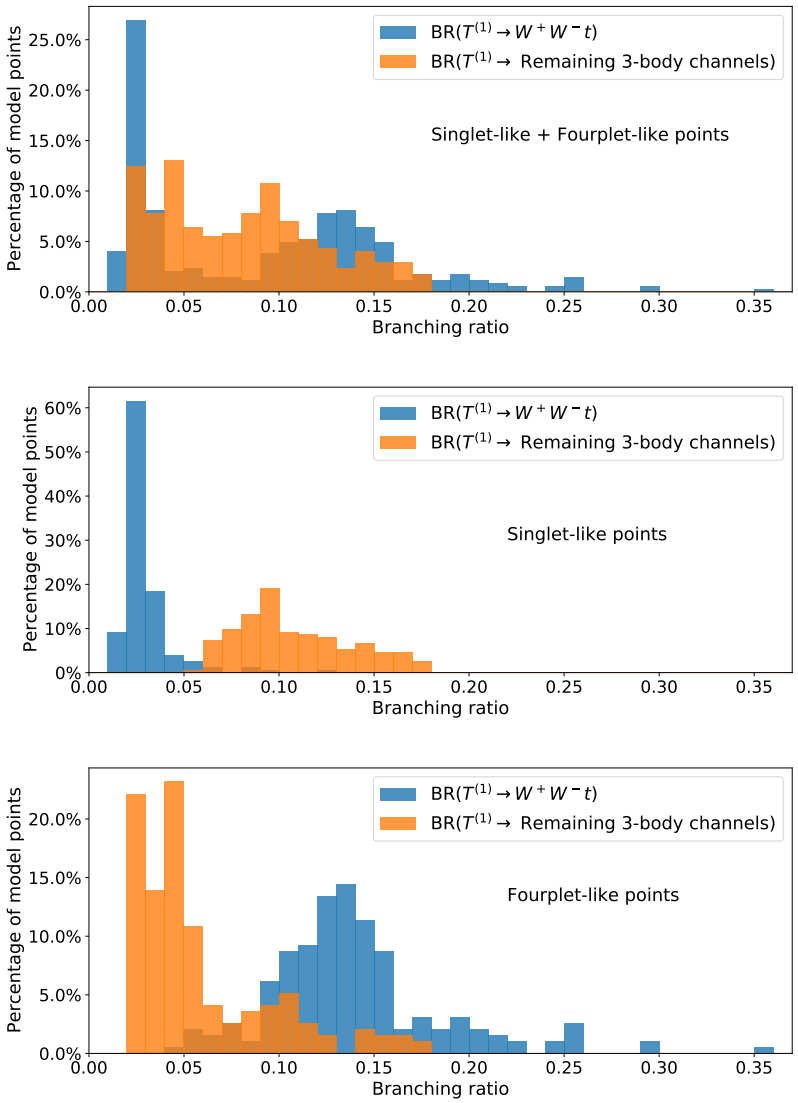

Figure 6.2: Distributions of the branching ratio of the $T^{(1)} \to W^+W^-t$ channel (in blue) and the sum of the remaining three body decay channels (in orange). The remaining three body channels are $\bar{t}tt$, $\bar{b}hW^+$, $\bar{b}ZW^+$, $b\bar{b}t$, hht, hZt and ZZt. At top, all points in the scan are shown. At the middle (bottom), only singlet-like (fourplet-like) points are shown.

around 0.13 (with about 40% of the points). There are some less frequent values above 0.16 that can even get as large as 0.35. For the sum of the branching ratios of the rest of the 3-body decays channels it is more difficult to identify separated regions.

The reason for this clustering of points is better understood if we split the points into groups of singlet-like and fourplet-like points. The corresponding distributions for each group are shown at the middle and bottom plots of Figure 6.2. There, we can see that the two previously mentioned regions of the W^+W^-t branching ratios correspond to the two different point types, being the singlet-like points the ones that generally lie into the range with smaller values and the fourplet-like points the ones that generally lie into the range with larger values. On the other hand, the sum of the remaining 3 body channels is more important than the W^+W^-t channel in the singlet-like points whereas less important for fourplet-like points.

The difference in branching ratios of the W^+W^-t channel in the singlet-like and fourplet-like points has two reasons: the different interference behaviours of the diagrams contributing to the W^+W^-t channel and the negligible values of the W^+b two body channel in the fourplet-like points. Let us explore these points more deeply.

In Figure 6.3 we show the five Feynman diagrams contributing to the $T \to W^+W^-t$ decay channel, where T represent any 2/3-charged resonance. These diagrams are mediated by $X_{5/3}$, h, Z, b and B, respectively. If we focus on the lightest 2/3-charged resonance $T = T^{(1)}$, the diagram with an intermediate B can be neglected, since the resonances $T^{(1)}$ and B always come from different $SU(2)$ multiplets implying a negligible $T^{(1)} - B - W$ coupling. On the other hand, the magnitude of the $T^{(1)}X_{5/3}W$ and $T^{(1)}bW$ couplings depend on the singlet-like or fourplet-like nature of $T^{(1)}$. $T^{(1)}$ will couple weakly with states with different hypercharge. Then, for singlet-like (fourplet-like) points, the $T^{(1)}X_{5/3}W$ ($T^{(1)}bW$) coupling is negligible.

This can be seen in Figure 6.4, where we show the distributions of each of the diagrams contributing to the $T^{(1)}$ decay into W^+W^-t in Figure 6.3, normalized to the width of $T \to W^+W^-t$. At the top, the distributions for the singlet-like points are shown. As already mentioned, the contributions of the B- and $X_{5/3}$-mediated diagrams are negligible, while the h-, Z- and b- mediated diagrams have sizable values. We can notice that the sum of the ratios can be larger than one and, moreover, there are points for which the Higgs- and bottom-mediated widths alone exceed the

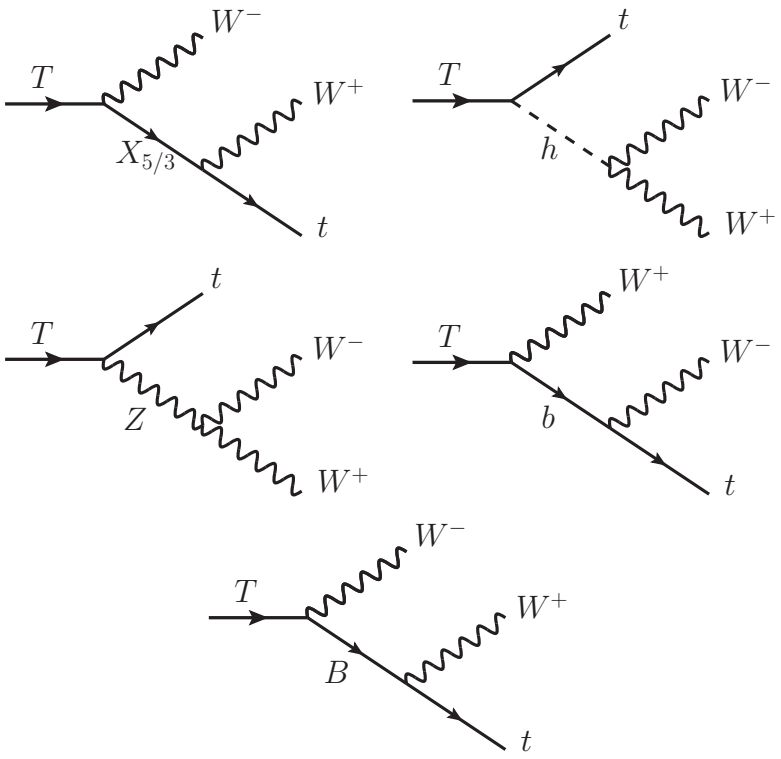

Figure 6.3: Feynman diagrams of the three body decay $T \to W^+W^-t$.

total $T \to W^+W^-t$ width. This indicates the presence of strong negative interference between the diagrams. At the bottom of Figure 6.4, the distributions for the fourplet-like points are shown. For these points, we see that the negligible diagrams are the B- and b-mediated ones, while the sizable ones are the h-, Z-, $X_{5/3}$-mediated diagrams. Unlike the singlet-like case, here, the small values of the width, signal a positive interference between the diagrams. This difference in interference behavior generally leads the fourplet-like points to exhibit larger W^+W^-t decay widths than the singlet-like points.

However, this is not enough to explain the difference in W^+W^-t branching ratios. Let us see how the $T^{(1)}$ two-body decays - ht, Zt and W^+b - behave. In Figure 6.5 the distributions of the two body decay's branching ratios for singlet-like points (at the top) and fourplet-like points (at the bottom) are shown. There we can see that the W^+b channel branching ratio takes values around 0.42 for most of the singlet-like points, while values less than 0.02 for most of the fourplet-like points. This is due to the previously mentioned negligibility of the $T^{(1)}bW$ vertex in the fourplet-like points. This is the main factor contributing to the importance of the three body

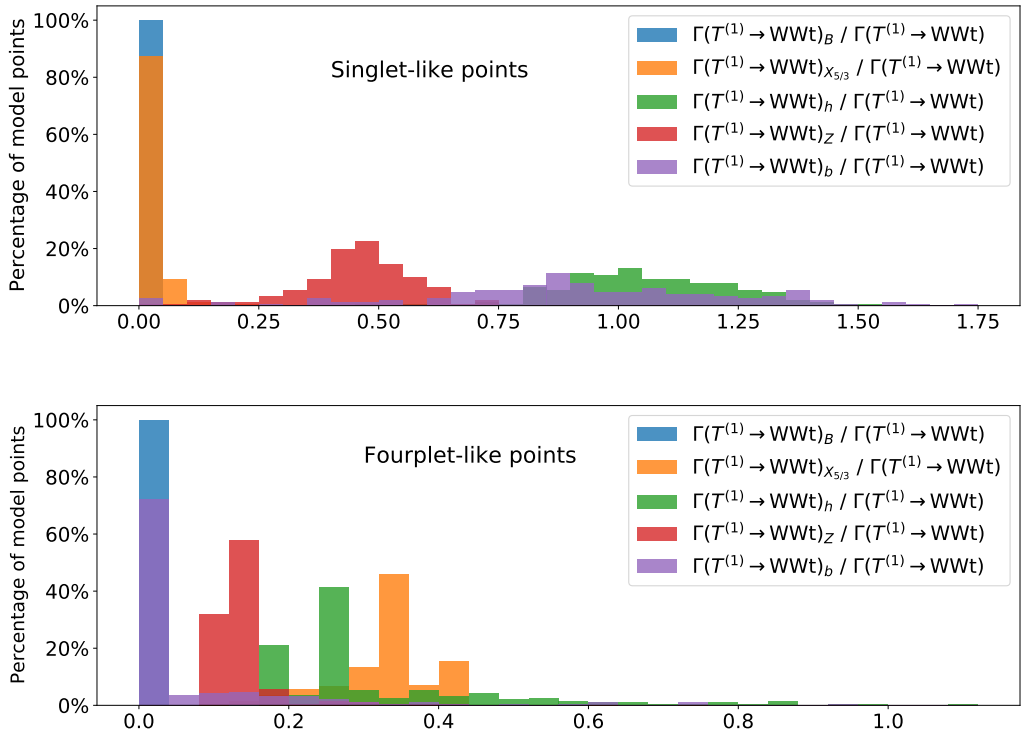

Figure 6.4: Distributions of the widths of each of the diagrams in Figure 6.3 normalized to the total decay width into WWt for singlet-like(fourplet-points) points at the top(bottom).

decay W^+W^-t BR in the fourplet-like points. While in the singlet-like points, W^+b is the most important channel (with a BR of almost 0.5), it almost disappears in the fourplet-like points making the W^+W^-t more important.

It is important to note that, in the absence of the three body decays, the values of BRs shown in Figure 6.5 are close to the naively expected values: $\text{BR}(th) \approx \text{BR}(tZ) \approx \frac{1}{2}\text{BR}(W^+b) \approx 0.25$ for singlets and $\text{BR}(th) \approx \text{BR}(tZ) \approx 0.5$, $\text{BR}(W^+b) \approx 0$ for fourplets. These are the values usually considered when studying the MCHM collider phenomenology [90] or establishing exclusion limits for resonance masses.

6.2 $X_{5/3}$ decays

When $X_{5/3}$ is the lightest BSM state, the only allowed 2-body decay is W^+t and the 3-body decay channels are W^+tZ, W^+th, $\bar{b}tt$ and W^+W^+b. Their corresponding

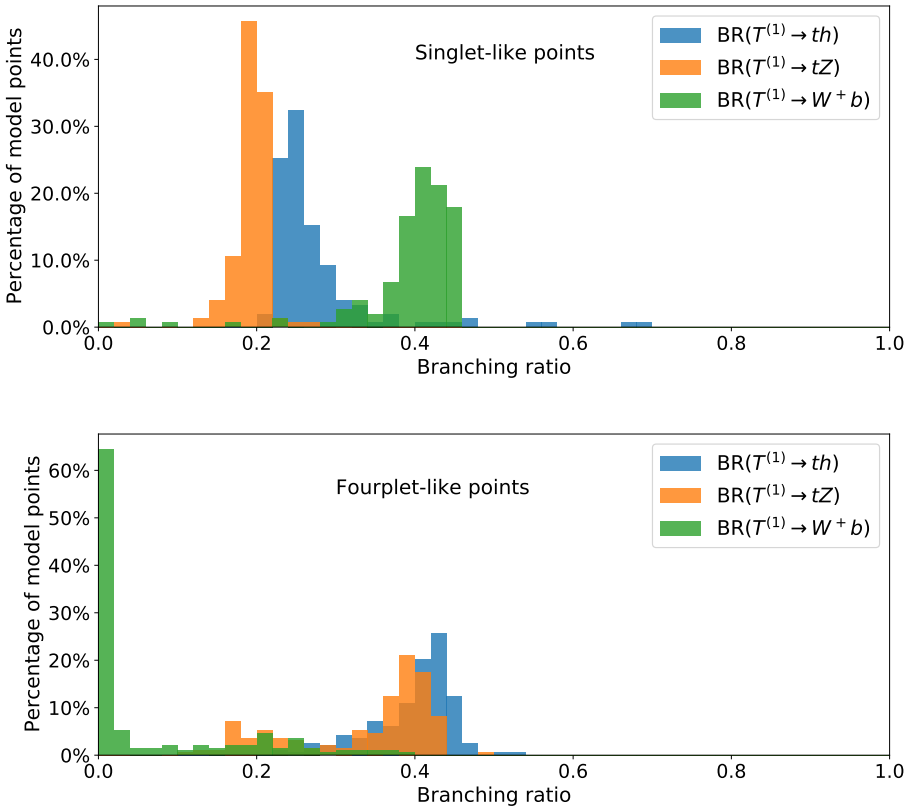

Figure 6.5: Distribution of two body decays' branching ratios of the $T^{(1)}$ resonance in singlet-like points (at the top) and fourplet-like points (at the bottom).

Feynman diagrams are shown in Figure 6.6. We should remember that, in the three-body decays the processes with two consecutive two-body decays must not be considered. For instance, in the $X_{5/3} \to W^+W^+tb$ decay in Figure 6.6d, we are not considering the diagram with a top quark as a mediator, since that would be equivalent to a two-body decay $X_{5/3} \to W^+t$ followed by the decay $t \to W^+b$. On the other hand, the diagrams with off-shell 2/3 charged top partners as mediators do contribute to the three-body decay.

In Figure 6.7, the distributions of the $X_{5/3}$ decay's BR are shown, with the distribution of $\mathrm{BR}(X_{5/3} \to W^+t)$ shown in blue. The sum $\mathrm{BR}(X_{5/3} \to W^+th) + \mathrm{BR}(X_{5/3} \to W^+tZ)$ is shown in orange and the sum $\mathrm{BR}(X_{5/3} \to \bar{b}tt) + \mathrm{BR}(X_{5/3} \to W^+W^+b)$, in green. The channels $\bar{b}tt$ and W^+W^+b were grouped because of their low BR's. Their sum generally lies between 0 and 0.03. The channels W^+th and W^+tZ were grouped because of their similar partial decay widths. Jointly, they usually get values around 15%, but they can represent up to 40% of the total $X_{5/3}$ width. Finally, the only two-body decay channel, W^+t, is the dominant one, with branching ratios between 0.5 up to 0.9. This last channel is usually the only one considered in experimental searches ($\mathrm{BR}(X_{5/3} \to W^+t) = 1$) [37, 38, 39]. In the present work we will analyze the effects that the most dominant three-body decay channels, W^+th and W^+tZ, would have in $X_{5/3}$ searches for fourplet-like points.

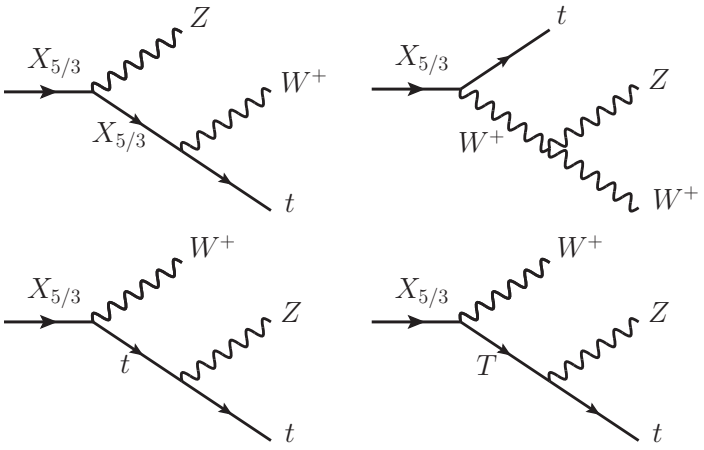

(a) $X_{5/3} \to W^+tZ$ diagrams.

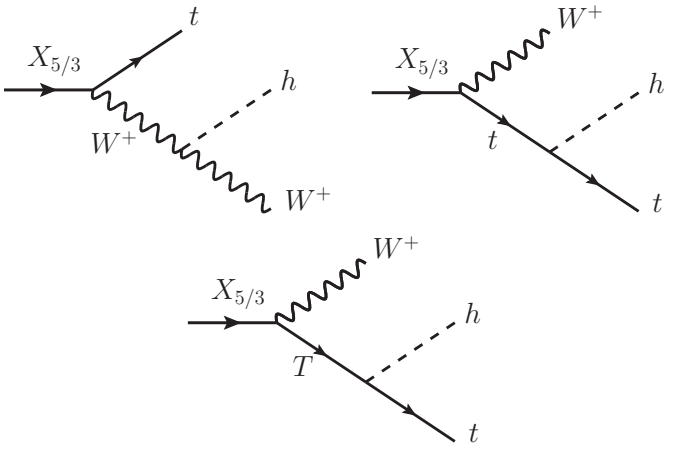

(b) $X_{5/3} \to W^+th$ diagrams.

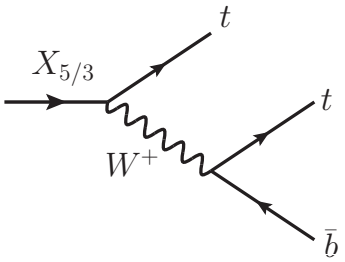

(c) $X_{5/3} \to \bar{b}tt$ diagram.

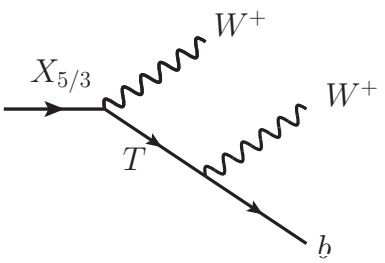

(d) $X_{5/3} \to W^+W^+b$ diagram.

Figure 6.6: Feynman diagrams of the three body decays of $X_{5/3}$ into SM particles.

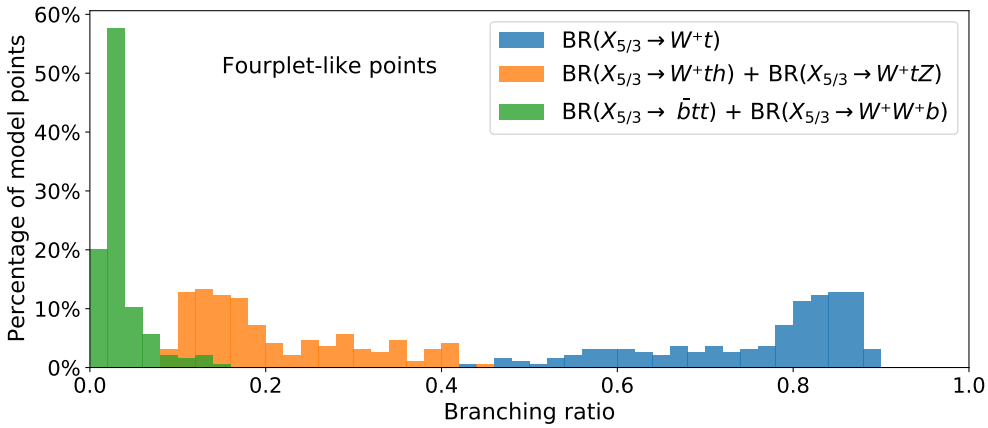

Figure 6.7: Distribution of the branching ratios of the 5/3 charged resonance ($X_{5/3}$) decays for fourplet-like points.

Chapter 7

Effects of three body decay channels on current VLQ experimental searches

The experimental searches of vector-like quarks (VLQ) performed so far at the LHC consider a simple VLQ scenario and assume that they decay exclusively into two-body final states. In the case of the 2/3-charged VLQ, the considered decays are into th, tZ and W^+b [31, 32, 33, 34, 35, 36], and for a 5/3-charged VLQ, the naive expectation is that it decays to W^+t with a 100% branching ratio [37, 38, 39]. However, in the previous chapter we saw that 3−body decay channels can have sizable contributions of around $10\% - 15\%$ to the total decay width in fourplet-like points of the MCHM$_5$. In this chapter, we will make a rough estimation of the effect that the inclusion of such decay channels would have in the mass exclusion limits obtained by the latest experimental analyses. Specifically, we will focus on [40] for the $T^{(1)}$ resonance and on [39] for the $X_{5/3}$ resonance (particular features of these studies will be described in the first paragraphs of Sections 7.3 and 7.4, respectively). They both follow a general analysis framework, which will be described in Section 7.1. In Section 7.2 we will describe our analysis strategy and, finally, Sections 7.3 and 7.4 will present the specific features of the analyses we made for the $T^{(1)}$ and $X_{5/3}$ resonance searches, respectively, along with the results obtained.

7.1 General description of existing experimental searches

The experimental searches at the LHC for the two heavy mass resonances with electric charges 2/3 and 5/3, respectively, follow the same general analysis framework. First, a discrete set of resonance masses in an interval is defined. For each mass, they simulate the signal events of pair produced resonances decaying exclusively into the two-body decays mentioned above, at leading order (LO). The distributions are then normalized to the next-to-next-to leading order (NNLO) cross section and weighted to

produce the desired combinations of branching ratios. A particular search channel is chosen and the background events contributing to that channel are generated. Then, the event selection and reconstruction is performed using cut-based or neural network analyses that enhances signal-background discrimination. An statistical analysis is done, afterwards, to determine the upper limits at 95% confidence level(CL) of the cross section of the resonance pair production for each mass in the discrete interval.

The results for the most recent experimental searches are shown in Figures 7.1 (for the T top partner) and 7.2 (for the $X_{5/3}$ top partner). There, the red line represents the theoretical cross section of resonance pair production. The black and dashed lines represent, respectively, the observed and expected signal cross section upper limit at 95% CL. The bands around the median expected limit (dashed line) represent the 68% (green) and 95% (yellow) confidence intervals for the expected experimental limits under the background-only hypothesis. These correspond to 1σ and 2σ ranges, respectively. The intersection between the red and black lines sets the resonance mass lower limit at 95% CL. We will further describe these plots in Sections 7.3 and 7.4.

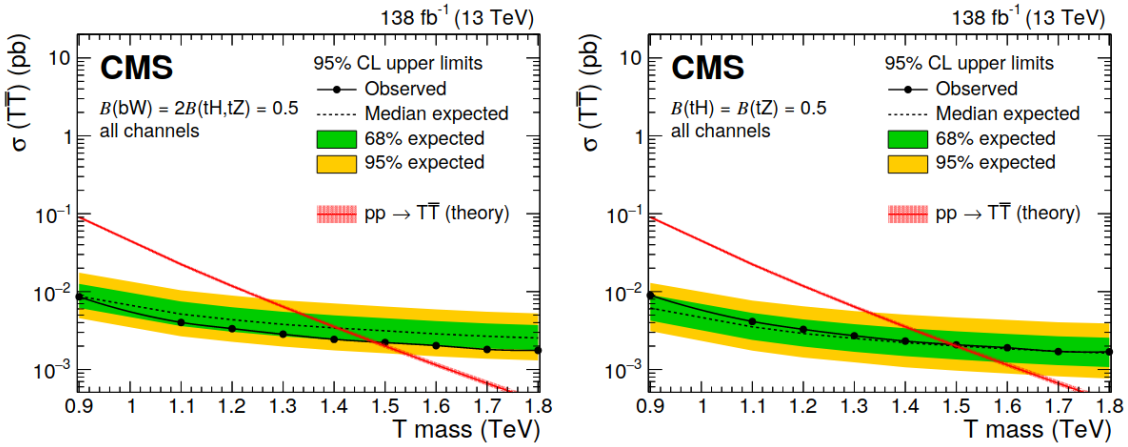

Figure 7.1: Expected and observed limits of the signal cross section upper limit at 95% CL for the simplified singlet (left) and simplified doublet (right) scenarios obtained by combining the analyses done in [40] from single lepton, same-sign dilepton and multilepton channels. The band around the theoretical prediction shows the theoretical uncertainty. Figure extracted from [40].

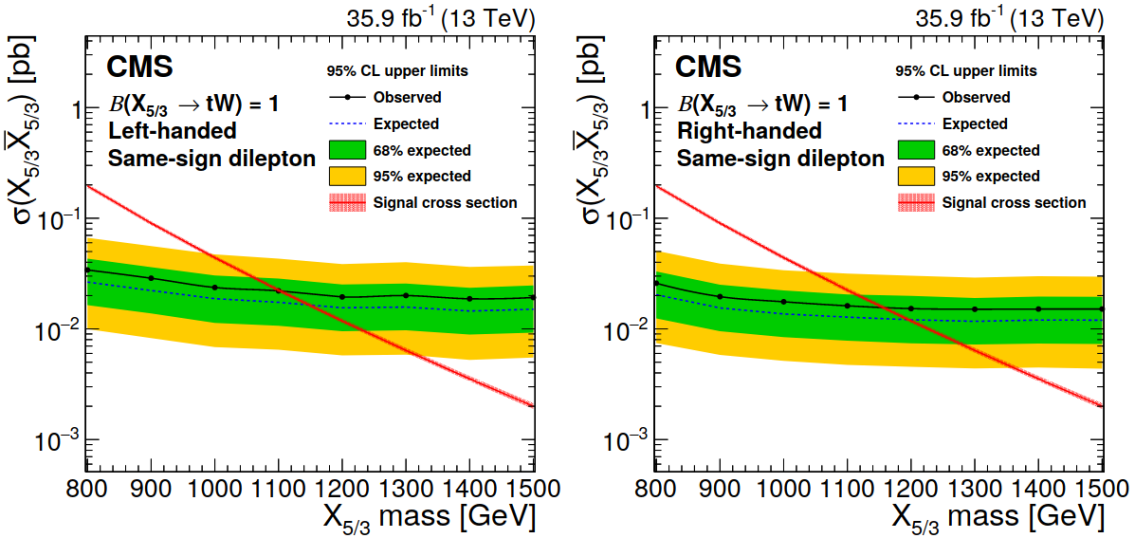

Figure 7.2: Expected and observed upper limits of the signal cross section at 95% CL for an LH (left) and RH (right) $X_{5/3}$ from the same-sign dilepton search performed by [39]. The band around the theoretical prediction shows the theoretical uncertainty. Figure extracted from [39].

7.2 Analysis strategy

Our aim in this chapter is to analyze what would be the effect of the introduction of three body decays in the experimental analyses mentioned above. Since in Figures 7.1 and 7.2, the theoretical resonance pair production (red line) will not be modified at all by the introduction of such new decay channels, we only can expect to estimate changes in the expected (black lines) signal cross sections and subsequently, estimate the change in the resonance mass exclusion limits.

For that, we will consider the same set of resonance masses considered in the experimental analyses. Then, for each resonance mass, we will take a point of the parameter space of the MCHM$_5$ with the corresponding mass. These points have arbitrary branching ratios. To consider the desired ones we re-scale the cross sections (number of events) accordingly. We simulate the signal events for resonance pair production with inclusive decays into two and three-body final states [1]. In that way, for each resonance mass, we will have one set of simulated events for each possible pair combination of decay channels (one for each resonance). All processes are simulated with Madgraph5 (v2.9) [74] at LO and $\sqrt{s} = 13$ TeV. The events, then, are showered and hadronized using Pythia8 [91] and finally passed through Delphes3

[1] All the computations will be done at LO.

(v3.5.0) [92] for a fast detector analysis. The output of the detector simulation is then extracted and analysed using ROOT [93].

In order to simulate specific branching ratio scenarios we will re-scale the distributions obtained from the events, in such a way that the cross section is given by:

$$\sigma_{R\bar{R}\to D_1\bar{D}_2}\left[\mathrm{BR}(D_1),\mathrm{BR}(D_2)\right] = \sigma_{R\bar{R}} \times F\left[\mathrm{BR}(D_1),\mathrm{BR}(D_2)\right] \tag{7.1}$$

where R represents the VLQ particle ($X_{5/3}$ or $T^{(1)}$), D_1 and D_2 represent the possible decay channels, $\sigma_{R\bar{R}}$ is the cross section of the resonance pair production ($p\bar{p} \to R\bar{R}$), and F is a factor that depends on the branching ratios of the channels involved in the process as follows:

$$F\left[\mathrm{BR}(D_1),\mathrm{BR}(D_2)\right] = \begin{cases} \left[\mathrm{BR}(D)\right]^2 & \text{, if } D_1 = D_2 = D \\ 2 \times \mathrm{BR}(D_1) \times \mathrm{BR}(D_2) & \text{, if } D_1 \neq D_2 \end{cases} \tag{7.2}$$

Since the sum of BRs equals 1, it follows that

$$\sum_{D_1,D_2} F[\mathrm{BR}(D_1),\mathrm{BR}(D_2)] = 1 \tag{7.3}$$

We will not simulate background events as they will not be modified with the inclusion of three-body decay channels. For a given search channel, we will apply the same cuts on the kinematical distributions as in the experimental analysis. For reasons of complexity in reproducing the analysis, we left the search channels based on neural network algorithms for a future work.

Depending on the search channel, the detector will have an efficiency in reconstructing the required final states. Furthermore, the cuts will impose different restrictions on each process with specific BRs combination. Then, the number of surviving events for each of these processes will be given by

$$N^{\mathrm{CUT}}_{R\bar{R}\to D_1\bar{D}_2}[\mathrm{BR}(D_1)\mathrm{BR}(D_2)] = \sigma_{R\bar{R}\to D_1\bar{D}_2}[\mathrm{BR}(D_1),\mathrm{BR}(D_2)] \times \xi_{D_1,D_2} \times \mathcal{L} \tag{7.4}$$

where $\mathcal{L}$ is the luminosity and ξ_{D_1,D_2} is a factor that encapsulate the detector and

cuts efficiencies. The total number of surviving events is

$$N^{\text{CUT}} = \sum_{D_1, D_2} N^{\text{CUT}}_{R\bar{R}\to D_1\bar{D}_2} \tag{7.5}$$

After that, we can compare the total number of surviving events of the scenarios with and without three body decays (we can control the presence of the three body decays varying the branching ratios). We expect the change in N to be small enough to displace the observed upper limits (black lines in Figures 7.1 and 7.2) in the same proportion in the opposite direction, that is, when the number of surviving events increases the signal cross section upper limit decreases in approximately the same ratio. In this way, we can roughly estimate the lower mass exclusion limit for scenarios with three body decays, by finding the mass value at the new intersection.

The analysis we make here is based on a fast simulation using Delphes3 (v3.5.0) [92], unlike the experimental searches, which are based on a full simulation. However, we followed the detector specifications as close as possible as those of the experimental studies. For that, we modified the default Delphes CMS card in such a way that:

- Jets are clustered using the anti-k_T (AKT) algorithm with a radius $R = 0.4$. This is done with FastJet [94, 95].
- Only jets with $p_T > 30$ GeV and $|\eta| < 2.4$ are pre-selected.
- Leptons (electrons or muons) are pre-selected using an isolation requirement. Given a lepton candidate with transverse momentum p_T^l, the lepton isolation variable, I, is defined as the sum of p_T of all the particles inside a cone with a p_T^l-dependent radius around the lepton, divided by p_T^l. The varying isolation radius is defined as:

$$\mathcal{R} = \frac{10 \text{ GeV}}{\min(\max(p_T^l, 50\text{GeV}), 200 \text{ GeV})} \tag{7.6}$$

  We say that a lepton is isolated if $I < 0.1$. For a lepton to be pre-selected, it has to be isolated and satisfy some conditions on kinematical quantities like p_T and η that are specific for each search and will be described in the corresponding Sections 7.3 or 7.4.

For convenience, we define here the H_T^{lep} variable as the scalar p_T sum of all

selected AK4 jets and leptons in the event. This parameter will be often used as an important kinematical cut in the following sections and even in Chapter 8.

7.3 Estimating 3-body decays effect on T searches

As of the writing of this thesis, the latest search for 2/3 charged top partners pair production is the one performed by the CMS Collaboration at CERN for an integrated luminosity of 138 fb^{-1} and a center of mass energy of 13 TeV [40]. This search was made independently for three leptonic signatures: a single lepton (electron or muon) search, a same-sign dilepton channel with exactly two leptons with the same electric charge and a multilepton channel with three or more leptons. The results of these search channels were combined to set a lower limit on the resonance mass for several combinations of its two-body decay branching ratios. The decay channels considered were tZ, th, and Wb. Figure 7.1 shows the experimental results for two scenarios: the singlet scenario (on the left side) with $\mathrm{BR}(W^+b) = 2 \times \mathrm{BR}(th) = 2 \times \mathrm{BR}(tZ) = 0.5$ and the doublet scenario (on the right side) with $\mathrm{BR}(W^+b) = 0$, $\mathrm{BR}(th) = \mathrm{BR}(tZ) = 0.5$. From now on we will refer to these branching ratio configurations as *simplified singlet scenario* and *simplified doublet scenario*, respectively, as they only consider two-body decay channels in their analysis. The plots in Fig 7.1 show a lower limit of around 1.49 TeV (1.5 TeV) for the simplified singlet (doublet) scenario. The maximum mass exclusion for the pair production of vector-like quarks with 2/3 electric charge is 1.54 TeV for resonances with 100% branching ratio into W^+b.

Signal and background events were simulated and signal regions (SR) that favour discrimination of signal against background were defined based on neural networks in the case of the single lepton search channel and on kinematical distributions cuts for the same-sign dilepton and multilepton search channels. Given the complexity of the analyses performed in the single lepton and multilepton channels and our limitations to perform similar analyses, we will only focus in estimating the modifications on the same-sign dilepton channel analysis, leaving the other channels for future work. It is worth mentioning that, from private communication with the authors of [40], we know that the constraint coming from the 2SSL channel alone is much weaker than the combined one (1L+2SSL+multilepton) shown in Figure 7.1.

In the experimental CMS study, the simulation of signal events were made for

T masses in the range [900 GeV, 1800 GeV] with steps of 100 GeV. In our analysis, for each mass in this set, we generate events for the processes $p\bar{p} \to T\bar{T} \to D_1\bar{D}_2$, where D_1 and D_2 can be any of the decay modes th, tZ, Wb and WWt. In total there are 10 decay combinations. The analysis follows the strategy in Section 7.2. The re-scaling of the distributions were done in such a way that the cross section is given by

$$\sigma_{T\bar{T}\to D_1\bar{D}_2} = \sigma_{T\bar{T}} \times F\left[\mathrm{BR}(D_1), \mathrm{BR}(D_2)\right], \tag{7.7}$$

where $\sigma_{T\bar{T}}$ is the T double production cross section and F is defined in Equation 7.2. We will analyze the three branching ratio configurations listed in Table 7.1. The BR configuration in the last scenario was chosen because it is representative of a fourplet-like point in the MCHM$_5$ as can be seen in Figure 6.5.

Scenario	BR(W^+b)	BR(th)	BR(tZ)	BR(W^+W^-t)
Simplified singlet	0.5	0.25	0.25	0
Simplified doublet	0	0.5	0.5	0
Fourplet-like	0	0.45	0.45	0.1

Table 7.1: Scenarios considered in the T analysis and their corresponding branching ratio configurations.

In the 2SSL search channel that we analyze here, we demand exactly two isolated leptons with the same sign of electric charge where the leading lepton has $p_T > 40$ GeV and the sub-leading one, $p_T > 30$ GeV. All leptons must have $|\eta| < 2.4$.

Also, we demand the presence of at least 4 AKT jets. To avoid quarkonia decays, the same-sign lepton pair is required to have an invariant mass greater than 20 GeV. Also, to reject charge-misidentified Z decays, this invariant mass must be outside the range [76.1 GeV, 106.1 GeV]. The CMS search in [40] analyzed the 2017-2018 data and combined it with previous results in [34] with 2016 data. Although different cuts on H_T^{lep} (defined in Section 7.2) were imposed in these studies, we used $H_T^{\mathrm{lep}} > 400$ GeV, which corresponds to the last one, since the 2017-2018 data contains most of the analyzed luminosity and, then, we expect to deviate less from their final results.

In Figure 7.3a we show the number of events passing the SR cuts for each T mass and BR configurations and a luminosity of 138 fb^{-1}. In Figure 7.3b we show the

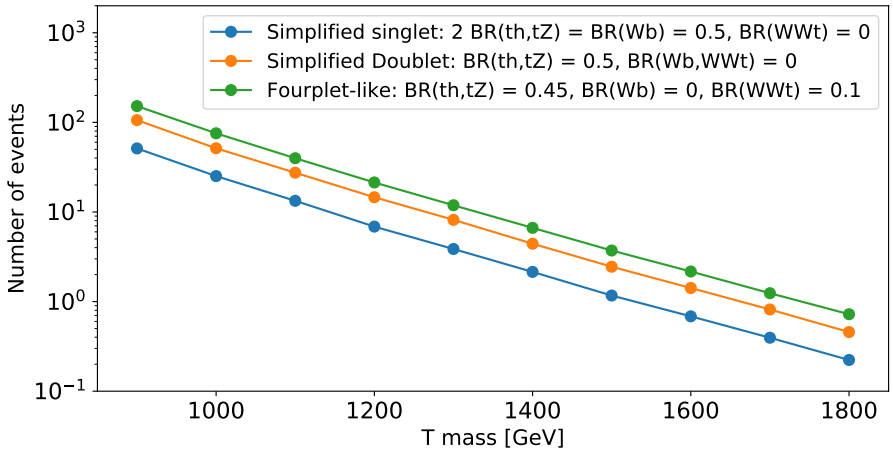

(a) Number of events passing the kinematical cuts described in the main text.

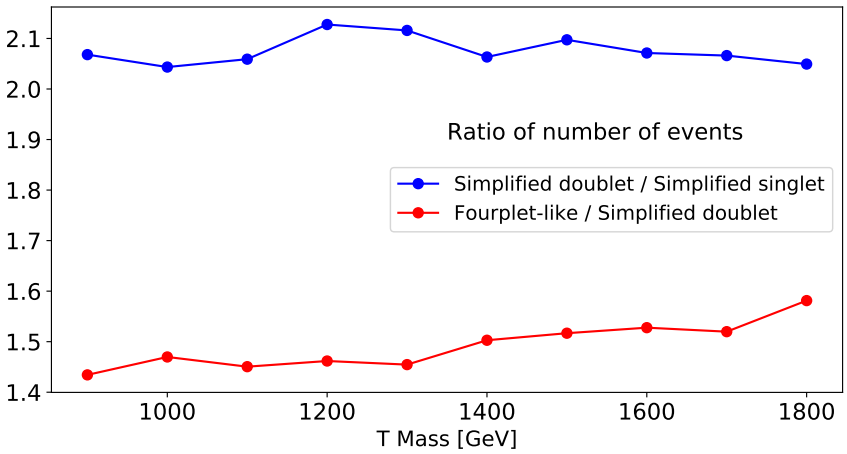

(b) Ratio of the number of events between the fourplet-like and the simplified doublet scenarios (in red) and between the simplified doublet and the simplified singlet scenario (in blue).

Figure 7.3: Results of the T resonances search analysis.

ratio of those numbers of passing events between the fourplet-like and the simplified doublet scenario (in red) and between the simplified doublet and the simplified singlet scenario (in blue). We estimate that those ratios are inversely proportional to the ratios of the cross sections upper limits of the corresponding scenarios found experimentally. To check the validity of this assumption we can compare these ratios for the simplified singlet and doublet scenarios. As is shown by the blue line in Fig. 7.3b the ratio between the number of events in these scenarios (doublet over singlet) varies in the range $[2.04, 2.13]$. Although in [40] they only show the results for the three search channels combined (see Fig. 7.1), we obtained the experimental upper limits for the same-sign dilepton search channel alone through private communication with the authors. By computing the corresponding observed upper limit ratios (singlet over doublet), they are in the range $[1.78, 1.87]$. Therefore, there is a 10%-16% discrepancy with the values we got in our analysis. This difference may indicate a deviation from our approximation, which can be due to the large increase in the number of events (they more than double). Other minor reasons are the random errors introduced by the events simulation, statistical fluctuations in data and some simplifications we did in the cuts implementation. However, for smaller variations in the number of events, we expect our approximation to be more accurate.

Focusing now on the fourplet-like and simplified doublet scenarios in Figure 7.3a and the ratios of their number of events in Figure 7.3b, we can see that the introduction of the 3-body decay channel WWt with branching ratio 0.1 in the fourplet-like scenario increases the number of events with respect to the simplified doublet case in factors lying in the range $[1.42, 1.56]$. That is, even with that low branching ratio of the WWt decay channel, there are enough events coming from the products of this channel surviving the kinematical cuts and enhancing the total number of events. This happens mainly because of the increased probability to find two same sign leptons from direct decays of W bosons as compared to the smaller number of leptons arising from h or Z bosons in the 2-body channels th and tZ respectively. In other words, for this search channel, the factors ξ in Eq. 7.4 for the processes with 3-body decays are larger than the ones with 2-body increasing N^{CUT} in Equation 7.2. Furthermore, we can see that the ratio is increasing with the top partner mass. This is due to the increasing p_T with which the leptons are emitted from heavier resonances allowing them to survive the H_T^{lep} cut more easily.

Following our approximation that the experimental upper limit of the resonance

pair production cross section will decrease in the same proportion (from the simplified doublet to the fourplet-like scenario) as the number of surviving events increase, we can roughly estimate the value that the lower mass exclusion limit would take when considering the 3-body decays. In Figure 7.4 we show the same expected and observed cross section upper limits in Figure 7.1, the simplified singlet scenario in blue and the doublet scenario in red. In purple we show the estimated upper limit for the fourplet-like scenario, obtained by displacing the simplified double dot limits accordingly to the ratios in the Figure 7.3b. Our very rough estimation is that the mass exclusion limit goes up to around 1580 GeV, an increment of ~ 80 GeV with respect to the simplified doublet case. This value is even larger than the maximum experimental lower limit obtained for a point with $\mathrm{BR}(W^+b) = 1$. However, we must be aware that this is a very rough approximation, since Figure 7.1 shows the results for the combination of the three search channels analyzed in [40] (single lepton, two same-sign leptons and at least three leptons) while we are only recasting the analysis for the two same-sign lepton channel. The 3-body decays can have a very different effect on the other two search channels causing this estimation to be inaccurate. A less inaccurate approximation can be found by making the same displacement but for the results of the 2SSL channel alone. From private communication with the authors of [40], we can estimate the mass exclusion limit or maximum reachable mass value to go from ~ 1000 GeV to ~ 1100 GeV, in this case.

7.4 Estimating 3-body decays effect on $X_{5/3}$ searches

In the case of the 5/3-charged top partners, we will follow the analysis made in the latest CMS experimental search for these vector-like resonances at a center of mass of 13 TeV and an integrated luminosity of 35.9 fb^{-1} [39]. In their analysis they considered a unique decay mode of the $X_{5/3}$ resonance into W^+ and t for two types of couplings: a right-handed $X_{5/3}W^+t$ coupling and a left-handed one. A same-sign dilepton final state and a single lepton final state were studied separately and finally combined. The analysis did not find any significant excess over the standard model background and the reported observed lower limits on the mass of the $X_{5/3}$ top partner with right-handed(left-handed) $X_{5/3}W^+t$ coupling are 1.16 (1.10) and 1.32 (1.30) TeV for the same-sign dilepton and single lepton final state, respectively, as can be seen in Fig. 7.2 for the left-handed $X_{5/3}$ at the left part of the figure and the right-handed one at the right part. The combined lower limit on the mass of the $X_{5/3}$ top partner with right-handed (left-handed) $X_{5/3}W^+t$ coupling is 1.33 (1.28)

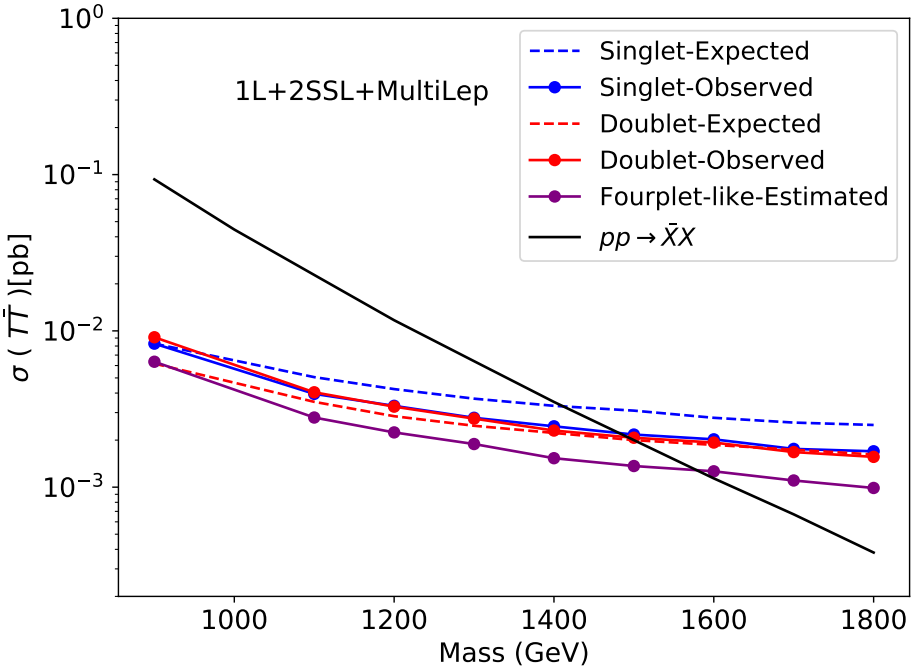

Figure 7.4: Expected and observed upper limits taken from Fig. 7.1 for the simplified singlet (in blue) and simplified doublet (in red) scenarios. The purple line represents the estimated limits in the fourplet- like scenario; 1L+2SSL+MultiLep refers to the results from the 3 corresponding channels analysed in [40].

.

TeV.

In the CMS study, two sets of events were generated: One that only allows right-handed $X_{5/3}$ interactions to W bosons and one that only allows left-handed $X_{5/3}$ interactions to W bosons. However, both scenarios were treated with the same cuts. We are working with a general vector-like $X_{5/3}$, but we expect that applying their cuts still gives a good estimate in our case.

In the CMS study, signal and background events were simulated and SR were defined through several kinematic requirements that enhance signal-background discrimination. Since adding three-body decay channels does not modify the number of background events, we will only focus on analyzing the modifications of the signal events under the SR cuts and how it would affect the estimation of the mass lower limits. We will only focus in estimating the modifications for the same-sign dilepton channel search as the experimental analysis made for the single lepton case is more challenging to reproduce. We leave this later case for a future work.

The simulation of the signal events in [39] was done for resonance masses in the range $[800\ \text{GeV}, 1500\ \text{GeV}]$ in steps of 100 GeV. We follow the analysis strategy described in Section 7.2. For each mass, we generated events for the processes $p\bar{p} \to X_{5/3}\bar{X}_{5/3} \to D_1\bar{D}_2$, where D_1 and D_2 can be any of the decay modes Wt, WtZ and Wth. In total, we have 6 decay combinations for each mass. The analysis was done following the strategy described in Section 7.2. The distributions were re-scaled in such a way that the cross section is given by

$$\sigma_{X\bar{X}\to D_1\bar{D}_2} = \sigma_{X\bar{X}} \times F\left[\text{BR}(D_1), \text{BR}(D_2)\right] \tag{7.8}$$

where $\sigma_{X\ \bar{X}}$ is the cross section of the $X_{5/3}$ pair production and F is a factor that depends on the branching ratios of the channels involved in the process, following Eq. 7.2. We considered the two scenarios listed in Table 7.2 for the branching ratios. The values in the last scenario were chosen to be representative of the parameter space of MCHM_5 as shown in Figure 6.7.

We required events containing two isolated leptons with the same electric charge. Since there can be additional leptons, we define the signal pair as the same-sign lepton pair that maximizes the scalar p_T sum of their constituents. In [39], a different p_T

Scenario	BR(W^+t)	BR(W^+tZ)	BR(W^+th)
2-body	1	0	0
3-body	0.8	0.1	0.1

Table 7.2: Scenarios considered in the $X_{5/3}$ analysis and their corresponding branching ratio configurations.

requirement was set for each of the two different triggering eras in which the samples were collected. However, we will set a unique requirement on the lepton p_T, which simplifies the analysis without significantly affecting the number of accepted events. The leading lepton is required to have $p_T > 40$ GeV and the subleading lepton to have $p_T > 35$ GeV. To avoid quarkonia decays, the same-sign lepton pair invariant mass is taken to be greater than 20 GeV. To reject events with Z boson decays, any event with an opposite charge same flavour lepton pair (electron-electron or muon-muon) with an invariant mass in the range [76.1 GeV, 106.1 GeV] is removed. Also, the event is required to contain at least two AK4 jets with the kinematical cuts outlined before ($p_T > 30$ GeV and $|\eta| < 2.4$).

The number of constituents, N_{const}, is defined as the number of AK4 jets plus the number of leptons not included in the signal lepton pair. Additionally, the CMS study [39] used $N_{\text{const}} \geq 5$ and $H_T^{\text{lep}} > 1200$ GeV, which we are also requiring.

Figure 7.5a shows the number of events that passed the required kinematical cuts at a luminosity of 35.9 fb^{-1}. They are shown for each analyzed $X_{5/3}$ mass and for the two branching ratio scenarios in Table 7.2. The blue circles represent the 2-body scenario and the orange ones, the 3-body scenario. In Figure 7.5b, we can see the ratio between these number of events. Unlike the T search analysis, in this case, there is a small increase of 5% - 10% in the number of accepted events of the 3-body scenario with respect to the 2-body scenario. The reason for this is that, in the case of $X_{5/3}$, the three body decays are introducing either an additional h or Z bosons, which mostly decay into quarks rather than into leptons, making the 2SSL channel less favourable. As a consequence, the lower mass exclusion limit of $X_{5/3}$ is barely affected by the introduction of the 3-body decays in the 2SSL search channel, as we can see in Figure 7.6. There, we show in blue the observed cross section upper limit for a right-handed $X_{5/3} - W - t$ coupling in the 2SSL channel (see Figure 7.2). The purple line represents the estimated 3-body upper limit obtained by displacing it using the proportions in Figure 7.5b. Similar small displacements are found if we

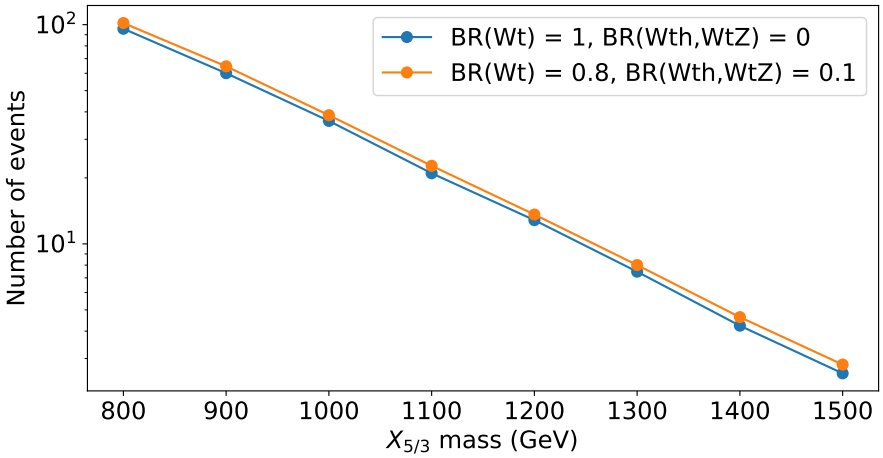

(a) Number of events passing the kinematical cuts described in the main.

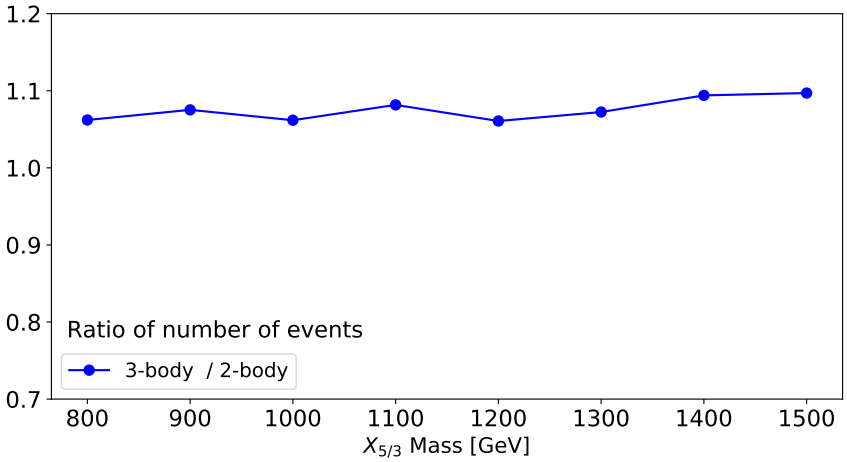

(b) Ratio of the number of events between the 2-body and the 3-body scenarios.

Figure 7.5: Results of the $X_{5/3}$ resonances search analysis.

take as a reference the left-handed $X_{5/3}$ coupling scenario or the combined search channels. We conclude that, at least in this search channel, the introduction of 3-body decays will not affect the exclusion limits significantly. However, other search channels (like the 1L channel) could be affected in a more significant way, which suggests a direction for future investigations.

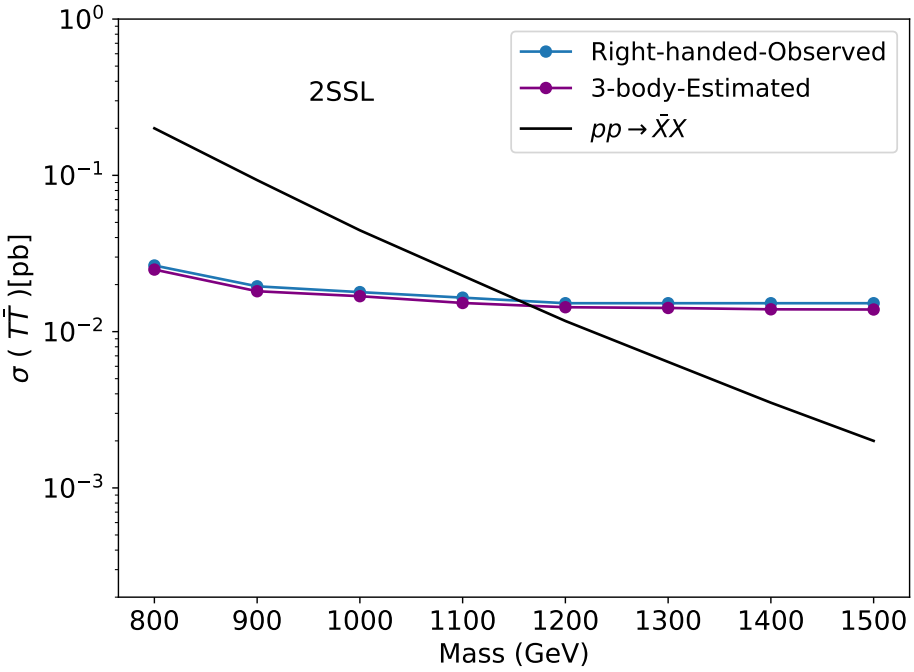

Figure 7.6: Observed upper limits taken from Fig. 7.2 for the right-handed scenario (in blue). The purple line represents the estimated limits considering the right-handed scenario as the reference.

Chapter 8

Search strategy for scenarios with non-negligible 3-body decay channels

In the previous chapter we saw that the presence of three body decays have an impact on the experimental exclusion limits of the resonance mass and we even made a rough estimation of their effect. There we analyzed the modifications on the $X_{5/3}$ and T^1 top partners searches independently. Moreover, in each of those cases, we treated the doubly produced resonances as being on-shell when we used Eq. 7.2. However, if we want to do a complete top partner search analysis involving their pair production and subsequent 3-body decays in the MCHM$_5$, we will see that new off-shell contributions can arise and that the two resonances cannot be studied independently anymore as both $X_{5/3}$ and $T^{(1)}$ pair produced resonances will contribute to the same experimental searches since their final states are similar. Let us show why this is the case.

Let us consider first (for illustration purposes only) the diagrams in Fig. 8.1. These diagrams are only one of the diagrams that contribute to the physical processes that generate the corresponding final states. The full physical process should include all the diagrams in 6.6a (for 8.1a) or 6.3 (for 8.1b). However, the diagrams in Fig. 8.1 have one of the largest contribution to the process in fourplet-like points and will be useful to extract important insights for our study.

In Figure 8.1a, we show the pair production of $X_{5/3}$ with one of them decaying into the 3-body channel W^+tZ mediated by T (which can be any of the three 2/3 charged top partners)[1]. A 3-body decay of the $X_{5/3}$ resonance implicitly assumes that $X_{5/3}$ is on-shell while T is off-shell (if both $X_{5/3}$ and T were on shell, we would have two consecutive 2-body decays: $X_{5/3} \to W^+T$ followed by $T \to tZ$)). However, there is also a probability to have an off-shell $X_{5/3}$ and an on-shell T, in which the

[1]Similar results are obtained if we consider the channel $X_{5/3} \to W^+th$ instead of $X_{5/3} \to W^+tZ$.

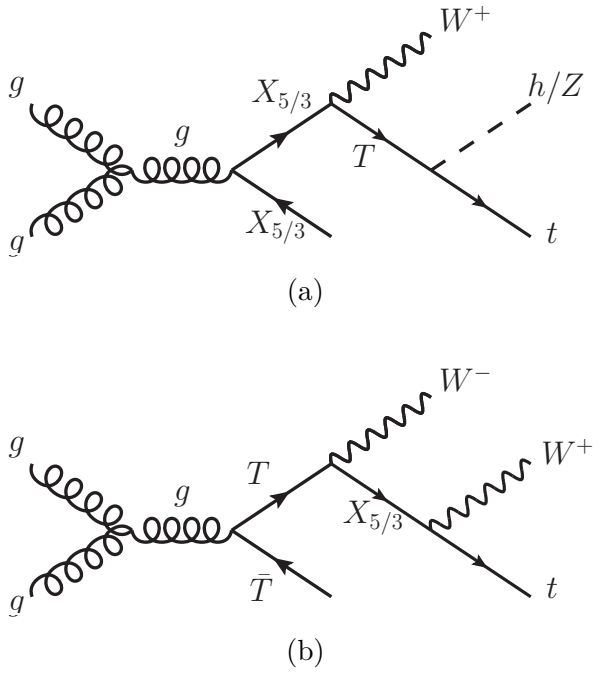

Figure 8.1: Feynman diagrams of the processes involving both two- and tree-body decays of resonances.

diagram represents the production of $W^+T\bar{X}_{5/3}$ mediated by an of-shell $X_{(5/3)}$ with the produced on-shell T decaying into the 2-body channel tZ. The magnitude of each of these contributions will be given by the resonances mass and the couplings involved.

To do a complete analysis we need to consider all of these possibilities. Let us explore how they can arise in detail. In the MCHM$_5$ we can have two types of lightest states: a singlet-like and a fourplet-like. Let us study each of these cases:

- For a singlet-like point, the mass of the lightest T resonance is given approximately by $M_T \approx \sqrt{M_1^2 + y_R^2 f^2}$. Recalling that $M_{X_{5/3}} \approx M_4$, we have that $M_{X_{5/3}} > M_T + M_W$ holds for a large enough M_4. That is, there is enough phase space for the on-shell $X_{5/3}$ to decay into the 2-body channel W^+T. The on-shell T can, in turn, decay into tZ (or tH). Having the two resonances on-shell could make the singlet-like T to be the most important contributor to the whole process. However, the vertex $X_{5/3-T-W^+}$, in this case, is suppressed since the resonances belong to different multiplets. Therefore, this process will be more suppressed the more purely singlet T is.

- In a fourplet-like point, $X_{5/3}$ and the lightest T belong to the same doublet and, hence, they have a degenerate mass approximately equal to M_4, with

the difference between them being less than M_W. That means that both resonances cannot be on-shell at the same time. However, one of them can be on-shell while the other is off-shell. The physical process will have both contributions as we can see in Figure 8.2. There, we show the normalized invariant mass distributions of two combination of final states from the process in Figure 8.1a for the C_9 benchmark point, that we take as representative of a fourplet-like point. At the top, we can see the distribution of $\mathrm{M}[W^+, t, Z]$, the invariant mass of the 3-body decay products of $X_{5/3}$. There we can see a peak at approximately 1300 GeV and a continuous bump right after it. The peak corresponds to the on-shell contribution of $X_{5/3}$ and the bump to the on-shell contribution of the T resonance. The bump starts appearing at approximately the peak mass because $X_{5/3}$ and T are degenerate in mass. For a heavier T mass resonance, for instance, the bump would start appearing more to the right. This is because an on-shell T would, at least, produce a $\mathrm{M}[t, Z]$ equal to its own mass (for a W^+ emitted with $p_T = 0$). At the bottom of Figure 8.2 we can see the distribution of the invariant mass of the tZ combination. In this case, the peak at around 1300 GeV corresponds to the on-shell contribution of T. The bump at the left of the peak represents the on-shell contribution of $X_{5/3}$. The maximum value of the bump is the $X_{5/3}$ mass which corresponds to the case in which the W^+ is emitted with $p_T = 0$. So, we can see that, for a fourplet-like point of the MCHM_5, both contributions overlap and have to be considered jointly.

In Figure 8.1b we show the Feynman diagram that represents the pair production of a T resonance with one of them decaying into the 3-body decay channel W^+W^-t with a $X_{5/3}$ resonance as mediator. Similarly to the previous case, this diagram can also represent the production of an on-shell $X_{5/3}$ (in association with a $\bar{T}$ and a W^-) decaying into the 2-body channel W^+t. Let us explore this process for the two realizations that the lightest T resonances can take:

- When the lightest T is a singlet-like resonance this process is highly suppressed as the resonances belong to different multiplets, however, we will still study their distributions as they can be useful to understand their fourplet-like counterparts. In a singlet-like point, the $X_{5/3}$ mass is greater than the T mass for a large enough M_4. That means that both resonances cannot be on-shell simultaneously. However, either one of them can be on-shell while the other is off-shell. These two contributions can be clearly seen represented by the blue

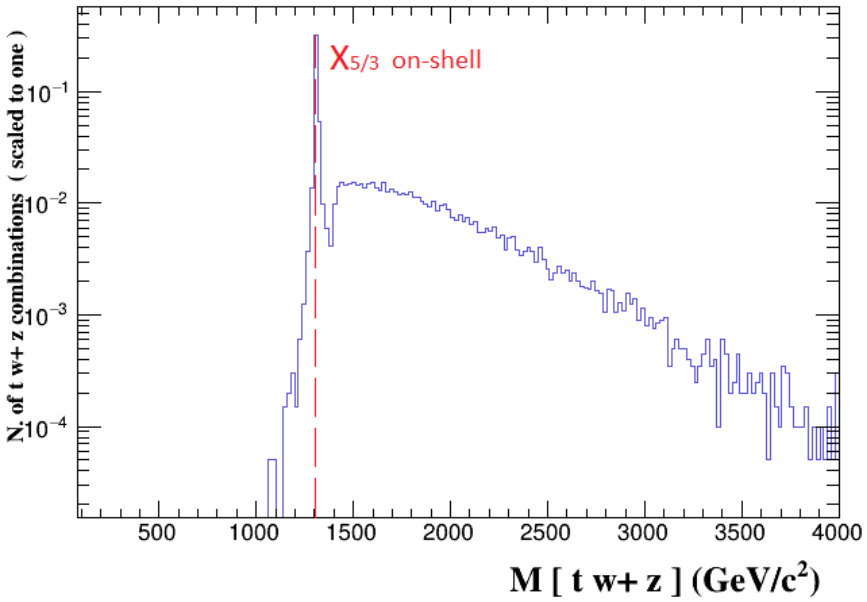

(a) M$[W^+, t, Z]$ distribution.

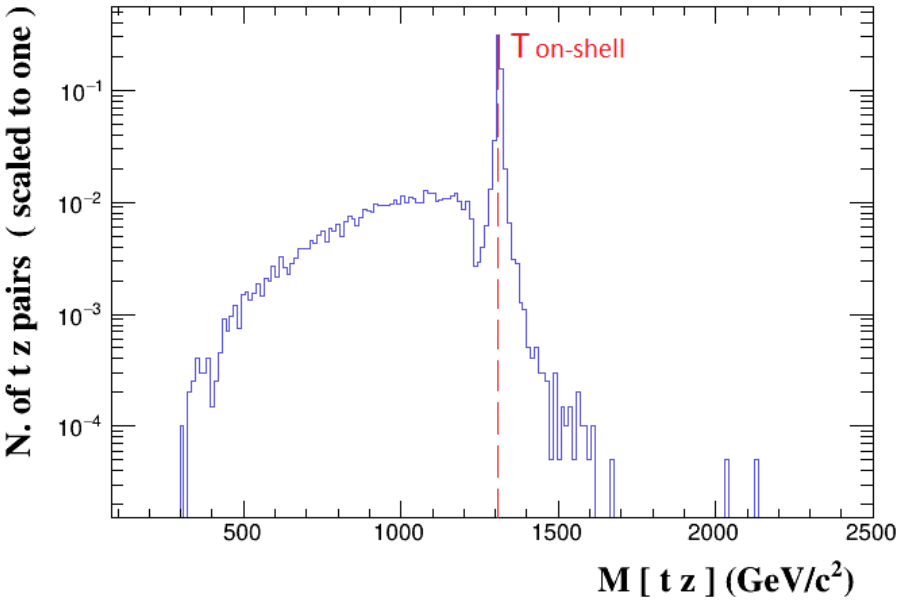

(b) M$[t, Z]$ distribution.

Figure 8.2: Invariant mass distributions of the process in Figure 8.1a for the benchmark point C_9 (fourplet-like point). Histograms generated with MadAnalysis 5 [75].

lines in Figure8.3, which show two invariant mass distributions (normalized to one) for the singlet-like point C_3 and the process in Figure 8.1b. At the top, we can see the $M[W^+, W^- t]$ distribution that shows the presence of a peak at around 1.6 TeV, that corresponds to the on-shell mass of the lightest T, and a bump starting at around 2.2 TeV (the mass of $X_{5/3}$) that corresponds to the $X_{5/3}$ on-shell contribution. In this case, the peak and the bump are clearly distinguishable because of the difference in mass between the lightest T and $X_{5/3}$. The blue line in Figure 8.3b shows the distribution of the invariant mass $M[W^+, t]$ for the same point C_3. Here, also, both contributions are clearly distinguishable with the peak at around 2.2 TeV representing the on-shell contribution of $X_{5/3}$ and the bump at the left, the T on-shell contribution that goes up to around 1.6 TeV (The lightest T mass) when a W^- is emitted at rest.

- When the lightest T is a fourplet-like resonance, it forms a doublet with $X_{5/3}$. Then, their masses are approximately degenerate and they can not be on-shell simultaneously. However, one of them can be on-shell while the other is off-shell. In Figure 8.3, we show in red, two normalized distributions for the fourplet-like point C_9. There we can see both contributions but, unlike the singlet-like case, they overlap due to the mass degeneracy between $T^{(1)}$ and $X_{5/3}$. We saw a similar behaviour in the distributions of Figure 8.2.

As we see, it is not an easy task to split the on-shell contributions for a fourplet-like point in processes where both $X_{5/3}$ and T resonances are present in the same diagram. On the other hand, in the singlet-like points, although it would be easier to split the on-shell contributions, they are negligible compared to other diagrams that contributes to the 3-body decay channels.

8.1 Detailed phenomenological analysis on a showcase MCHM$_5$ point

In Chapter 7 we followed the analyses made in the experimental top partner searches, which assume simplified scenarios in which there is only one light resonance (T or $X_{5/3}$) while others are considered heavy enough to be integrated out. Also, they only considered these resonances to decay into 2-body channels. However, we saw that, in the MCHM$_5$, the existence of 3-body decay channels implies considering

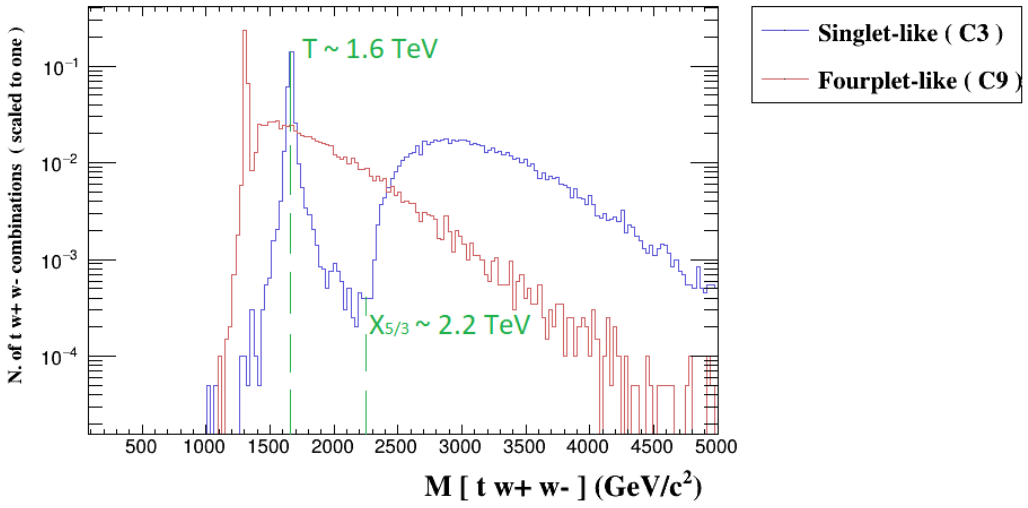

(a) M$[W^+, W^-, t]$ distribution.

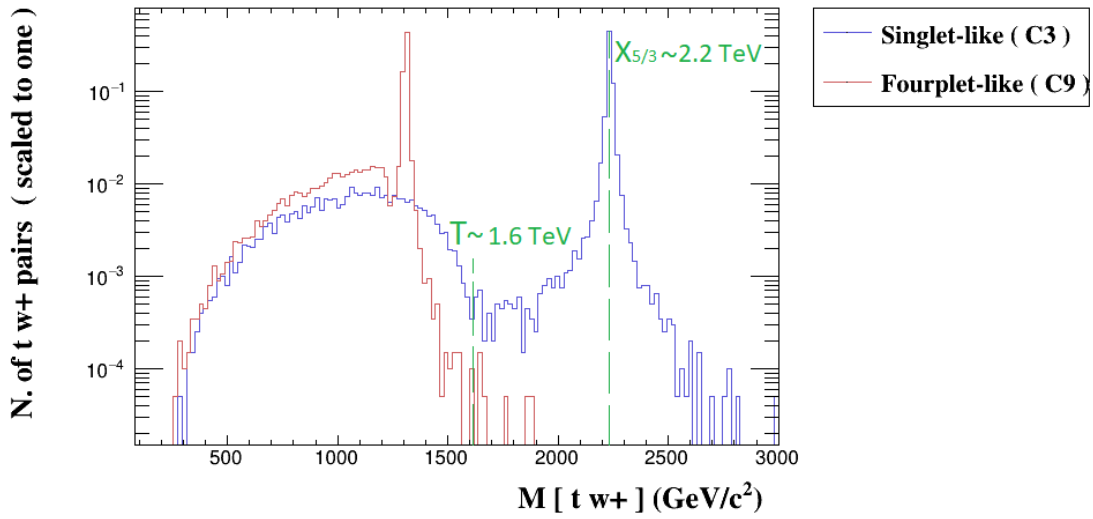

(b) M$[W^+, t]$ distribution.

Figure 8.3: Normalized invariant mass distributions of the process in Figure 8.1b for the benchmark points C_3 and C_9. Histograms generated with MadAnalysis 5 [75].

processes where more than one resonance is present. Moreover, these processes are more relevant in cases with mass degeneracy. An important case of degeneracy in our analysis is the one between the lightest T and $X_{5/3}$ in a fourplet-like scenario, which involves the overlap between their on-shell contributions in processes where both are present.

Here, we present a complete analysis for a representative MCHM$_5$ fourplet-like point including all resonances and contributions arising from the 3-body decays in the multileptonic search channels. At the time of the elaboration of this analysis, the most recent pair produced top partner searches including a two same-sign lepton (2SSL) channel were [39] for the $X_{5/3}$ search and [96] for the T search. The reported mass lower bounds in those studies were around 1.3 TeV for both resonances. We chose to do the analysis on the benchmark point C_9 in Table 4.5 since its $X_{5/3}$ and lightest T masses are nearly degenerate and borderline with respect to that limit. Also, the mass of the second lightest 2/3 charged top partner (1.8 TeV) is low enough so that it is not integrated out and can contribute to increase the signal events. More importantly, $T^{(1)}$ has a sizable branching ratio into three bodies making it an unexplored scenario in current searches. In Table 8.1 we show the main properties of the 5 resonances in the C_9 point [2].

8.1.1 Signal

Since we have seen that 3-body decays of the $T^{(1)}$ resonance increase the resistance to cuts in the leptonic channels, we will focus in a signal containing the decay $T^{(1)} \to W^+W^-t$. Specifically, we will focus on the $T^{(1)}$ pair production where one resonance decays into a 2-body state (th or tZ) and the other into the 3-body one (WWt). In turn the top quarks decay into Wb and we will consider h/Z to decay into $b\bar{b}$ to maximize the number of events, which give rise to $W^+W^-W^+W^-b\bar{b}b\bar{b}$ ($4W4b$). This same configuration can be obtained from the pair production of the $X_{5/3}$ resonance with one of them decaying into the 3-body channel WtZ or Wth and the other into the 2-body channel Wt. Therefore, we must consider both processes [3].

[2] Here, we are computing the widths including all possible partial decays. The value $\Gamma_{T^{(1)}} = 7.75$ GeV is, thus, a bit higher than the one showed in Table 4.5 ($\Gamma_{T^{(1)}} = 7.49$ GeV), because, there, we used the "automatic" Madgraph tool, which compute widths ignoring some small partial decay for computational efficiency.

[3] Although we are mentioning only the on-shell 3-body decay, we are implicitly including the off-shell contributions, as well.

	$T^{(1)}$	$T^{(2)}$	$T^{(3)}$	B	$X_{5/3}$
Mass (GeV)	1312	1804	2024	1987	1309
Width (GeV)	7.75	13.38	6.8	5.5	6.68
Pair production σ (fb)	6.60	0.50	0.17	0.21	6.74
BR(th)	0.456	0.162	0.032	-	-
BR(tZ)	0.395	0.07	0.14	-	-
BR(W^+b)	0.016	0.204	0.135	-	-
BR(W^-t)	-	-	-	0.045	-
BR(W^+t)	-	-	-	-	0.855
BR(W^+W^-t)	0.097	0.124	0.009	-	-
BR(W^+tZ)	-	-	-	-	0.025
BR(W^+ht)	-	-	-	-	0.025
BR($X_{5/3}W^-$)	-	0.128	0.014	-	-
BR($T^{(1)}h$)	-	0.066	0.006	-	-
BR($T^{(1)}Z$)	-	0.062	0.006	-	-
BR($T^{(2)}h$)	-	-	0.179	-	-
BR($T^{(2)}Z$)	-	-	0.421	-	-
BR($W^-T^{(1)}$)	-	-	-	0.007	-
BR($W^-T^{(2)}$)	-	-	-	0.765	-
Other BRs	0.037	0.18	0.058	0.19	0.095

Table 8.1: Masses, decay widths and branching ratios of the resonances in the benchmark point C_9.

Subsequently, there can be different final states depending on the decay mode of the W bosons (which can be either leptonic or hadronic). In this study we chose to focus in multileptonic search channels which, despite their low cross section due to the low branching ratio of the leptonic W decay, are a cleaner signature as compared to the fully-hadronic or mono-leptonic channels, as the last ones present large backgrounds. We will perform dedicated analysis for two multileptonic channels: The two same-sign leptonic (2SSL) channel, in which only events with exactly a pair of leptons (electrons or muons) with the same electric charge are considered, and the trilepton (3L) channel, in which exactly three leptons (electrons or muons) of any charge are required. Additionally, we will do an analysis for a 2SSL+3L search channel in which events with two same-sign lepton or three leptons are required. To perform an inclusive search, we will consider as signal events the ones arising from all processes involving top partners that can contribute to the search channels.

Process	σ [fb]	decay mode	$\sigma \times$ BR [ab]
$X\bar{X} \to t\bar{t}W^+W^-$	4.87	$W_{l^\pm}W_{l^\pm}W_{\rm had}W_{\rm had}$	208
		$W_{l^\pm}W_{l^\mp}W_{l^\pm}W_{\rm had}$	133
		$W_{l^\pm}W_{l^\mp}W_{l^\pm}W_{l^\mp}$	106
$X\bar{X} \to W^+W^-t\bar{t}h$	1.12	$W_{l^\pm}W_{l^\pm}W_{\rm had}W_{\rm had}$	27.6
		$W_{l^\pm}W_{l^\mp}W_{l^\pm}W_{\rm had}$	17.7
		$W_{l^\pm}W_{l^\mp}W_{l^\pm}W_{l^\mp}$	1.41
$T\bar{T} \to W^+W^-t\bar{t}h$	1.01	$W_{l^\pm}W_{l^\pm}W_{\rm had}W_{\rm had}$	24.9
		$W_{l^\pm}W_{l^\mp}W_{l^\pm}W_{\rm had}$	15.9
		$W_{l^\pm}W_{l^\mp}W_{l^\pm}W_{l^\mp}$	1.27
$T\bar{T} \to t\bar{t}hh$	1.37	$W_{l^\pm}W_{l^\pm}W_{\rm had}W_{\rm had}$	14.6
		$W_{l^\pm}W_{l^\mp}W_{l^\pm}W_{\rm had}$	9.32
		$W_{l^\pm}W_{l^\mp}W_{l^\pm}W_{l^\mp}$	0.75
$X\bar{X} \to W^+W^-t\bar{t}Z$	1.1	$W_{l^\pm}W_{l^\pm}W_{\rm had}W_{\rm had}$	7.15
		$W_{l^\pm}W_{l^\mp}W_{l^\pm}W_{\rm had}$	4.58
		$W_{l^\pm}W_{l^\mp}W_{l^\pm}W_{l^\mp}$	3.66
$T\bar{T} \to W^+W^-t\bar{t}Z$	0.86	$W_{l^\pm}W_{l^\pm}W_{\rm had}W_{\rm had}$	5.59
		$W_{l^\pm}W_{l^\mp}W_{l^\pm}W_{\rm had}$	3.57
		$W_{l^\pm}W_{l^\mp}W_{l^\pm}W_{l^\mp}$	0.29
$T\bar{T} \to t\bar{t}Zh$	2.37	$W_{l^\pm}W_{l^\mp}W_{\rm had}Z_l$	4.29
		$W_{l^\pm}W_{l^\pm}W_{\rm had}W_{\rm had}$	3.33
		$W_{l^\pm}W_{l^\mp}W_{l^\pm}W_{\rm had}$	2.13
		$W_{l^\pm}W_{l^\mp}W_{l^\pm}W_{l^\mp}$	0.17
$T\bar{T} \to t\bar{t}ZZ$	1.03	$W_{l^\pm}W_{l^\mp}Z_l$	0.98

Table 8.2: Signal processes for the point C_9 in the 2SSL search at LO and $\sqrt{s} = 14$ TeV.

In Table 8.2 we list (in the first column) the signal processes used in the analyses. The signal processes are composed by the pair production of T or X with all the possible decay combinations into two or three bodies with the exception of the ones containing both resonances decaying into three bodies due to their negligible cross section. The second column shows their corresponding cross sections at $\sqrt{s} = 14$ TeV before any leptonic or hadronic decay. The third column shows the decay modes that contribute the most to our desired signatures. For the case of the W boson, $W_{l^\pm}$ or $W_{l^\mp}$ represent their leptonic decay mode (into electrons or muons) and W_{had}, their hadronic decay mode. Z_l represent the leptonic decay (into electrons or muons) of the Z boson. The fourth column lists the cross sections after the decays. These were computed by multiplying the cross section by the corresponding branching ratios. All processes were simulated with Madgraph5 (v2.9) [74] at LO. Showering and hadronization were performed by Pythia8 [91] and the events were passed through Delphes3 (v3.5.0) [92] for a fast detector analysis. At Delphes level, we used the default card for the HL-LHC and we used FastJet [94, 95] to cluster jets using the anti-k_T algorithm with $R = 0.4$.

One can think that the cross sections of all processes (before the decays of Ws) in table 8.2 can be approximated by the product of the corresponding pair production cross sections and the branching ratios into 2- and 3-body channels listed in 8.1. However, this is true only for the processes containing 2-body decays, exclusively. For the ones containing 3-body decays, the cross sections are larger (around four times) than just the corresponding product. This is because, for these cases, besides the pure 3-body decay of the on-shell pair produced resonances, there is the additional contribution of the off-shell counterpart, as discussed previously.

8.1.2 Background

The $4W4b$ signature of the signal events is also produced by the SM production of four top quarks. We will take advantage of the fact that this process has been the subject of intensive dedicated searches [97, 98, 99] and consider it and its usual backgrounds as the background processes for our analysis. The $t\bar{t}t\bar{t}$ backgrounds are usually categorised into two types: irreducible, composed of the processes in which the selected leptons come from decays of W or Z bosons, and the reducible background, which is composed of processes in which misidentified leptons can fake the signal signature. These mis-identifications can be produced either because of

misassigned electric charge of prompt leptons or fake/non-prompt leptons arising from the decay of a heavy meson.

Among the irreducible background processes, the most important is the production of $t\bar{t}$ in association with a boson, that is, $t\bar{t}W$, $t\bar{t}Z$ or $t\bar{t}h$. Other minor contributors are the top pair production in association with two bosons, that is $t\bar{t}W^+W^-$, $t\bar{t}hh$, $t\bar{t}ZZ$, $t\bar{t}hZ$. However, we will not include the processes containing Z or h bosons since, either the branching ratio into leptons is small (in the case of the Z's), or they have to first decay into W's to finally produce leptons (in the case of h) making them to have a safely negligible contribution. The $t\bar{t}W^+W^-$ process, on the other hand, can decay directly into the desired final states and will be considered. In Table 8.3 we list, in the first column, all the considered irreducible background processes with their cross section at LO and $\sqrt{s} = 14$ in the second column. The third column shows the decay modes that contribute to our search channel and the fourth the cross sections after these decays. The "jets" term in $t\bar{t}W^{\pm}$ + jets and $t\bar{t}Z$ + jets represent the respective process plus 0, 1 and 2 jets. For these processes, the final jets after parton shower were matched to the original partons using the MLM matching scheme. The processes in Table 8.3 will be used in all three search channels.

Backgrounds	σ [fb]	decay mode	$\sigma \times$ BR [fb]
$t\bar{t}W^{\pm}$ + jets	574.5	$W_{l^\pm}W_{l^\pm}W_{\text{had}}$	18.14
		$W_{l^\pm}W_{l^\pm}W_{l^\mp}$	5.81
$t\bar{t}Z$ + jets	743.1	$W_{l^\pm}W_{\text{had}}Z_l$	12.73
		$W_{l^\pm}W_{l^\mp}Z_l$	2.04
$t\bar{t}h$	479.9	$W_{l^\pm}W_{\text{had}}W_{l^\pm}W_{\text{had}}$	4.42
		$W_{l^\pm}W_{l^\mp}W_{l^\pm}W_{\text{had}}$	2.82
		$W_{l^\pm}W_{\text{had}}Z_lZ_{\text{had}}$	0.54
		$W_{l^\pm}W_{l^\mp}W_{l^\pm}W_{l^\mp}$	0.22
$t\bar{t}t\bar{t}$	11.8	$W_{l^\pm}W_{l^\pm}W_{\text{had}}W_{\text{had}}$	0.51
		$W_{l^\pm}W_{l^\mp}W_{l^\pm}W_{\text{had}}$	0.32
		$W_{l^\pm}W_{l^\mp}W_{l^\pm}W_{l^\mp}$	0.03
$t\bar{t}W^+W^-$	9.88	$W_{l^\pm}W_{\text{had}}W_{l^\pm}W_{\text{had}}$	0.42
		$W_{l^\pm}W_{l^\mp}W_{l^\pm}W_{\text{had}}$	0.27
		$W_{l^\pm}W_{l^\mp}W_{l^\pm}W_{l^\mp}$	0.03
tZ bjj	317	$W_{l^\pm}Z_l$	4.6

Table 8.3: Most important background processes contributing to the 2SSL, 3L or 2SSL+3L channels. The cross sections were computed at LO and $\sqrt{s} = 14$ TeV.

We are neglecting the irreducible background $t\bar{t}$ + jets, despite it having a larger

cross section before cuts due to computational limitations. However, the cuts we will impose in the analysis are hard enough to safely neglect it.

8.1.3 Analysis strategy

Once the signal and background samples were generated, they were passed through Delphes3 to simulate the response of the HL-LHC detectors. For that, we used the default card corresponding to this detector configuration. The b-jet reconstruction algorithm has an efficiency of $0.75(1 - \frac{p_T}{5000\ \text{GeV}})$. Given a lepton candidate with transverse momentum p_T^l, it is considered to be isolated if the p_T sum of all the particles inside the cone with fixed radius $\mathcal{R} = 0.3$ around the lepton, divided by p_T^l, is less than 0.1. Additionally, we imposed the following conditions on the accepted reconstructed particles: leptons (electrons or muons) with $p_T > 30$ GeV and $|\eta| < 3$ and jets with $p_T > 30$ GeV and $|\eta| < 3$.

As we mentioned before, the signal processes involving 3-body decays have 4 b-jets in their final state, which arise from the hadronic decay of the Higgs or Z bosons and from the electroweak decay of tops. From all the background processes, only the four tops production presents this same feature at the matrix element (ME) level. Thus, the b-jet multiplicity is another important signal/background discriminator. We kept only the events with three or more reconstructed b-jets ($N_b \geq 3$). This cut will be used in all three search channels (2SSL, 3L and 2SSL+3L).

The decays of the pair produced resonances in the signal processes produce highly energetic particles. Although we could use the leptons' p_T sum or the jets' p_T sum as good discriminators, separately, we found that the variable H_T^{lep} (defined in Section 7.2) is an even better discriminator. In Figure 8.4 we show the H_T^{lep} distribution of all the processes involved, when selecting only the events with exactly two leptons with the same electric charge (2SSL channel). The black line represents the sum of all the events arising from the signal processes in Table 8.2. The background processes are shown as stacked histograms. As we can see, the signal H_T^{lep} takes high values as compared to the background counterpart. We use this variable as an important cut to enhance the signal/background ratio. We experimented with different H_T^{lep} cuts in each search channel and chose the following values as the best ones: $H_T^{\text{lep}} > 1.8$ TeV for the 2SSL channel, $H_T^{\text{lep}} > 1.6$ TeV for the 3L channel and $H_T^{\text{lep}} > 1.6$ for the 2SSL+3L channel.

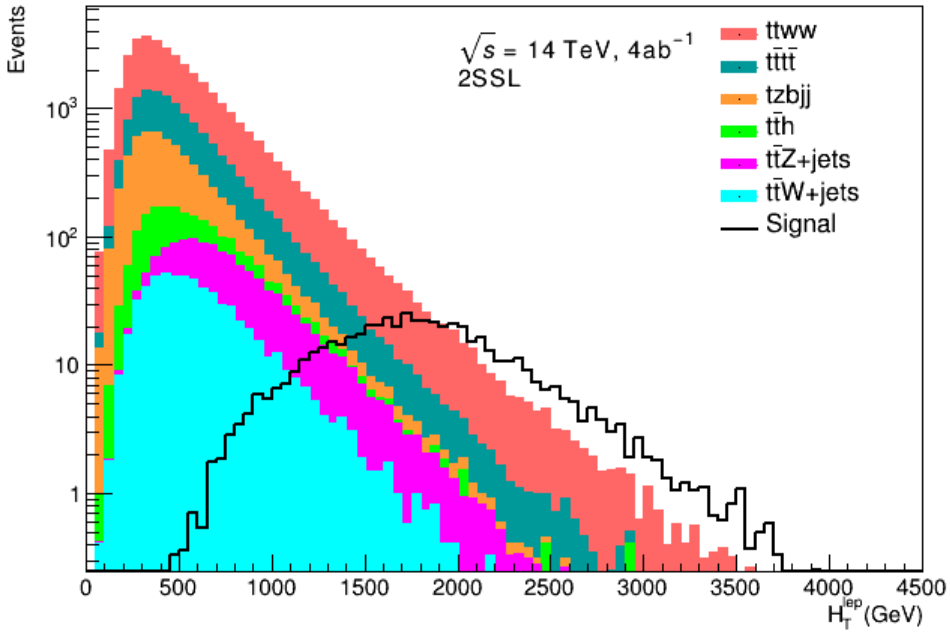

Figure 8.4: H_T^{lep} distribution in the 2SSL channel.

We also impose cuts on the missing energy ($\not{E}_T$) to help ensure we are excluding the contributions of the reducible backgrounds and other rarer processes like double boson production (WZ, ZZ, $W^{\pm}W^{\mp}$). The chosen minimum values of $\not{E}_T$ are: 100 GeV for the 2SSL channel, 150 GeV for the 3L channel, and 100 or 150 GeV for the 2SSL+3L channel depending on the desired degree of rare background exclusion.

8.1.4 Results

In Tables 8.4, 8.5 and 8.6, we list the number of events at a luminosity $\mathcal{L} = 4\text{ab}^{-1}$ after each step of the cuts implementations for both signal and background processes in the 2SSL, 3L and 2SSL+3L search channels, respectively. These values are rounded to the nearest integer.

We can see that the first two cuts (N_b and H_T^{lep}) are the most important ones to enhance the signal-to-background ratio (S/B) and the signal significance ($S/\sqrt{B}$). After these two cuts these values are, respectively: 2.2 and 11.9 for the 2SSL channel, 2.1 and 9.0 for the 3L channel, and 1.7 and 14.5 for the 2SSL+3L channel. These results show us that it is posible to find evidence for this model at the HL-LHC

in these kind of inclusive searches. We can further use the missing energy cut to ensure reducing rare backgrounds even if we slightly reduce the number of signal events. With the listed cuts $S/\sqrt{B}$ shows a slight increase in all three search channels.

From the three studied channels, the most promising one is the 2SSL + 3L both because of the highest value of $S/\sqrt{B} = 14.5$ getting up to $S/\sqrt{B} = 15$ with the $\not{E}_T$ cut implementation and because of the higher number of signal events. Although we are considering a model with resonance masses around 1.3 TeV, we can roughly estimate the mass reach of the HL-LHC. For this, we can assume that the signal cross section (or, directly, the number of events) is proportional to the resonance pair production cross section, which decreases exponentially with mass as shown by the black line in Figure 7.6. In this way, and assuming a luminosity of 4 ab^{-1}, the estimated mass that it is possible to reach at the HL-LHC is around 1.5 TeV for $S/\sqrt{B} = 5$ and 1.6 TeV for $S/\sqrt{B} = 3$. These mass reaches were obtained following a simple cut-and-count analysis, with only two multileptonic channels. A more complete analysis would surely enhance them.

It is worth noticing that, among the signal processes, the ones containing three body decays survive the cuts better and even overtakes the number of events of the ones with only two body decays. This happens despite the small 3-body decay branching ratios of both T and $X_{5/3}$ resonances, mainly because of the low cost to produce leptons as they come directly from the W bosons, while in the 2-body processes, production of leptons needs to pass first through $h \to WW^*$ or the direct Z leptonic decay ($Z \to l^+l^-$) which has a smaller branching ratio.

Process			Number of events - 2SSL ($\mathcal{L} = 4$ ab^{-1})			
			No cuts	$N_b \geq 3$	$N_b \geq 3$, $H_T^{\text{lep}} > 1.8$ TeV	$N_b \geq 3$, $H_T^{\text{lep}} > 1.8$ TeV $\not{E}_T > 150$ GeV
Signal	2-bodies	$X\bar{X} \to t\bar{t}W^+W^-$	356	40	20	15
		$T\bar{T} \to t\bar{t}hh$	39	14	5	3
		$T\bar{T} \to t\bar{t}Zh$	17	7	4	2
		$T\bar{T} \to t\bar{t}ZZ$	12	2	1	1
	3-bodies	$X\bar{X} \to W^+W^-t\bar{t}h$	48	24	15	11
		$T\bar{T} \to W^+W^-t\bar{t}h$	42	21	13	9
		$T\bar{T} \to W^+W^-t\bar{t}Z$	15	6	4	3
		$X\bar{X} \to W^+W^-t\bar{t}Z$	12	5	3	2
Background		$t\bar{t}W^\pm$	20536	691	19	9
		$t\bar{t}Z$	7062	237	4	2
		$t\bar{t}h$	3893	132	1	0
		$t\bar{t}t\bar{t}$	658	288	6	3
		$t\bar{t}W^+W^-$	597	30	1	0
		tZ bjj	761	18	0	0
S/B				0.1	2.2	3.2
$S/\sqrt{B}$				3.2	11.9	12.1

Table 8.4: Number of events surviving the cuts implementation in the 2SSL search channel.

Process			Number of events - 3L ($\mathcal{L} = 4$ ab^{-1})			
			No cuts	$N_b \geq 3$	$N_b \geq 3$, $H_T^{\text{lep}} > 1.6$ TeV	$N_b \geq 3$, $H_T^{\text{lep}} > 1.6$ TeV $\not{E}_T > 100$ GeV
Signal	2-bodies	$X\bar{X} \to t\bar{t}W^+W^-$	137	9	5	4
		$T\bar{T} \to t\bar{t}hh$	19	5	3	2
		$T\bar{T} \to t\bar{t}Zh$	35	16	13	11
		$T\bar{T} \to t\bar{t}ZZ$	49	7	6	5
	3-bodies	$X\bar{X} \to W^+W^-t\bar{t}h$	18	8	5	5
		$T\bar{T} \to W^+W^-t\bar{t}h$	15	7	5	4
		$T\bar{T} \to W^+W^-t\bar{t}Z$	5	2	1	1
		$X\bar{X} \to W^+W^-t\bar{t}Z$	4	2	1	1
Background		$t\bar{t}W^\pm$	3203	44	2	2
		$t\bar{t}Z$	10444	308	13	8
		$t\bar{t}h$	1280	26	0	0
		$t\bar{t}t\bar{t}$	201	79	3	2
		$t\bar{t}W^+W^-$	197	6	0	0
		tZ bjj	984	21	1	1
S/B				0.1	2.1	2.6
$S/\sqrt{B}$				2.5	9.0	9.3

Table 8.5: Number of events surviving the cuts implementation in the 3L search channel.

Process			Number of events - 2SSL+3L ($\mathcal{L} = 4$ ab^{-1})				
			No cuts	$N_b \geq 3$	$N_b \geq 3$, $H_T^{\text{lep}} > 1.6$ TeV	$N_b \geq 3$, $H_T^{\text{lep}} > 1.6$ TeV $\not{E}_T > 100$ GeV	$N_b \geq 3$, $H_T^{\text{lep}} > 1.6$ TeV $\not{E}_T > 150$ GeV
Signal	2-bodies	$X\bar{X} \to t\bar{t}W^+W^-$	492	49	32	28	24
		$T\bar{T} \to t\bar{t}hh$	58	19	10	8	7
		$T\bar{T} \to t\bar{t}Zh$	52	23	18	14	11
		$T\bar{T} \to t\bar{t}ZZ$	60	9	7	6	4
	3-bodies	$X\bar{X} \to W^+W^-t\bar{t}h$	66	32	24	20	17
		$T\bar{T} \to W^+W^-t\bar{t}h$	57	27	21	18	15
		$T\bar{T} \to W^+W^-t\bar{t}Z$	20	8	6	5	4
		$X\bar{X} \to W^+W^-t\bar{t}Z$	16	7	5	4	4
Background		$t\bar{t}W^\pm$	23739	735	35	24	16
		$t\bar{t}Z$	17506	545	20	12	8
		$t\bar{t}h$	5174	158	1	1	1
		$t\bar{t}t\bar{t}$	859	367	14	10	7
		$t\bar{t}W^+W^-$	794	36	1	1	1
		tZ bjj	1744	39	1	1	0
S/B				0.1	1.7	2.1	2.6
$S/\sqrt{B}$				4.0	14.5	14.9	15.0

Table 8.6: Number of events surviving the cuts implementation in the 2SSL+3L search channel.

Chapter 9

Conclusions and Outlook

This thesis explored Minimal Composite Higgs Models at high energy hadron colliders. In particular, we focused on the MCHM_5 and the MCHM_{14}, for which we developed full generation and simulation frameworks to study their parameter space.

In Chapters 3 to 5, we concentrated on the $t\bar{t}h$ and $t\bar{t}hh$ production processes. The $t\bar{t}h$ process kinematic distributions are not modified with respect to the SM but deviations in the cross section can occur. While it is always suppressed in the MCHM_5, the cross section can be enhanced in the MCHM_{14}, as expected. Regarding the $t\bar{t}hh$ process, both non-resonant contributions and heavy top partners pair production were included. The study finds that the non-resonant contribution is sizable, and even dominant for heavy fermion masses over 4 TeV, and provides access not only to the trilinear Higgs self-coupling (as in the SM), but also to the double Yukawa coupling introduced by the MCHM. The analysis also examined the relative contributions of the top-Yukawa, double Yukawa, and trilinear Higgs couplings, revealing that the trilinear Higgs coupling accounts for around 15% of the non-resonant cross section, as shown in Tables 4.3 and 4.4.

A systematic investigation of the parameter space of both models was conducted using a clustering algorithm. This two-stage exploration begins with physics at the "Low Scale" (see Chapter 4) concentrating on the part of the parameter space that the HL-LHC can probe. In a subsequent stage, the analysis is extended to the "High Scale" (see Chapter 5) region, including mass parameters that reach up to 30 TeV, which is of interest for future planned colliders such as the 100 TeV FCC-hh and the SppC. Then, a set of representative points were selected for each energy regime. These points comprehensively summarize the phenomenology of the parameter space of the models. They are listed in Tables 4.1, 4.5, and 5.1 for the MCHM_5, and in Tables 4.2, 4.6, and 5.2 for the MCHM_{14}.

As part of the exploration, representative points with sizable three-body decays

were found. In Chapter 6, we saw that this behaviour arises for fourplet-like points[1], in which the lightest states form a near degenerate doublet. Although we focused on the MCHM, we expect this to happen generally in any model with a vector-like doublet. The inclusion of these three-body channels in experimental searches can increase previous exclusion limits. In Chapter 7, we estimated that, for the case of the lightest 2/3-charged top partner, $T^{(1)}$, its exclusion limit in the same-sign dilepton channel [40] can increase by $80-100$ GeV. This happens because the 3-body decay of $T^{(1)}$ into W^+W^-t increase the probability of producing two same-sign leptons in the final state, as compared with the two-body channels, which allows the events to survive the kinematical cuts more easily.

However, when two resonances are nearly degenerate, another feature emerges: there is an additional off-shell contribution from one of the two resonances that increases the total cross section. Since it is difficult to isolate the two states, we proposed an inclusive search in Chapter 8 in three scenarios: two same-sign lepton, three-lepton and their combination. The results are shown in Tables 8.4, 8.5 and 8.6, respectively. In the combined scenario and for a point with relatively low resonances with mass 1.3 TeV, we get a significance $S/\sqrt{B} = 15$ at the HL-LHC with a luminosity of 4 ab^{-1}. If we scale it according to the production cross section we reach masses of 1.5 TeV for $S/\sqrt{B} = 5$ and 1.6 TeV for $S/\sqrt{B} = 3$, indicating opportunities of discovery or evidence at the HL-LHC. Furthermore, the analysis presented here can be further improved by using more complex techniques than the simple cut-and-count analysis performed.

Overall, this thesis provides a comprehensive examination of MCHM models at high energy hadron colliders and contributes to the ongoing efforts to uncover new physics beyond the Standard Model.

[1] See the definitions after Equation 6.6

Appendix A

Representations of SO(5)

We use the following 5×5 matrix representation of the generators T^B of SO(5):

$$T^1_L = \begin{pmatrix} 0 & 0 & 0 & -\frac{i}{2} & 0 \\ 0 & 0 & -\frac{i}{2} & 0 & 0 \\ 0 & \frac{i}{2} & 0 & 0 & 0 \\ \frac{i}{2} & 0 & 0 & 0 & 0 \\ 0 & 0 & 0 & 0 & 0 \end{pmatrix}, \; T^2_L = \begin{pmatrix} 0 & 0 & \frac{i}{2} & 0 & 0 \\ 0 & 0 & 0 & -\frac{i}{2} & 0 \\ -\frac{i}{2} & 0 & 0 & 0 & 0 \\ 0 & \frac{i}{2} & 0 & 0 & 0 \\ 0 & 0 & 0 & 0 & 0 \end{pmatrix},$$

$$T^3_L = \begin{pmatrix} 0 & -\frac{i}{2} & 0 & 0 & 0 \\ \frac{i}{2} & 0 & 0 & 0 & 0 \\ 0 & 0 & 0 & -\frac{i}{2} & 0 \\ 0 & 0 & \frac{i}{2} & 0 & 0 \\ 0 & 0 & 0 & 0 & 0 \end{pmatrix}, \; T^1_R = \begin{pmatrix} 0 & 0 & 0 & \frac{i}{2} & 0 \\ 0 & 0 & -\frac{i}{2} & 0 & 0 \\ 0 & \frac{i}{2} & 0 & 0 & 0 \\ -\frac{i}{2} & 0 & 0 & 0 & 0 \\ 0 & 0 & 0 & 0 & 0 \end{pmatrix}$$

$$T^2_R = \begin{pmatrix} 0 & 0 & \frac{i}{2} & 0 & 0 \\ 0 & 0 & 0 & \frac{i}{2} & 0 \\ -\frac{i}{2} & 0 & 0 & 0 & 0 \\ 0 & -\frac{i}{2} & 0 & 0 & 0 \\ 0 & 0 & 0 & 0 & 0 \end{pmatrix}, \; T^3_R = \begin{pmatrix} 0 & -\frac{i}{2} & 0 & 0 & 0 \\ \frac{i}{2} & 0 & 0 & 0 & 0 \\ 0 & 0 & 0 & \frac{i}{2} & 0 \\ 0 & 0 & -\frac{i}{2} & 0 & 0 \\ 0 & 0 & 0 & 0 & 0 \end{pmatrix}$$

$$T^{\hat{1}} = \begin{pmatrix} 0 & 0 & 0 & 0 & -\frac{i}{\sqrt{2}} \\ 0 & 0 & 0 & 0 & 0 \\ 0 & 0 & 0 & 0 & 0 \\ 0 & 0 & 0 & 0 & 0 \\ \frac{i}{\sqrt{2}} & 0 & 0 & 0 & 0 \end{pmatrix}, \; T^{\hat{2}} = \begin{pmatrix} 0 & 0 & 0 & 0 & 0 \\ 0 & 0 & 0 & 0 & -\frac{i}{\sqrt{2}} \\ 0 & 0 & 0 & 0 & 0 \\ 0 & 0 & 0 & 0 & 0 \\ 0 & \frac{i}{\sqrt{2}} & 0 & 0 & 0 \end{pmatrix},$$

$$T^{\hat{3}} = \begin{pmatrix} 0 & 0 & 0 & 0 & 0 \\ 0 & 0 & 0 & 0 & 0 \\ 0 & 0 & 0 & 0 & -\frac{i}{\sqrt{2}} \\ 0 & 0 & 0 & 0 & 0 \\ 0 & 0 & \frac{i}{\sqrt{2}} & 0 & 0 \end{pmatrix}, \; T^{\hat{4}} = \begin{pmatrix} 0 & 0 & 0 & 0 & 0 \\ 0 & 0 & 0 & 0 & 0 \\ 0 & 0 & 0 & 0 & 0 \\ 0 & 0 & 0 & 0 & -\frac{i}{\sqrt{2}} \\ 0 & 0 & 0 & \frac{i}{\sqrt{2}} & 0 \end{pmatrix}, \tag{A.1}$$

which act on the fundamental representation **5** of SO(5) as $\delta\Psi_{\mathbf{5}} = T^B\Psi_{\mathbf{5}}$. We write the **5** representation (using a notation appropriate for states with $U(1)_X$ charge $X = 2/3$) as

$$\Psi_{\mathbf{5}}^{(2/3)} \;=\; X_{5/3}\, v_{\frac{1}{2},\frac{1}{2}} + X_{2/3}\, v_{-\frac{1}{2},\frac{1}{2}} + T\, v_{\frac{1}{2},-\frac{1}{2}} + B\, v_{-\frac{1}{2},-\frac{1}{2}} + \tilde{T}\, v_0 \;, \tag{A.2}$$

where we used the normalized basis

$$\begin{aligned} v_{\frac{1}{2},\frac{1}{2}} &= \frac{1}{\sqrt{2}} \begin{pmatrix} i \\ -1 \\ 0 \\ 0 \\ 0 \end{pmatrix}, \quad v_{-\frac{1}{2},\frac{1}{2}} = \frac{1}{\sqrt{2}} \begin{pmatrix} 0 \\ 0 \\ -i \\ -1 \\ 0 \end{pmatrix}, \\ v_{\frac{1}{2},-\frac{1}{2}} &= \frac{1}{\sqrt{2}} \begin{pmatrix} 0 \\ 0 \\ -i \\ 1 \\ 0 \end{pmatrix}, \quad v_{-\frac{1}{2},-\frac{1}{2}} = \frac{1}{\sqrt{2}} \begin{pmatrix} -i \\ -1 \\ 0 \\ 0 \\ 0 \end{pmatrix}, \end{aligned}$$

and

$$v_0^T = (0,0,0,0,1) \;.$$

The notation is such that the subindices a, b denote the $T^3_{L,R}$ eigenvalues: $T^3_L\, v_{a,b} = a\, v_{a,b}$, $T^3_R\, v_{a,b} = b\, v_{a,b}$, while v_0 denotes the complete singlet, $T^i_L\, v_0 = T^i_R\, v_0 = 0$. Furthermore, one has $T^+_L\, v_{\frac{1}{2},\pm\frac{1}{2}} = 0$, $T^+_L\, v_{-\frac{1}{2},\pm\frac{1}{2}} = v_{\frac{1}{2},\pm\frac{1}{2}}$, $T^-_L\, v_{\frac{1}{2},\pm\frac{1}{2}} = v_{-\frac{1}{2},\pm\frac{1}{2}}$, $T^-_L\, v_{-\frac{1}{2},\pm\frac{1}{2}} = 0$, and similarly $T^+_R\, v_{\pm\frac{1}{2},\frac{1}{2}} = 0$, $T^+_R\, v_{\pm\frac{1}{2},-\frac{1}{2}} = v_{\pm\frac{1}{2},\frac{1}{2}}$, $T^-_R\, v_{\pm\frac{1}{2},\frac{1}{2}} = v_{\pm\frac{1}{2},-\frac{1}{2}}$, $T^-_R\, v_{\pm\frac{1}{2},-\frac{1}{2}} = 0$, where $T^\pm_{L,R} \equiv T^1_{L,R} \pm i T^2_{L,R}$ are the standard $SU(2)$ raising and lowering operators, satisfying

$$\begin{aligned} [T^3_L, T^\pm_L] &= \pm T^\pm_L \;, \qquad [T^3_R, T^\pm_R] = \pm T^\pm_R \;, \\ [T^+_L, T^-_L] &= 2\, T^3_L \;, \qquad [T^+_R, T^-_R] = 2\, T^3_R \;, \end{aligned}$$

and $[T_L^i, T_R^j] = 0$. The states satisfy the standard normalization

$$\begin{aligned} T_L^{\pm}|s_L, m_L; s_R, m_R\rangle &= \sqrt{s_L(s_L+1) - m_L(m_L \mp 1)}\,|s_L, m_L \pm 1; s_R, m_R\rangle \ , \\ T_R^{\pm}|s_L, m_L; s_R, m_R\rangle &= \sqrt{s_R(s_R+1) - m_R(m_R \mp 1)}\,|s_L, m_L; s_R, m_R \pm 1\rangle \ . \end{aligned}$$

Thus, $\mathbf{\Psi_4} \sim (X_{5/3}, X_{2/3}, T, B)$ is a bi-doublet $(\mathbf{2},\mathbf{2})$ of $SU(2)_L \times SU(2)_R$ with $(s_L, s_R) = (1/2, 1/2)$, while $\mathbf{\Psi_1} \sim \tilde{T}$ is a singlet with $(s_L, s_R) = (0, 0)$.

The **14** representation of SO(5) can be written in terms of a 5×5 symmetric and traceless matrix, such that the $SO(5)$ generators (A.1) act as $\delta\mathbf{\Psi_{14}} = [T^B, \mathbf{\Psi_{14}}]$. Using again the notation for states with $X = 2/3$, we write

$$\begin{aligned} \mathbf{\Psi}_{\mathbf{14}}^{(2/3)} &= \tilde{T}\, S_0 + (X_{\frac{5}{3}}\, S_{\frac{1}{2},\frac{1}{2}} + X_{\frac{2}{3}}\, S_{-\frac{1}{2},\frac{1}{2}} + T\, S_{\frac{1}{2},-\frac{1}{2}} + B\, S_{-\frac{1}{2},-\frac{1}{2}}) \\ &\quad + [U_{\frac{8}{3}} S_{1,1} + U_{\frac{5}{3}} S_{0,1} + U_{\frac{2}{3}} S_{-1,1} \\ &\quad + \ V_{\frac{5}{3}}\, S_{1,0} + V_{\frac{2}{3}}\, S_{0,0} + V_{-\frac{1}{3}}\, S_{-1,0} \\ &\quad + \ F_{\frac{2}{3}}\, S_{1,-1} + F_{-\frac{1}{3}}\, S_{0,-1} + F_{-\frac{4}{3}}\, S_{-1,-1}] \end{aligned} \tag{A.3}$$

which exhibits the decomposition $\mathbf{14} \sim (\mathbf{3},\mathbf{3}) + (\mathbf{2},\mathbf{2}) + (\mathbf{1},\mathbf{1})$ under $\mathrm{SU}(2)_L \times \mathrm{SU}(2)_R$.

The notation for the basis $S_{a,b}$ is the same as explained above, e.g. $[T_L^3, S_{a,b}] = a\, S_{a,b}$, $[T_R^3, S_{a,b}] = b\, S_{a,b}$, while S_0 denotes the complete singlet, $[T_L^i, S_0] = [T_R^i, S_0] = 0$. The states $\mathbf{\Psi_9} \sim (U_{8/3}, U_{5/3}, U_{2/3}, V_{5/3}, V_{2/3}, V_{-1/3}, F_{2/3}, F_{-1/3}, F_{-4/3})$ transform as a bi-triplet of $SU(2)_L \times SU(2)_R$ with $(s_L, s_R) = (1, 1)$, and the bi-doublet $\mathbf{\Psi_4}$ and singlet $\mathbf{\Psi_1}$ follow the same notation used for the **5** of $SO(5)$ above. The subindices on the fields denote the electric charge, given by

$$Q = T_L^3 + T_R^3 + X \ . \tag{A.4}$$

Explicitly, the $S_{a,b}$ and S_0 matrices are given by:

$$S_{1,1} = \frac{1}{2}\begin{pmatrix} 1 & i & 0 & 0 & 0 \\ i & -1 & 0 & 0 & 0 \\ 0 & 0 & 0 & 0 & 0 \\ 0 & 0 & 0 & 0 & 0 \\ 0 & 0 & 0 & 0 & 0 \end{pmatrix}, \quad S_{1,0} = \frac{1}{2\sqrt{2}}\begin{pmatrix} 0 & 0 & -1 & -i & 0 \\ 0 & 0 & -i & 1 & 0 \\ -1 & -i & 0 & 0 & 0 \\ -i & 1 & 0 & 0 & 0 \\ 0 & 0 & 0 & 0 & 0 \end{pmatrix},$$

$$S_{1,-1} = \frac{1}{2}\begin{pmatrix} 0 & 0 & 0 & 0 & 0 \\ 0 & 0 & 0 & 0 & 0 \\ 0 & 0 & 1 & i & 0 \\ 0 & 0 & i & -1 & 0 \\ 0 & 0 & 0 & 0 & 0 \end{pmatrix}, \quad S_{0,1} = \frac{1}{2\sqrt{2}}\begin{pmatrix} 0 & 0 & -1 & i & 0 \\ 0 & 0 & -i & -1 & 0 \\ -1 & -i & 0 & 0 & 0 \\ i & -1 & 0 & 0 & 0 \\ 0 & 0 & 0 & 0 & 0 \end{pmatrix},$$

$$S_{0,0} = \frac{1}{2}\begin{pmatrix} -1 & 0 & 0 & 0 & 0 \\ 0 & -1 & 0 & 0 & 0 \\ 0 & 0 & 1 & 0 & 0 \\ 0 & 0 & 0 & 1 & 0 \\ 0 & 0 & 0 & 0 & 0 \end{pmatrix}, \quad S_{0,-1} = \frac{1}{2\sqrt{2}}\begin{pmatrix} 0 & 0 & 1 & i & 0 \\ 0 & 0 & -i & 1 & 0 \\ 1 & -i & 0 & 0 & 0 \\ i & 1 & 0 & 0 & 0 \\ 0 & 0 & 0 & 0 & 0 \end{pmatrix},$$

$$S_{-1,1} = \frac{1}{2}\begin{pmatrix} 0 & 0 & 0 & 0 & 0 \\ 0 & 0 & 0 & 0 & 0 \\ 0 & 0 & 1 & -i & 0 \\ 0 & 0 & -i & -1 & 0 \\ 0 & 0 & 0 & 0 & 0 \end{pmatrix}, \quad S_{-1,0} = \frac{1}{2\sqrt{2}}\begin{pmatrix} 0 & 0 & 1 & -i & 0 \\ 0 & 0 & -i & -1 & 0 \\ 1 & -i & 0 & 0 & 0 \\ -i & -1 & 0 & 0 & 0 \\ 0 & 0 & 0 & 0 & 0 \end{pmatrix},$$

$$S_{-1,-1} = \frac{1}{2}\begin{pmatrix} 1 & -i & 0 & 0 & 0 \\ -i & -1 & 0 & 0 & 0 \\ 0 & 0 & 0 & 0 & 0 \\ 0 & 0 & 0 & 0 & 0 \\ 0 & 0 & 0 & 0 & 0 \end{pmatrix},$$

for the **9** of $SO(4) = SU(2)_L \times SU(2)_R$,

$$S_{\frac{1}{2},\frac{1}{2}} = \frac{1}{2}\begin{pmatrix} 0 & 0 & 0 & 0 & i \\ 0 & 0 & 0 & 0 & -1 \\ 0 & 0 & 0 & 0 & 0 \\ 0 & 0 & 0 & 0 & 0 \\ i & -1 & 0 & 0 & 0 \end{pmatrix}, \quad S_{\frac{1}{2},-\frac{1}{2}} = \frac{1}{2}\begin{pmatrix} 0 & 0 & 0 & 0 & 0 \\ 0 & 0 & 0 & 0 & 0 \\ 0 & 0 & 0 & 0 & -i \\ 0 & 0 & 0 & 0 & 1 \\ 0 & 0 & -i & 1 & 0 \end{pmatrix},$$

$$S_{-\frac{1}{2},\frac{1}{2}} = \frac{1}{2}\begin{pmatrix} 0 & 0 & 0 & 0 & 0 \\ 0 & 0 & 0 & 0 & 0 \\ 0 & 0 & 0 & 0 & -i \\ 0 & 0 & 0 & 0 & -1 \\ 0 & 0 & -i & -1 & 0 \end{pmatrix}, \quad S_{-\frac{1}{2},-\frac{1}{2}} = \frac{1}{2}\begin{pmatrix} 0 & 0 & 0 & 0 & -i \\ 0 & 0 & 0 & 0 & -1 \\ 0 & 0 & 0 & 0 & 0 \\ 0 & 0 & 0 & 0 & 0 \\ -i & -1 & 0 & 0 & 0 \end{pmatrix},$$

for the **4** of $SO(4)$, and

$$S_0 = \frac{1}{2\sqrt{5}}\begin{pmatrix} 1 & 0 & 0 & 0 & 0 \\ 0 & 1 & 0 & 0 & 0 \\ 0 & 0 & 1 & 0 & 0 \\ 0 & 0 & 0 & 1 & 0 \\ 0 & 0 & 0 & 0 & -4 \end{pmatrix}.$$

for the $SO(4)$ singlet. These matrices form an orthonormal basis: $\mathrm{Tr}(S_A^* S_B) = \delta_{AB}$.

Appendix B

Embeddings of $SO(4)$ into $SO(5)$

The four NGBs resulting from the spontaneous breaking of $SO(5) \to SO(4) = SU(2)_L \times SU(2)_R$ can be parametrized as

$$U = e^{i\frac{\sqrt{2}}{f}h^{\hat{a}}T^{\hat{a}}} , \tag{B.1}$$

where $T^{\hat{a}}$ are the (four) broken generators in $SO(5)/SO(4)$ given in Eq (A.1) and f is the scale of spontaneous symmetry breaking. The $h^{\hat{a}}$ transform as a 4-plet of $SO(4)$, and can be arranged in a doublet of $SU(2)_L$ as:

$$H = \frac{1}{\sqrt{2}}\begin{pmatrix} h_2 + ih_1 \\ h_4 - ih_3 \end{pmatrix} . \tag{B.2}$$

One can assume that EWSB proceeds through a non-vanishing vev $h_0 = \langle h_4 \rangle$, with the vev's of the other components vanishing. In unitary gauge, $h_1 = h_2 = h_3 = 0$ and $h_4 = h_0 + h$, where h is the physical Higgs boson. Using the explicit form of the broken generators results in the matrix given in Eq. (2.1).

It is also easy to embed the various fermion $SO(4)$ multiplets used in the main text into (incomplete) representations of $SO(5)$ that simplify the writing of the Lagrangian. For example,

- For the MCHM$_5$:

  The elementary fermions are written as

$$\begin{aligned} Q_L^{\mathbf{5}} &= t_L\, v_{\frac{1}{2},-\frac{1}{2}} + b_L\, v_{-\frac{1}{2},-\frac{1}{2}} , \\ T_R^{\mathbf{5}} &= t_R\, v_0 , \end{aligned}$$

  and the composite fermions are written as

$$\begin{aligned} \mathbf{\Psi_4} &= X_{5/3}\, v_{\frac{1}{2},\frac{1}{2}} + X_{2/3}\, v_{-\frac{1}{2},\frac{1}{2}} + T\, v_{\frac{1}{2},-\frac{1}{2}} + B\, v_{-\frac{1}{2},-\frac{1}{2}} , \\ \mathbf{\Psi_1} &= \tilde{T}\, v_0 . \end{aligned}$$

These result in Eqs. (2.9) and (2.10).

- For the MCHM$_{14}$:

  The elementary fermions are written as

$$\begin{aligned} Q_L^{\mathbf{14}} &= t_L\, S_{\frac{1}{2},-\frac{1}{2}} + b_L\, S_{-\frac{1}{2},-\frac{1}{2}}\ , \\ T_R^{\mathbf{14}} &= t_R\, S_0\ , \end{aligned}$$

  and the composite fermions are written as

$$\begin{aligned} \mathbf{\Psi_9} &= [U_{\frac{8}{3}} S_{1,1} + U_{\frac{5}{3}} S_{0,1} + U_{\frac{2}{3}} S_{-1,1} \\ &\quad + V_{\frac{5}{3}}\, S_{1,0} + V_{\frac{2}{3}}\, S_{0,0} + V_{-\frac{1}{3}}\, S_{-1,0} \\ &\quad + F_{\frac{2}{3}}\, S_{1,-1} + F_{-\frac{1}{3}}\, S_{0,-1} + F_{-\frac{4}{3}}\, S_{-1,-1}] \\ \mathbf{\Psi_4} &= X_{5/3}\, S_{\frac{1}{2},\frac{1}{2}} + X_{2/3}\, S_{-\frac{1}{2},\frac{1}{2}} + T\, S_{\frac{1}{2},-\frac{1}{2}} + B\, S_{-\frac{1}{2},-\frac{1}{2}}\ , \\ \mathbf{\Psi_1} &= \tilde{T}\, S_0\ . \end{aligned}$$

  All of these are traceless, symmetric 5×5 matrices. It is then straightforward to form a complete **14** of $SO(5)$ as

$$\mathbf{\Psi_{14}} = \mathbf{\Psi_9} + \mathbf{\Psi_4} + \mathbf{\Psi_1}\ .$$

Appendix C

Explicit form of the Lagrangian terms with the d_μ and e_μ symbols

In unitary gauge, the gauged d_μ and e_μ symbols are given by

$$d_\mu = \left\{ \frac{g}{\sqrt{2}} W_\mu^1 s_h,\ \frac{g}{\sqrt{2}} W_\mu^2 s_h,\ \frac{g W_\mu^3 - g' B_\mu}{\sqrt{2}} s_h,\ \frac{\partial_\mu h}{f} \right\} \tag{C.1}$$

$$e_\mu = \frac{i}{2} \begin{pmatrix} 0 & -g' B_\mu - g W_\mu^3 & g W_\mu^2 & -g W_\mu^1 c_h \\ g' B_\mu + g W_\mu^3 & 0 & -g W_\mu^1 & -g W_\mu^2 c_h \\ -g W_\mu^2 & g W_\mu^1 & 0 & (g' B_\mu - g W_\mu^3) c_h \\ g W_\mu^1 c_h & g W_\mu^2 c_h & -(g' B_\mu - g W_\mu^3) c_h & 0 \end{pmatrix}, \tag{C.2}$$

where $c_h = \cos \frac{h_0 + h}{f}$ and $s_h = \sin \frac{h_0 + h}{f}$. Under $SO(4)$, d_μ^i transforms in the fundamental and e_μ^a in the adjoint.

Let us take the terms containing the d_μ symbol in Equations 2.7 and 2.17 and define:

$$\mathcal{L}_{\rm d}^{\mathbf{5}} = -i\, c_L\, \overline{\Psi}_{\mathbf{4}} P_L \not{d}\, \Psi_{\mathbf{1}} - i\, c_R\, \overline{\Psi}_{\mathbf{4}} P_R \not{d}\, \Psi_{\mathbf{1}} + \text{h.c.}, \tag{C.3}$$

$$\mathcal{L}_{\rm d}^{\mathbf{14}} = -i\, c_4\, \overline{\Psi}_4 \not{d}\, \Psi_1 - i\, c_9\, \overline{\Psi}_{\mathbf{9}}^{ij} \not{d}^i\, \Psi_{\mathbf{4}}^j - i\, \frac{c_{T9}}{4\pi f}\, \overline{\Psi}_{\mathbf{9}}^{ij}\, d_\mu^i d^{j\,\mu}\, \tilde{T} + \text{h.c.}. \tag{C.4}$$

Using the fermion embeddings defined in Appendix B and Equations C.1 and C.2, we can write, explicitly, the Lagrangian terms above in the interaction basis as:

$$\begin{aligned} \mathcal{L}_{\rm d}^{\mathbf{5}} = \ & c_R \left\{ g\sqrt{\xi} \left[\frac{1}{\sqrt{2}} \left(\overline{X}_{5/3}\right)_R \not{W}^+ \tilde{T}_R - \frac{1}{\sqrt{2}} \overline{B}_R \not{W}^- \tilde{T}_R - \frac{1}{2c_w} \overline{T}_R \not{Z} \tilde{T}_R \right.\right. \\ & \left.\left. - \frac{1}{2c_w} \left(\overline{X}_{2/3}\right)_R \not{Z} \tilde{T}_R \right] + i \left[\left(\overline{X}_{2/3}\right)_R - \overline{T}_R \right] \frac{\not{\partial} h}{f} \tilde{T}_R \right\} + (R \to L) + \text{h.c.}, \end{aligned} \tag{C.5}$$

$$
\begin{aligned}
\mathcal{L}_{\rm d}^{\mathbf{14}} &= c_4\left[g\sqrt{\xi}\left(\frac{1}{\sqrt{2}}\overline{X}_{5/3}\not{W}^{+}\tilde{T}-\frac{1}{\sqrt{2}}\overline{B}\not{W}^{-}\tilde{T}-\frac{1}{2c_w}\overline{T}\not{Z}\tilde{T}\ -\frac{1}{2c_w}\overline{X}_{2/3}\not{Z}\tilde{T}\right)\right.\\
&\qquad\left.+i\left(\overline{X}_{2/3}-\overline{T}\right)\frac{\not{\partial}h}{f}\tilde{T}\right]\\
&- \frac{1}{4}\,c_9\,\frac{g_2}{c_w}\sqrt{\xi}\left\{\sqrt{2}\left[\overline{V}_{-1/3}+\overline{F}_{-1/3}\right]\not{Z}B+\left[\overline{V}_{2/3}+2\overline{U}_{2/3}\right]\not{Z}X_{2/3}\right.\\
&+ \left.\left[\overline{V}_{2/3}+2\overline{F}_{2/3}\right]\not{Z}T+\sqrt{2}\left[\overline{U}_{5/3}+\overline{V}_{5/3}\right]\not{Z}X_{5/3}\right\}\\
&- \frac{1}{4}c_9g_2\sqrt{\xi}\left\{\sqrt{2}\overline{V}_{2/3}\not{W}^{-}\overline{X}_{5/3}+2\sqrt{2}\overline{F}_{-4/3}\not{W}^{-}B+2\overline{F}_{-1/3}\not{W}^{-}T+2\overline{V}_{-1/3}\not{W}^{-}X_{2/3}\right.\\
&- \left.\sqrt{2}\overline{V}_{2/3}\not{W}^{+}B+2\sqrt{2}\overline{U}_{8/3}\not{W}^{+}X_{5/3}+2\overline{V}_{5/3}\not{W}^{+}T+2\overline{U}_{5/3}\not{W}^{+}X_{2/3}\right\}\\
&+ \frac{i}{2f}c_9\left\{\sqrt{2}\left[\overline{V}_{-1/3}-\overline{F}_{-1/3}\right]\not{\partial}hB+\left[\overline{V}_{2/3}-2\overline{F}_{2/3}\right]\not{\partial}h\,T+\right.\\
&\left.\left[2\overline{U}_{2/3}-\overline{V}_{2/3}\right]\not{\partial}h\,X_{2/3}+\sqrt{2}\left[\overline{U}_{5/3}-\overline{V}_{5/3}\right]\not{\partial}h\,X_{5/3}\right\}\\
&+ \frac{ic_{T9}}{4\pi f^3}\partial_\mu h\,\partial^\mu h\left[\overline{U}_{2/3}-\overline{V}_{2/3}+\overline{F}_{2/3}\right]\tilde{T}\\
&+ \frac{c_{T9}g_2\sqrt{\xi}}{4\pi f^2c_w}Z_\mu\left[\partial^\mu h\left(\overline{F}_{2/3}-\overline{U}_{2/3}\right)+W_\mu^{+}\left(\overline{U}_{5/3}-\overline{V}_{5/3}\right)+W_\mu^{-}\left(\overline{F}_{-1/3}-\overline{V}_{-1/3}\right)\right]\tilde{T}\\
&+ \frac{ic_{T9}g_2^2\xi}{8\pi f}\left[-\frac{Z_\mu Z^\mu}{2c_w}\left(\overline{U}_{2/3}+\overline{V}_{2/3}+\overline{F}_{2/3}\right)-W_\mu^{+}W^{+\mu}\overline{U}_{8/3}-W_\mu^{-}W^{-\mu}\overline{F}_{-4/3}\right.\\
&+ \left.W_\mu^{+}W^{-\mu}\overline{V}_{2/3}-\frac{Z_\mu W^{-\mu}}{c_w}\left(\overline{V}_{-1/3}+\overline{F}_{-1/3}\right)+\frac{Z_\mu W^{+\mu}}{c_w}\left(\overline{U}_{5/3}+\overline{V}_{5/3}\right)\right]\tilde{T}+\text{h. c.},
\end{aligned}
$$

where c_w is the cosine of the Weinberg angle.

Now, we can take, conveniently, some terms from Eq. 2.7 and 2.17 and define:

$$\mathcal{L}_{\rm e}^{\mathbf{5}} = \overline{\Psi}_{\mathbf{4}}\left(\frac{2}{3}g'\not{B}-\not{e}\right)\Psi_{\mathbf{4}}, \tag{C.6}$$

$$\mathcal{L}_{\rm e}^{\mathbf{14}} = \overline{\Psi}_{\mathbf{9}}\left(\frac{2}{3}g'\not{B}\Psi_{\mathbf{9}}-[\not{e},\Psi_{\mathbf{9}}]\right). \tag{C.7}$$

This terms will lead to electroweak corrections due to compositeness that are given by:

$$
\begin{aligned}
\mathcal{L}_{\mathrm{e}}^{\mathbf{5}} &= \overline{\Psi}_{\mathbf{4}}\left(\frac{2}{3}g'\not{B}-\not{e}\right)\Psi_{\mathbf{4}} \\
&= \frac{g}{c_w}\left[\left(-\frac{1}{2}+\frac{1}{3}s_w^2\right)\overline{B}\not{Z}B+\left(\frac{1}{2}-\frac{5}{3}s_w^2\right)\overline{X}_{5/3}\not{Z}X_{5/3}\right. \\
&+ \left.\left(\frac{\sqrt{1-\xi}}{2}-\frac{2}{3}s_w^2\right)\overline{T}\not{Z}T+\left(-\frac{\sqrt{1-\xi}}{2}-\frac{2}{3}s_w^2\right)\overline{X}_{2/3}\not{Z}X_{2/3}\right] \\
&+ \frac{g}{\sqrt{2}}\frac{1+\sqrt{1-\xi}}{2}\left[\overline{B}\not{W}^-T+\overline{X}_{5/3}\not{W}^+X_{2/3}+\text{h. c.}\right] \\
&+ \frac{g}{\sqrt{2}}\frac{1-\sqrt{1-\xi}}{2}\left[\overline{X}_{5/3}\not{W}^+T+\overline{B}\not{W}^-X_{2/3}+\text{h. c.}\right], \qquad \text{(C.8)}
\end{aligned}
$$

$$
\begin{aligned}
\mathcal{L}_{\mathrm{e}}^{\mathbf{14}} &= \overline{\Psi}_{\mathbf{9}}\left(\frac{2}{3}g'\not{B}\Psi_{\mathbf{9}}-[\not{e},\Psi_{\mathbf{9}}]\right) \\
&= \frac{g}{c_w}\left[\left(-\sqrt{1-\xi}+-\frac{2}{3}s_w^2\right)\overline{U}_{2/3}\not{Z}U_{2/3}+\left(\frac{1-\sqrt{1-\xi}}{2}-\frac{5}{3}s_w^2\right)\overline{U}_{5/3}\not{Z}U_{5/3}\right. \\
&+ \left(\frac{1}{2}-\frac{8}{3}s_w^2\right)\overline{U}_{8/3}\not{Z}U_{8/3}+\left(-\frac{1+\sqrt{1-\xi}}{2}+\frac{1}{3}s_w^2\right)\overline{V}_{-1/3}\not{Z}V_{-1/3} \\
&+ -\frac{2}{3}s_w^2\overline{V}_{2/3}\not{Z}V_{2/3}+\left(\frac{1+\sqrt{1-\xi}}{2}+\frac{1}{3}s_w^2\right)\overline{V}_{5/3}\not{Z}V_{5/3} \\
&+ \left(-1+\frac{4}{3}s_w^2\right)\overline{F}_{-4/3}\not{Z}F_{-4/3}+\left(-\frac{1-\sqrt{1-\xi}}{2}+\frac{1}{3}s_w^2\right)\overline{F}_{-1/3}\not{Z}F_{-1/3} \\
&+ \left.\left(\sqrt{1-\xi}-\frac{2}{3}s_w^2\right)\overline{F}_{2/3}\not{Z}F_{2/3}\right] \\
&+ \frac{g}{2}(1+\sqrt{1-\xi})\left[\overline{V}_{5/3}\not{W}^+V_{2/3}+\overline{V}_{2/3}\not{W}^+V_{-1/3}\right. \\
&+ \overline{F}_{-1/3}\not{W}^+F_{-4/3}+\overline{F}_{2/3}\not{W}^+F_{-1/3} \\
&+ \left.\overline{U}_{8/3}\not{W}^+U_{5/3}+\overline{U}_{5/3}\not{W}^+U_{2/3}+\text{h. c.}\right] \\
&+ \frac{g}{2}(1-\sqrt{1-\xi})\left[\overline{V}_{-1/3}\not{W}^+F_{-4/3}+\overline{V}_{2/3}\not{W}^+F_{-1/3}\right. \\
&+ \overline{V}_{5/3}\not{W}^+F_{2/3}+\overline{U}_{5/3}\not{W}^+V_{2/3} \\
&+ \left.\overline{U}_{8/3}\not{W}^+V_{5/3}+\overline{U}_{2/3}\not{W}^+V_{-1/3}+\text{h. c.}\right]. \qquad \text{(C.9)}
\end{aligned}
$$

Appendix D

Results of the clustering algorithm applied to the parameter space of the MCHM

This appendix contains the plots relative to the clustering of sections 4.4.2, 5.2.1 and 5.2.2, according to the table below.

Model and Scan	Section	Figures
Low Scale MCHM_{14}	4.4.2	D.1 and D.2
High Scale MCHM_{5}	5.2.1	D.3 and D.4
High Scale MCHM_{14}	5.2.2	D.5 and D.6

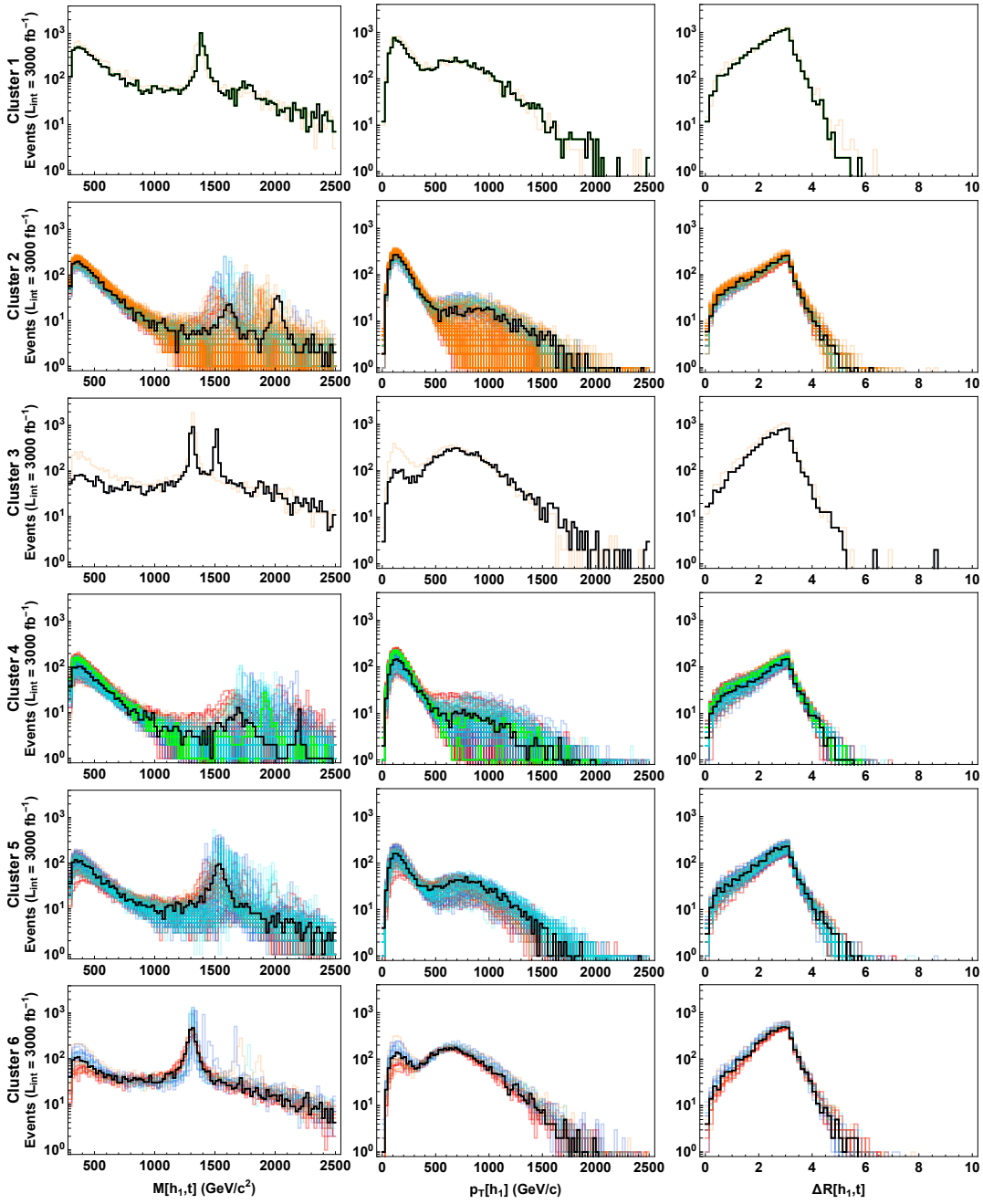

Figure D.1: Distributions at $\sqrt{s} = 14$ TeV for the invariant mass of the pair composed by top and most energetic Higgs h_1 (first column), transverse momenta of h_1 (second column) and angular distances in the transverse plane between h_1 and the top (third column), organized in clusters by similarity (clusters 1 through 6). Red, blue, orange and cyan curves indicate respectively points in Regions I, II, III and IV of the LS-MCHM$_{14}$. The benchmark point for each cluster is shown in black, with clusters 1 to 6 containing respectively points D_1 to D_6 in Table 4.6. The example points (see Table 4.2) are shown in green (cluster 1 contains Q_1, cluster 4 contains Q_5 and Q_7).

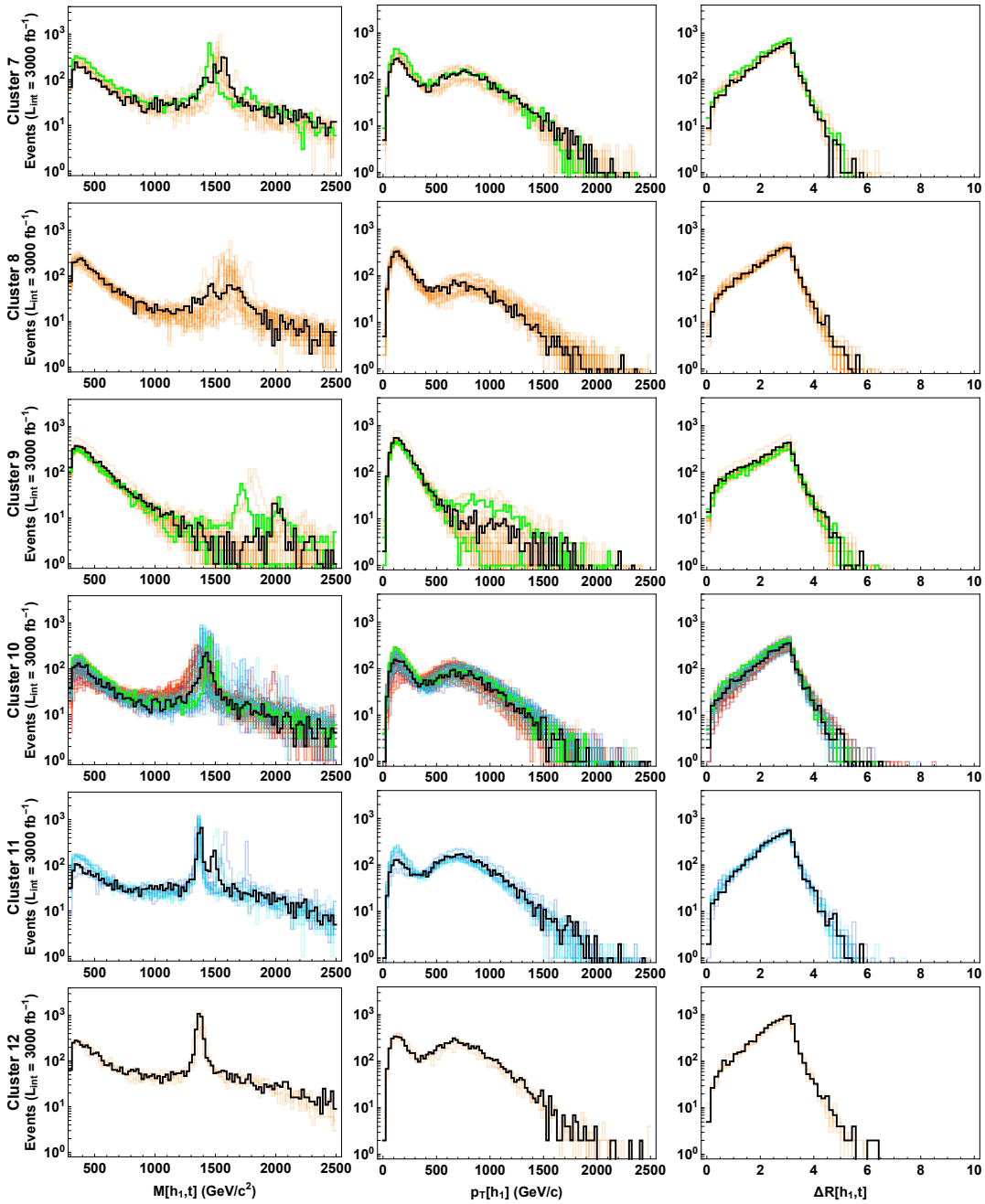

Figure D.2: Distributions at $\sqrt{s} = 14$ TeV for the invariant mass of the pair composed by top and most energetic Higgs h_1 (first column), transverse momenta of h_1 (second column) and angular distances in the transverse plane between h_1 and the top (third column), organized in clusters by similarity (clusters 7 through 12). Red, blue, orange and cyan curves indicate respectively points in Regions I, II, III and IV of the LS-MCHM$_{14}$. The benchmark point for each cluster is shown in black, with clusters 7 to 12 containing respectively points D_7 to D_{12} in Table 4.6. The example points (see Table 4.2) are shown in green (cluster 7 contains Q_2, cluster 9 contains Q_3 and Q_4 and cluster 10 contains Q_6).

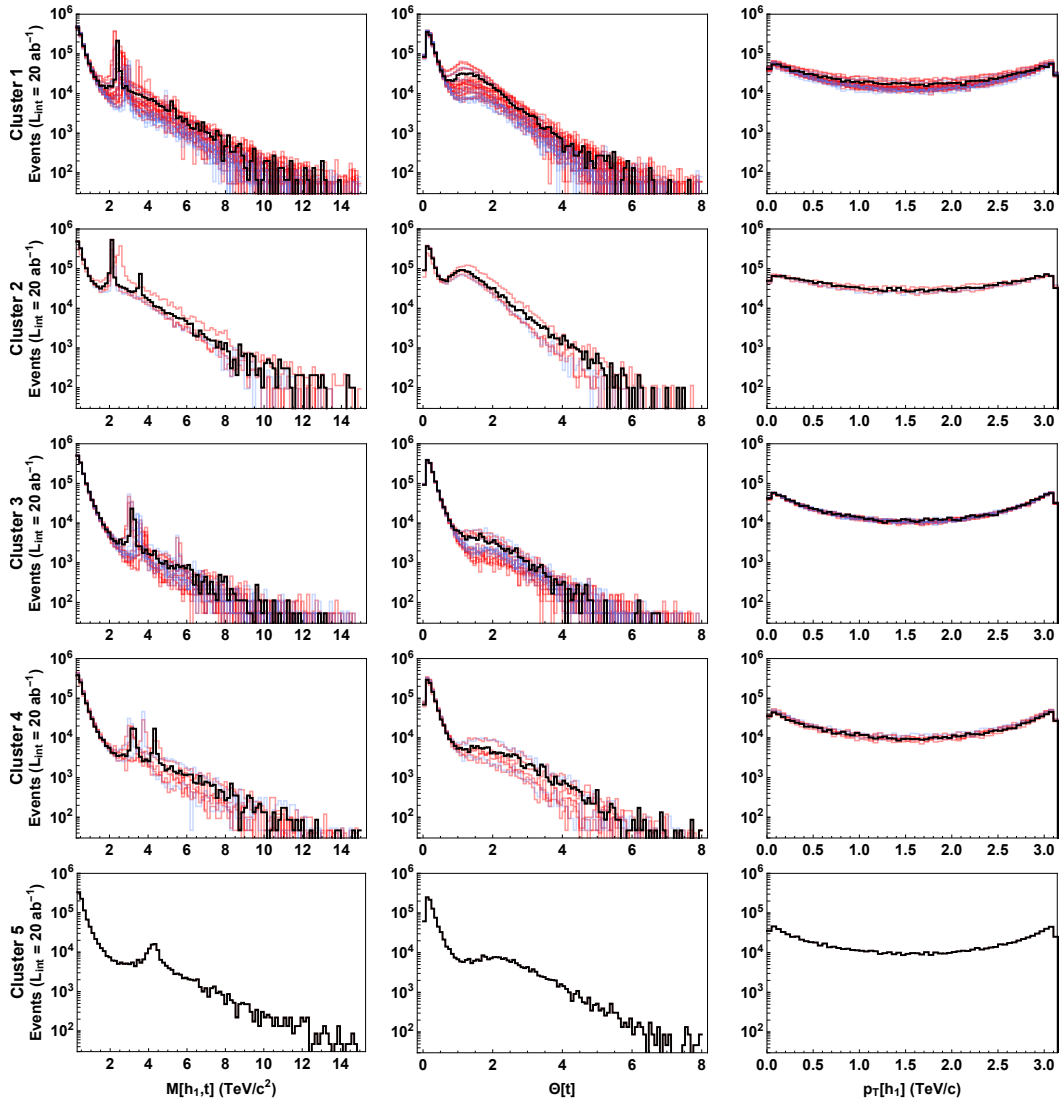

Figure D.3: Distributions at $\sqrt{s} = 100$ TeV for the invariant mass of the pair composed by top and most energetic Higgs h_1 (first column), the top quark angle (second column) and the transverse momenta of h_1 (third column), organized in clusters by similarity (clusters 1 through 5). Red and blue curves indicate respectively points in Regions I and II of the HS-MCHM$_5$. The benchmark point for each cluster is shown in black, with clusters 1 to 5 containing respectively points E_1 to E_5 in Table 5.1.

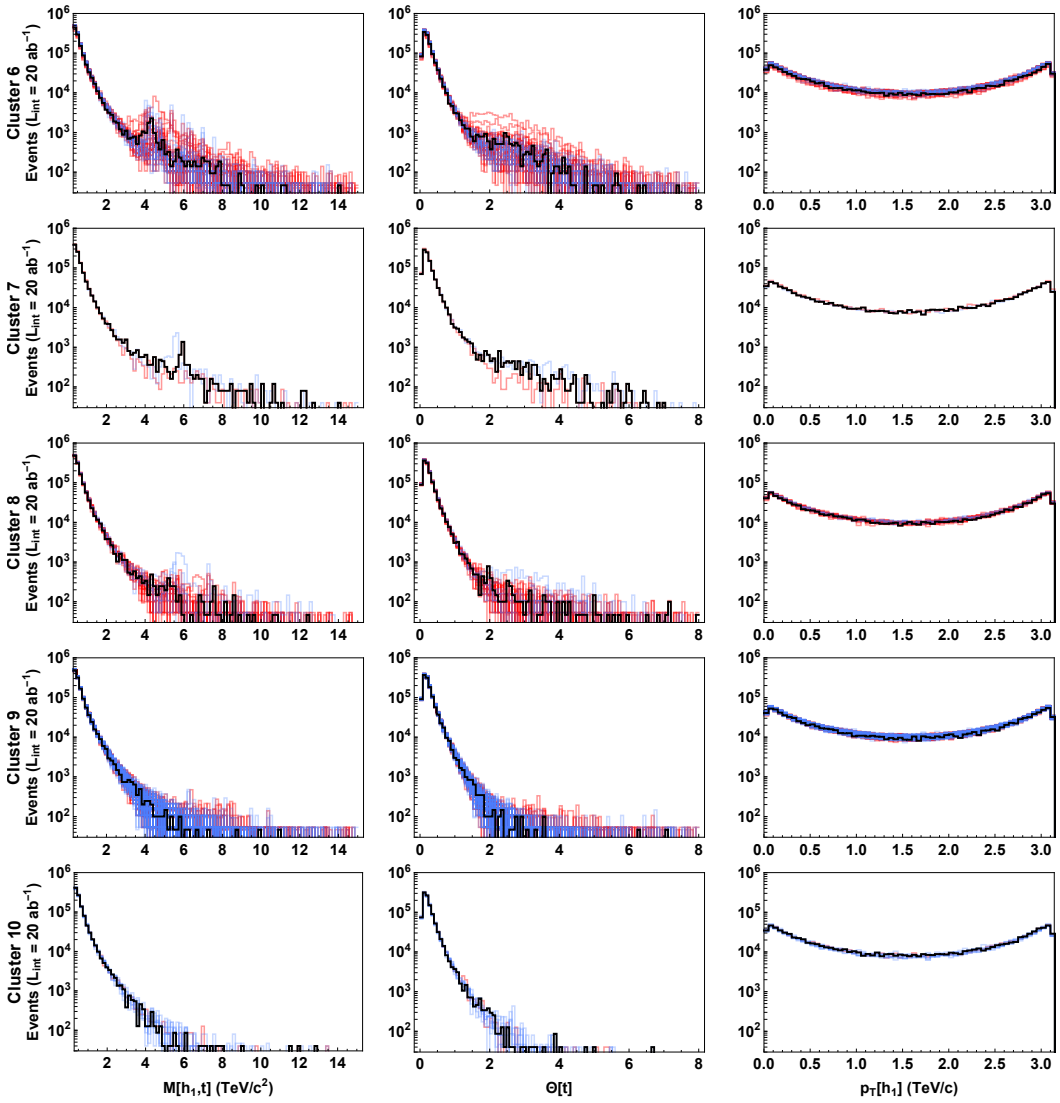

Figure D.4: Distributions at $\sqrt{s} = 100$ TeV for the invariant mass of the pair composed by top and most energetic Higgs h_1 (first column), the top quark angle (second column) and the transverse momenta of h_1 (third column), organized in clusters by similarity (clusters 6 through 10). Red and blue curves indicate respectively points in Regions I and II of the HS-MCHM$_5$. The benchmark point for each cluster is shown in black, with clusters 6 to 10 containing respectively points E_6 to E_{10} in Table 5.1.

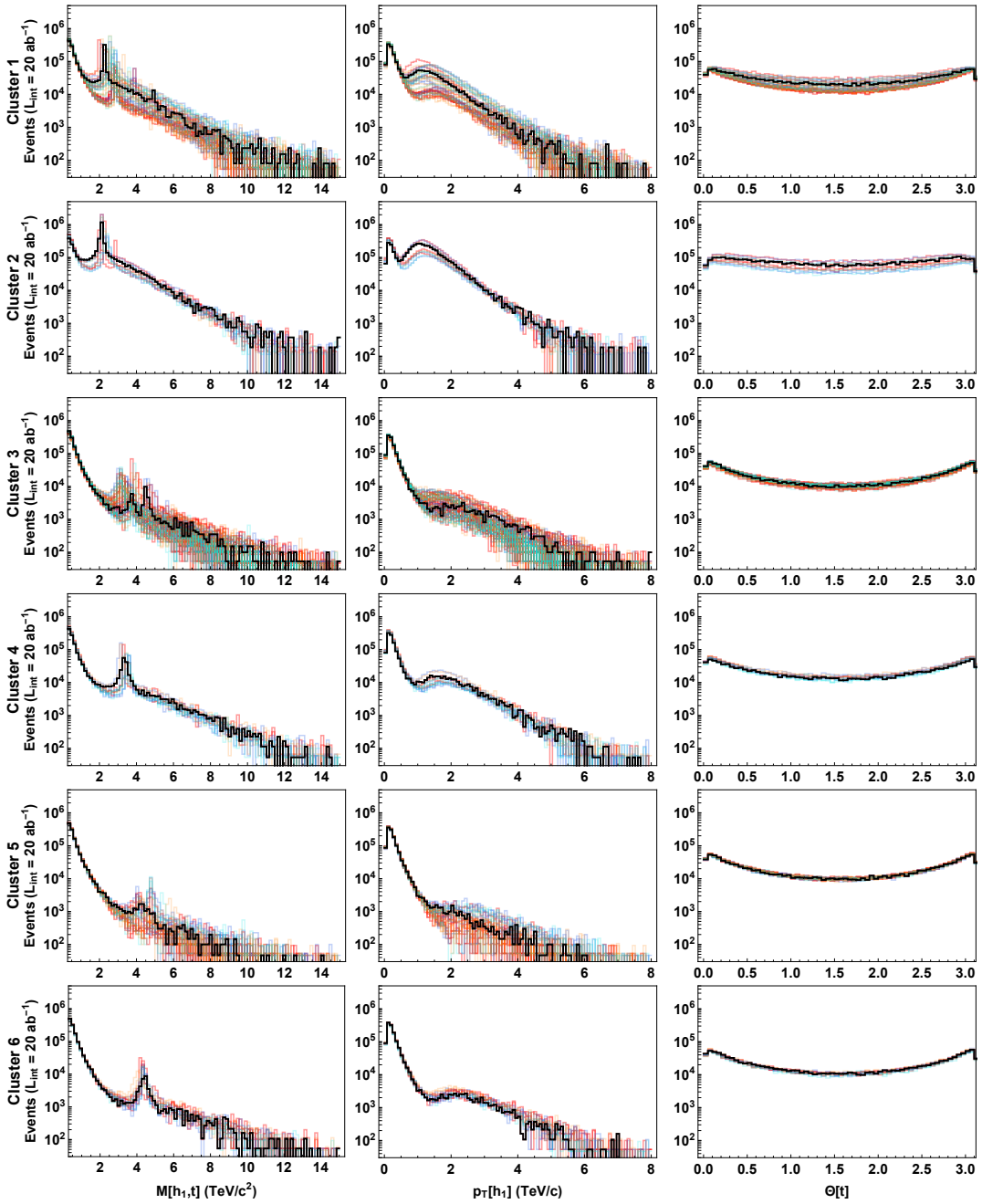

Figure D.5: Distributions at $\sqrt{s} = 100$ TeV for the invariant mass of the pair composed by top and most energetic Higgs h_1 (first column), transverse momenta of h_1 (second column) and the top angle (third column), organized in clusters by similarity (clusters 1 through 6). Red, blue, orange and cyan curves indicate respectively points in Regions I, II, III and IV of the HS-MCHM$_{14}$. The benchmark point for each cluster is shown in black, with clusters 1 to 6 containing respectively points F_1 to F_6 in Table 5.2.

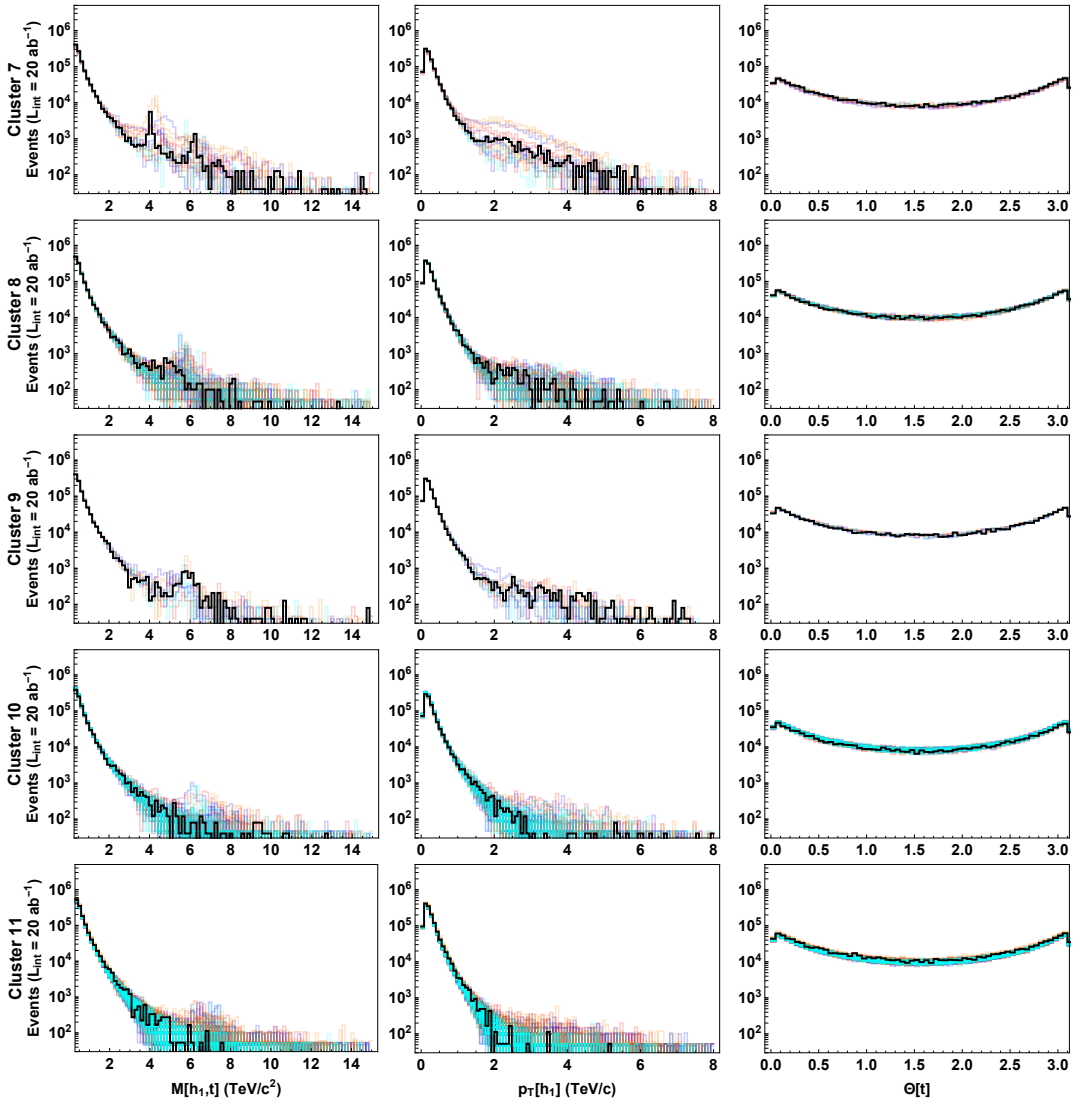

Figure D.6: Distributions at $\sqrt{s} = 100$ TeV for the invariant mass of the pair composed by top and most energetic Higgs h_1 (first column), transverse momenta of h_1 (second column) and the top angle (third column), organized in clusters by similarity (clusters 7 through 11). Red, blue, orange and cyan curves indicate respectively points in Regions I, II, III and IV of the HS-MCHM$_{14}$. The benchmark point for each cluster is shown in black, with clusters 1 to 6 containing respectively points F_7 to F_{11} in Table 5.2.

Bibliography

[1] G. Aad *et al.*, "Observation of a new particle in the search for the Standard Model Higgs boson with the ATLAS detector at the LHC," *Phys. Lett.*, vol. B716, pp. 1–29, 2012.

[2] S. Chatrchyan *et al.*, "Observation of a new boson at a mass of 125 GeV with the CMS experiment at the LHC," *Phys. Lett.*, vol. B716, pp. 30–61, 2012.

[3] Y. Gouttenoire, *Beyond the Standard Model Cocktail*. Springer Theses, Cham: Springer, 2022.

[4] Y. A. Gol'Fand and E. P. Likhtman, "Extension of the Algebra of Poincare Group Generators and Violation of P invariance," *Soviet Journal of Experimental and Theoretical Physics Letters*, vol. 13, p. 323, Apr. 1971.

[5] J. Wess and B. Zumino, "Supergauge transformations in four dimensions," *Nucl. Phys. B*, vol. 70, no. 1, pp. 39–50, 1974.

[6] J. Wess and B. Zumino, "A lagrangian model invariant under supergauge transformations," *Physics Letters B*, vol. 49, no. 1, pp. 52–54, 1974.

[7] J. Wess and B. Zumino, "Supergauge invariant extension of quantum electrodynamics," *Nuclear Physics B*, vol. 78, no. 1, pp. 1–13, 1974.

[8] L. Randall and R. Sundrum, "Large mass hierarchy from a small extra dimension," *Physical Review Letters*, vol. 83, pp. 3370–3373, oct 1999.

[9] L. Randall and R. Sundrum, "An alternative to compactification," *Physical Review Letters*, vol. 83, pp. 4690–4693, dec 1999.

[10] H. Georgi and D. B. Kaplan, "Composite higgs and custodial su(2)," *Physics Letters B*, vol. 145, no. 3, pp. 216–220, 1984.

[11] D. B. Kaplan and H. Georgi, "SU(2) x U(1) Breaking by Vacuum Misalignment," *Phys. Lett. B*, vol. 136, pp. 183–186, 1984.

[12] D. B. Kaplan, H. Georgi, and S. Dimopoulos, "Composite higgs scalars," *Physics Letters B*, vol. 136, no. 3, pp. 187–190, 1984.

[13] M. J. Dugan, H. Georgi, and D. B. Kaplan, "Anatomy of a Composite Higgs Model," *Nucl. Phys. B*, vol. 254, pp. 299–326, 1985.

[14] I. Zurbano Fernandez *et al.*, "High-Luminosity Large Hadron Collider (HL-LHC): Technical design report," vol. 10/2020, 12 2020.

[15] A. Abada, M. Abbrescia, S. AbdusSalam, *et al.*, "FCC-hh: The Hadron Collider," *Eur. Phys. J. Spec. Top. 228*, no. 228, p. 755–1107, 2019.

[16] M. Benedikt and F. Zimmermann, "Future circular collider: Integrated programme and feasibility study," *Frontiers in Physics*, vol. 10, 2022.

[17] M. Ahmad *et al.*, "CEPC-SPPC Preliminary Conceptual Design Report. 1. Physics and Detector," 3 2015.

[18] "CEPC-SPPC Preliminary Conceptual Design Report. 2. Accelerator," 1 2015.

[19] "CEPC Conceptual Design Report: Volume 1 - Accelerator," 9 2018.

[20] J. Tang, Y. Zhang, Q. Xu, J. Gao, X. Lou, and Y. Wang, "Snowmass 2021 White Paper AF4 - SPPC," in *2022 Snowmass Summer Study*, 3 2022.

[21] J. Tang, "Design concept for a future super proton-proton collider," *Frontiers in Physics*, vol. 10, 2022.

[22] R. Contino *et al.*, "Physics at a 100 TeV pp collider: Higgs and EW symmetry breaking studies," *CERN Yellow Rep.*, no. 3, pp. 255–440, 2017.

[23] N. Arkani-Hamed, T. Han, M. Mangano, and L.-T. Wang, "Physics opportunities of a 100 TeV proton–proton collider," *Phys. Rept.*, vol. 652, pp. 1–49, 2016.

[24] T. Golling *et al.*, "Physics at a 100 TeV pp collider: beyond the Standard Model phenomena," *CERN Yellow Rep.*, no. 3, pp. 441–634, 2017.

[25] K. Agashe, R. Contino, and A. Pomarol, "The Minimal composite Higgs model," *Nucl. Phys.*, vol. B719, pp. 165–187, 2005.

[26] M. Aaboud *et al.*, "Observation of Higgs boson production in association with a top quark pair at the LHC with the ATLAS detector," *Phys. Lett.*, vol. B784, pp. 173–191, 2018.

[27] A. M. Sirunyan *et al.*, "Observation of $t\bar{t}H$ production," *Phys. Rev. Lett.*, vol. 120, no. 23, p. 231801, 2018.

[28] L. A. F. do Prado, "Exploring the Higgs sector Beyond the Standard Model with the Top Yukawa coupling: a phenomenological and experimental search." PhD thesis defended in July, 2020, available at https://repositorio.unesp.br/handle/11449/193301?locale-attribute=en.

[29] "Search for the nonresonant $t\bar{t}HH$ production in the semileptonic decay of the top pair and the Higgs pair decay into b quarks at the HL-LHC," tech. rep., CERN, Geneva, 2022.

[30] G. Li, L.-X. Xu, B. Yan, and C.-P. Yuan, "Resolving the degeneracy in top quark Yukawa coupling with Higgs pair production," *Phys. Lett. B*, vol. 800, p. 135070, 2020.

[31] B. Gripaios, T. Müller, M. A. Parker, and D. Sutherland, "Search strategies for top partners in composite higgs models," *Journal of High Energy Physics*, vol. 2014, Aug 2014.

[32] M. Backović, T. Flacke, J. H. Kim, and S. J. Lee, "Search strategies for TeV scale fermionic top partners with charge 2/3," *Journal of High Energy Physics*, vol. 2016, pp. 1–51, apr 2016.

[33] A. M. Sirunyan *et al.*, "Search for pair production of vectorlike quarks in the fully hadronic final state," *Phys. Rev. D*, vol. 100, p. 072001, Oct 2019.

[34] A. M. Sirunyan *et al.*, "Search for vector-like T and B quark pairs in final states with leptons at $\sqrt{s} = 13$ TeV," *JHEP*, vol. 08, p. 177, 2018.

[35] M. Aaboud *et al.*, "Combination of the searches for pair-produced vector-like partners of the third-generation quarks at $\sqrt{s} = 13$ TeV with the ATLAS detector," *Phys. Rev. Lett.*, vol. 121, no. 21, p. 211801, 2018.

[36] M. Aaboud *et al.*, "Search for pair and single production of vectorlike quarks in final states with at least one z boson decaying into a pair of electrons or muons in pp collision data collected with the atlas detector at $\sqrt{s} = 13$ TeV," *Phys. Rev. D*, vol. 98, p. 112010, Dec 2018.

[37] CMS Collaboration, "Search for top-quark partners with charge 5/3 in the same-sign dilepton final state," *Physical Review Letters*, vol. 112, Apr 2014.

[38] CMS Collaboration, "Search for top quark partners with charge 5/3 in proton-proton collisions at $\sqrt{s} = 13$ TeV," *Journal of High Energy Physics*, vol. 2017, Aug 2017.

[39] A. M. Sirunyan *et al.*, "Search for top quark partners with charge 5/3 in the same-sign dilepton and single-lepton final states in proton-proton collisions at $\sqrt{s} = 13$ TeV," *JHEP*, vol. 03, p. 082, 2019.

[40] CMS Collaboration, "Search for pair production of vector-like quarks in leptonic final states in proton-proton collisions at $\sqrt{s} = 13$ TeV," tech. rep., CERN, Geneva, 2022. Submitted to the Journal of High Energy Physics. All figures and tables can be found at http://cms-results.web.cern.ch/cms-results/public-results/publications/B2G-20-011 (CMS Public Pages).

[41] M. Cepeda *et al.*, *Report from Working Group 2: Higgs Physics at the HL-LHC and HE-LHC*, vol. 7, pp. 221–584. 12 2019.

[42] C. Bautista, L. de Lima, R. D. Matheus, E. Pontón, L. A. Fernandes do Prado, and A. Savoy-Navarro, "Probing the top-Higgs sector with composite Higgs models at present and future hadron colliders," *JHEP*, vol. 03, p. 049, 2021.

[43] C. Bautista, L. de Lima, R. D. Matheus, and A. Savoy-Navarro, "On the Importance of Three-Body Decays of Vector-Like Quarks," 3 2023.

[44] G. Panico and A. Wulzer, "The Composite Nambu-Goldstone Higgs," *Lect. Notes Phys.*, vol. 913, pp. pp.1–316, 2016.

[45] A. Falkowski, F. Riva, and A. Urbano, "Higgs at last," *JHEP*, vol. 11, p. 111, 2013.

[46] M. Carena, L. Da Rold, and E. Pontón, "Minimal Composite Higgs Models at the LHC," *JHEP*, vol. 06, p. 159, 2014.

[47] G. Buchalla, O. Cata, and C. Krause, "A Systematic Approach to the SILH Lagrangian," *Nucl. Phys.*, vol. B894, pp. 602–620, 2015.

[48] V. Sanz and J. Setford, "Composite Higgs Models after Run 2," *Adv. High Energy Phys.*, vol. 2018, p. 7168480, 2018.

[49] D. Liu, I. Low, and C. E. M. Wagner, "Modification of Higgs Couplings in Minimal Composite Models," *Phys. Rev.*, vol. D96, p. 035013, 2017.

[50] A. Banerjee, G. Bhattacharyya, N. Kumar, and T. S. Ray, "Constraining Composite Higgs Models using LHC data," *JHEP*, vol. 03, p. 062, 2018.

[51] J. de Blas, O. Eberhardt, and C. Krause, "Current and Future Constraints on Higgs Couplings in the Nonlinear Effective Theory," *JHEP*, vol. 07, p. 048, 2018.

[52] K. Agashe, R. Contino, L. Da Rold, and A. Pomarol, "A Custodial symmetry for $Zb\bar{b}$," *Phys. Lett.*, vol. B641, pp. 62–66, 2006.

[53] M. Carena, E. Pontón, J. Santiago, and C. E. M. Wagner, "Light Kaluza Klein States in Randall-Sundrum Models with Custodial SU(2)," *Nucl. Phys.*, vol. B759, pp. 202–227, 2006.

[54] C. Anastasiou, E. Furlan, and J. Santiago, "Realistic Composite Higgs Models," *Phys. Rev.*, vol. D79, p. 075003, 2009.

[55] A. Orgogozo and S. Rychkov, "The S parameter for a Light Composite Higgs: a Dispersion Relation Approach," *JHEP*, vol. 06, p. 014, 2013.

[56] C. Grojean, O. Matsedonskyi, and G. Panico, "Light top partners and precision physics," *JHEP*, vol. 10, p. 160, 2013.

[57] A. Pich, I. Rosell, and J. J. Sanz-Cillero, "Oblique S and T Constraints on Electroweak Strongly-Coupled Models with a Light Higgs," *JHEP*, vol. 01, p. 157, 2014.

[58] C. Englert, A. Freitas, M. M. Muhlleitner, T. Plehn, M. Rauch, M. Spira, and K. Walz, "Precision Measurements of Higgs Couplings: Implications for New Physics Scales," *J. Phys.*, vol. G41, p. 113001, 2014.

[59] D. Croon, B. M. Dillon, S. J. Huber, and V. Sanz, "Exploring holographic Composite Higgs models," *JHEP*, vol. 07, p. 072, 2016.

[60] A. Pomarol and F. Riva, "The Composite Higgs and Light Resonance Connection," *JHEP*, vol. 08, p. 135, 2012.

[61] G. Panico, M. Redi, A. Tesi, and A. Wulzer, "On the Tuning and the Mass of the Composite Higgs," *JHEP*, vol. 03, p. 051, 2013.

[62] M. Montull, F. Riva, E. Salvioni, and R. Torre, "Higgs Couplings in Composite Models," *Phys. Rev.*, vol. D88, p. 095006, 2013.

[63] A. Carmona and F. Goertz, "A naturally light Higgs without light Top Partners," *JHEP*, vol. 05, p. 002, 2015.

[64] S. Kanemura, K. Kaneta, N. Machida, S. Odori, and T. Shindou, "Single and double production of the higgs boson at hadron and lepton colliders in minimal composite higgs models," *Phys. Rev.*, vol. D94, no. 1, p. 015028, 2016.

[65] M. B. Gavela, K. Kanshin, P. A. N. Machado, and S. Saa, "The linear-non-linear frontier for the Goldstone Higgs," *Eur. Phys. J.*, vol. C76, no. 12, p. 690, 2016.

[66] H.-L. Li, L.-X. Xu, J.-H. Yu, and S.-H. Zhu, "EFTs meet Higgs Nonlinearity, Compositeness and (Neutral) Naturalness," *JHEP*, vol. 09, p. 010, 2019.

[67] D. B. Kaplan, "Flavor at SSC energies: A new mechanism for dynamically generated fermion masses," *Nuclear Physics B*, vol. 365, no. 2, pp. 259 – 278, 1991.

[68] G. Aad, B. Abbott, D. Abbott, O. Abdinov, A. Abed Abud, K. Abeling, D. Abhayasinghe, S. Abidi, O. AbouZeid, N. Abraham, and et al., "Combined measurements of Higgs boson production and decay using up to 80 fb^{-1} of proton-proton collision data at $\sqrt{s} = 13$ TeV collected with the ATLAS experiment," *Physical Review D*, vol. 101, Jan 2020.

[69] M. Redi and A. Weiler, "Flavor and CP invariant composite Higgs models," *Journal of High Energy Physics*, vol. 2011, Nov 2011.

[70] Wolfram Research, "Mathematica 8.0," 2010.

[71] J. Gao, "CEPC and SPPC Status from the completion of the CDR towards TDR," *Journal of Modern Physics A*, p. to be published, 2020.

[72] D. Liu, L. T. Wang, and K. P. Xie, "Prospects of searching for composite resonances at the LHC and beyond," *JHEP*, vol. 01, p. 157, 01 2019.

[73] A. Alloul, N. D. Christensen, C. Degrande, C. Duhr, and B. Fuks, "FeynRules 2.0 - A complete toolbox for tree-level phenomenology," *Comput. Phys. Commun.*, vol. 185, pp. 2250–2300, 2014.

[74] J. Alwall, R. Frederix, S. Frixione, V. Hirschi, F. Maltoni, O. Mattelaer, H. S. Shao, T. Stelzer, P. Torrielli, and M. Zaro, "The automated computation of tree-level and next-to-leading order differential cross sections, and their matching to parton shower simulations," *JHEP*, vol. 07, p. 079, 2014.

[75] E. Conte, B. Fuks, and G. Serret, "MadAnalysis 5, A User-Friendly Framework for Collider Phenomenology," *Comput. Phys. Commun.*, vol. 184, pp. 222–256, 2013.

[76] R. Contino, M. Ghezzi, M. Moretti, G. Panico, F. Piccinini, and A. Wulzer, "Anomalous Couplings in Double Higgs Production," *JHEP*, vol. 08, p. 154, 2012.

[77] A. Carvalho, M. Dall'Osso, T. Dorigo, F. Goertz, C. A. Gottardo, and M. Tosi, "Higgs Pair Production: Choosing Benchmarks With Cluster Analysis," *JHEP*, vol. 04, p. 126, 2016.

[78] M. Aaboud *et al.*, "Search for pair production of up-type vector-like quarks and for four-top-quark events in final states with multiple b-jets with the atlas detector," *JHEP*, vol. 07, p. 089, 2018.

[79] CMS Collaboration, "Sensitivity projections for Higgs boson properties measurements at the HL-LHC," *CMS-PAS-FTR-18-011*, 11 2018.

[80] ATLAS Collaboration, "Projections for measurements of Higgs boson cross sections, branching ratios, coupling parameters and mass with the ATLAS detector at the HL-LHC," *ATL-PHYS-PUB-2018-054*, 2018.

[81] M. Aaboud *et al.*, "Search for pair production of Higgs bosons in the $b\bar{b}b\bar{b}$ final state using proton-proton collisions at $\sqrt{s} = 13$ TeV with the ATLAS detector," *JHEP*, vol. 01, p. 030, 2019.

[82] A. M. Sirunyan *et al.*, "Search for nonresonant Higgs boson pair production in the $\mathrm{b\bar{b}b\bar{b}}$ final state at $\sqrt{s} = 13$ TeV," *JHEP*, vol. 04, p. 112, 2019.

[83] A. Arganda, C. Garcia-Garcia, and M. Herrero, "Probing the Higgs self-coupling through double Higgs production in Vector Boson scattering at the LHC," *Nucl. Phys.*, vol. B945, p. 114687, 2019.

[84] G. Aad *et al.*, "Search for the $HH \to b\bar{b}b\bar{b}$ process via vector-boson fusion production using proton-proton collisions at $\sqrt{s} = 13$ TeV with the ATLAS detector," *JHEP*, vol. 07, p. 108, 2020.

[85] C. Englert, F. Krauss, M. Spannowsky, and J. M. Thompson, "Di-Higgs Phenomenolgy in tthh channel: the forgotten channel," *Phys. Let.*, vol. B743, pp. 93–97, 2015.

[86] S. Banerjee, F. Krauss, and M. Spannowsky, "Revisiting the tthh channel at the FCC-hh," *Phys. Rev.*, vol. D100, p. 073012, 2019.

[87] M. Gillioz, R. Gröber, C. Grojean, M. Mühlleitner, and E. Salvioni, "Higgs low-energy theorem (and its corrections) in composite models," *Journal of High Energy Physics*, vol. 2012, Oct 2012.

[88] A. M. Sirunyan, A. Tumasyan, W. Adam, F. Ambrogi, T. Bergauer, J. Brandstetter, M. Dragicevic, J. Erö, A. Escalante Del Valle, and et al., "Measurement of top quark pair production in association with a Z boson in proton-proton collisions at $\sqrt{s} = 13$ TeV," *Journal of High Energy Physics*, vol. 2020, Mar 2020.

[89] M. Aaboud *et al.*, "Measurement of the $t\bar{t}Z$ and $t\bar{t}W$ cross sections in proton-proton collisions at $\sqrt{s} = 13$ TeV with the ATLAS detector," *Phys. Rev. D*, vol. 99, no. 7, p. 072009, 2019.

[90] A. De Simone, O. Matsedonskyi, R. Rattazzi, and A. Wulzer, "A first top partner hunter's guide," *Journal of High Energy Physics*, vol. 2013, Apr 2013.

[91] T. Sjöstrand, S. Ask, J. R. Christiansen, R. Corke, N. Desai, P. Ilten, S. Mrenna, S. Prestel, C. O. Rasmussen, and P. Z. Skands, "An introduction to pythia 8.2," *Computer Physics Communications*, vol. 191, pp. 159–177, 2015.

[92] J. de Favereau, , C. Delaere, P. Demin, A. Giammanco, V. Lemaître, A. Mertens, and M. Selvaggi, "DELPHES 3: a modular framework for fast simulation of a generic collider experiment," *Journal of High Energy Physics*, vol. 2014, feb 2014.

[93] R. Brun and F. Rademakers, "ROOT: An object oriented data analysis framework," *Nucl. Instrum. Meth. A*, vol. 389, pp. 81–86, 1997. See also: zenodo.org/record/3895860 (ROOT v6.18/02).

[94] M. Cacciari and G. P. Salam, "Dispelling the N^3 myth for the k_t jet-finder," *Physics Letters B*, vol. 641, no. 1, pp. 57–61, 2006.

[95] M. Cacciari, G. P. Salam, and G. Soyez, "FastJet user manual," *The European Physical Journal C*, vol. 72, mar 2012.

[96] A. M. Sirunyan *et al.*, "Search for vector-like T and B quark pairs in final states with leptons at $\sqrt{s} = 13$ TeV," *Journal of High Energy Physics*, vol. 2018, aug 2018.

[97] E. Alvarez, D. A. Faroughy, J. F. Kamenik, R. Morales, and A. Szynkman, "Four Tops for LHC," *Nucl. Phys. B*, vol. 915, pp. 19–43, 2017.

[98] A. M. Sirunyan *et al.*, "Search for production of four top quarks in final states with same-sign or multiple leptons in proton-proton collisions at $\sqrt{s} = 13$ TeV," *Eur. Phys. J. C*, vol. 80, no. 2, p. 75, 2020.

[99] G. Aad *et al.*, "Evidence for $t\bar{t}t\bar{t}$ production in the multilepton final state in proton–proton collisions at $\sqrt{s} = 13$ TeV with the ATLAS detector," *Eur. Phys. J. C*, vol. 80, no. 11, p. 1085, 2020.